NUMERICAL INVESTIGATION OF INTERACTION BETWEEN HYDRAULIC FRACTURES AND NATURAL FRACTURES

A Thesis

by

WENXU XUE

Submitted to the Office of Graduate Studies of
Texas A&M University
in partial fulfillment of the requirements for the degree of

MASTER OF SCIENCE

December 2010

Major Subject: Petroleum Engineering

Numerical Investigation of Interaction Between Hydraulic Fractures and Natural Fractures

NUMERICAL INVESTIGATION OF INTERACTION BETWEEN HYDRAULIC FRACTURES AND NATURAL FRACTURES

A Thesis

by

WENXU XUE

Submitted to the Office of Graduate Studies of
Texas A&M University
in partial fulfillment of the requirements for the degree of

MASTER OF SCIENCE

Approved by:

Chair of Committee,	Ahmad Ghassemi
Committee Members,	Stephen A. Holditch
	Yuefeng Sun
Head of Department,	Stephen A. Holditch

December 2010

Major Subject: Petroleum Engineering

ABSTRACT

Numerical Investigation of Interaction Between Hydraulic Fractures and Natural Fractures. (December 2010)

Wenxu Xue, B.S., Tsinghua University

Chair of Advisory Committee: Dr. Ahmad Ghassemi

Hydraulic fracturing of a naturally-fractured reservoir is a challenge for industry, as fractures can have complex growth patterns when propagating in systems of natural fractures in the reservoir. Fracture propagation near a natural fracture (NF) considering interaction between a hydraulic fracture (HF) and a pre-existing NF, has been investigated comprehensively using a two dimensional Displacement Discontinuity Method (DDM) Model in this thesis.

The rock is first considered as an elastic impermeable medium (with no leakoff), and then the effects of pore pressure change as a result of leakoff of fracturing fluid are considered. A uniform pressure fluid model and a Newtonian fluid flow model are used to calculate the fluid flow, fluid pressure and width distribution along the fracture. Joint elements are implemented to describe different NF contact modes (stick, slip, and open mode). The structural criterion is used for predicting the direction and mode of fracture propagation.

The numerical model was used to first examine the mechanical response of the NF to predict potential reactivation of the NF and the resultant probable location for fracture re-initiation. Results demonstrate that: 1) Before the HF reaches a NF, the possibility of fracture re-initiation across the NF and with an offset is enhanced when the NF has weaker interfaces; 2) During the stage of fluid infiltration along the NF, a maximum tensile stress peak can be generated at the end of the opening zone along the NF ahead of the fluid front; 3) Poroelastic effects, arising from fluid diffusion into the rock deformation can induce closure and compressive stress at the center of the NF ahead of the HF tip before HF arrival. Upon coalescence when fluid flows along the NF, the poroelastic effects tend to reduce the value of the HF aperture and this decreases the tension peak and the possibility of fracture re-initiation with time.

Next, HF trajectories near a NF were examined prior to coalesce with the NF using different joint, rock and fluid properties. Our analysis shows that: 1) Hydraulic fracture trajectories near a NF may bend and deviate from the direction of the maximum horizontal stress when using a joint model that includes initial joint deformation; 2) Hydraulic fractures propagating with higher injection rate or fracturing fluid of higher viscosity propagate longer distance when turning to the direction of maximum horizontal stress; 3) Fracture trajectories are less dependent on injection rate or fluid viscosity when using a joint model that includes initial joint deformation; whereas, they are more dominated by injection rate and fluid viscosity when using a joint model that excludes initial joint deformation.

DEDICATION

To My Family

ACKNOWLEDGEMENTS

I would like to express my sincere gratitude to my advisor, Dr. Ahmad Ghassemi. He has been very patient and has encouraged me throughout my graduate study. His guidance and help enabled me to complete the research project. I would also like to thank Dr. Stephen A. Holditch and Dr. Yuefeng Sun for their kindly serving as committee members and reviewing the thesis.

I feel grateful to all my family members for their love and support. I thank my grandparents and parents for bringing me up and encouraging me to pursue graduate study. I thank my husband for his constant understanding and support.

Appreciation also goes to my friends and colleagues for their help in finishing my thesis and to the department faculty and staff for making my time at Texas A&M University a great experience. I would especially like to thank Jun Ge, Chakra Rawal, Jian Huang and Qingfeng Tao for their help on my study.

Finally, great appreciation goes to the RPSEA (through GTI) for providing the financial support for this research; matching support from Crisman Institute of Texas A&M University is also appreciated.

TABLE OF CONTENTS

Page

LIST OF FIGURES

Page

LIST OF TABLES

1 INTRODUCTION

1.1 Hydraulic Fracturing

Hydraulic fracturing is a process in which viscous hydraulic fluids and sorted proppant are mixed together and pumped into the wellbore to initiate and extend fractures in the rock formation. Hydraulic fracturing is a technique widely used in the petroleum industry to enhance the recovery of oil and gas from underground hydrocarbon reservoirs. It is also applied in the areas such as heat extraction from geothermal reservoirs, fault reactivation in mining and the measurement of in situ stress.

1.2 Hydraulic Fracture Modeling

Numerous analytical and numerical models have been developed to simulate hydraulic fracturing. The early efforts focused on analytical solutions for fractures of simple geometry, such as a straight crack in plane strain condition or a `penny-shaped crack (Geertsma and de Klerk 1969; Khristianovic and Zheltov 1955; Nordgren 1972; Perkins and Kern 1961; Sneddon 1946). All these solutions are approximate, and they contain simplifications in relation to either the opening or the pressure field within the crack. In recent years, research efforts have been directed towards the development of numerical algorithms to model the propagation of hydraulic fractures in rocks characterized by different mechanical properties and/or in-situ stresses, and natural discontinuities.

This thesis follows the style of *SPE Journal.*

Hydraulic fracturing is a complicated and challenging process to model, as it involves the coupling of at least three components:

1) Mechanical deformation in rock induced by the fluid pressure on fracture surface
2) Fluid flow within the fracture
3) Fracture propagation in the rock formation.

In the following sections, the modeling consideration of these three components is discussed in detail.

1.2.1 Reservoir Rock

In most current models, the mechanical deformation in the rock mass due to the fluid pressure on the fracture surfaces is assumed to be linear elastic. However, many natural substances such as rocks and soils are porous and their matrix is permeated by a fluid such as liquid or gas. Usually both solid matrix and the pore network (pore space) are assumed to be continuous and form two interpenetrating continua. Porous media whose solid matrix/fluid system behaves linearly under applied loads is called poroelastic.

The theory of poroelasticity was introduced by Biot in 1941. Biot's equations of the linear theory of poroelasticity (see Appendix A) are derived from: Equations of linear elasticity for the solid matrix; Navier–Stokes equations for the viscous fluid; Darcy's law for the fluid flow through the porous matrix. The coupled poroelastic effects of the deformation of fluid-saturated porous media can be summarized as follows (Vandamme et al. 1989):

- Volumetric variations caused by changes in pore pressure: an increase of the pore pressure can induce a volumetric expansion of the porous rock;
- Pore pressure variations due to changes in mean stress: pore pressure is increased from the application of a confining pressure if the fluid is prevented from escaping (undrained condition);
- The sensitivity of the volumetric response of the rock to the rate of loading: the rock stiffness ranges from K_u (undrained bulk modulus) to K (drained bulk modulus), depending on the loading rate. In fast loading, the fluid has not enough time to dissipate so the rock is undrained and appears stiffer.

The poroelastic effects, which arise from coupling of the fluid flow and rock deformation, were mostly ignored in the fracture modeling. The inherent assumptions are that the time scale of the problem (diffusion) is such that poroelastic effects have not had time to develop and that the magnitude of the effect is small enough to be neglected (Boone et al. 1991). However, in many instances, such as injection into highly permeable sands or naturally fractured reservoirs, there is large leakoff into the formation during fracturing treatment so that poroelastic effects of significant magnitude can develop and need be considered. The poroelastic influences of a neighboring producing/inject well can create a heterogeneous stress field in the reservoir, and cause a hydraulic fracture to propagate deviating from its expected path of propagation (perpendicular to the minimum far-field compressive stress) (Berchenko and Detournay

1997). Also, pore pressure diffusion can decrease the effective stress in natural fractures promoting slip.

The influences of coupled poroelastic processes on fracture opening have also been addressed previously (Detournay and Cheng 1991; Ghassemi and Zhang 2006; Vandamme et al. 1989). It has been shown that poroelastic effects could cause the crack opening to decrease with time and that the opening and closure of the crack in response to poroelastic loads would have a corresponding influence on the stress intensity factor (SIF) at the crack tip. Therefore, it is of interest to simulate fracture propagation considering poroelastic effects of the host rock.

A few analytical procedures have been developed and used to solve the poroelastic effects on fracture propagation (Huang and Russell 1985; Ruina 1978). However, these analytical approaches are limited in solving many practical problems. Researchers have been continuing the efforts in developing various robust numerical methods such as the Boundary Element Method (BEM) (Crouch and Starfield 1983; Dong and de Pater 2001; Yan 2004) and the Finite Element Method (FEM) to solve crack problems. In terms of computational resources, BEM is more efficient than other methods, including FEM, for crack problems where surface/volume ratio is small, as in the BEM one only needs to construct a "mesh" over the modeled surface.

The displacement discontinuity (DD) method lends itself nicely to solving problems involving injection/production using hydraulically induced or natural fractures and provides for more flexibility. The square root crack tip element (Yan 2004) in the 2D real DD method greatly improves the accuracy of evaluation of stress/displacement and the SIF at the crack tip. In our present work, the 2D real DD BEM is used to model fracture deformation and propagation considering poroelastic effects of the rock.

1.2.2 Fluid Flow Within the Fracture

Although actual fluids used for hydraulic fracturing treatments have complicated rheologies, such as viscoelasticity, usually the fluid flow within the fracture is modeled using a simple model. Typical underlying assumptions include: the fracturing fluid has a uniform pressure distribution inside the fracture; the fracturing fluid is an incompressible Newtonian fluid such that the pressure gradient within the fracture is related to the flow rate and the fracture width governed by the Poiseuille's Law (Batchelor 1967); the fracturing fluid behavior can be approximated by a power-law model. In our current study, both assumptions of constant pressure distribution and Newtonian fluid are used as our focus is stimulation of unconventional gas reservoirs that are mostly treated with water.

1.2.3 Fracture Propagation

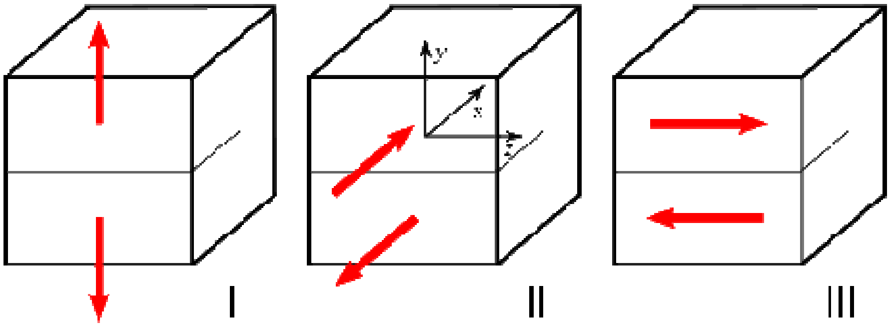

Fig. 1.1 Mode I, Mode II, and Mode III cracks (Wikipedia).

There are three different basic modes of fracture propagation as shown in **Fig. 1.1.** Mode I is opening or tensile mode, where the crack surfaces move apart in a direction perpendicular to the surfaces. Mode II is sliding or in-plane shear mode, where the crack surfaces slide over one another in a direction perpendicular to the leading edge of the crack. Mode III is tearing or antiplane shear mode, where the crack surfaces move relative to one another in a direction parallel to the leading edge of the crack.

The fracture propagation process is mostly modeled using linear elastic fracture mechanics (LEFM) theory, which assumes that the material is isotropic and linear elastic. Based on this assumption, the stress field near the crack tip is calculated using the theory of elasticity. LEFM is valid only when the zone of inelastic deformation at the crack tip is small compared to the size of the crack. The criterion of fracture propagation is mostly given by the maximum tangential tensile stress approach, conventional energy-release rate approach or stress intensity factor (SIF) approach.

The model we used here differs from those of previous studies in that it includes a more flexible crack initiation and propagation criterion - structural criterion (Dobroskok et al. 2005). This criterion is a unified criterion capable of predicting both Mode I (tensile, opening) and Mode II (sliding, shear) fracture propagation. Since Griffith's (1924) paper on fracture of brittle materials, immense literature has appeared on this subject. Most of these works have focused on Mode I propagation. And most previous hydraulic fracture propagation model were based on Mode I or mixed-mode propagation, without considering the possibility of Mode II propagation. However, in many cases in rock mechanics, Mode II propagation may prevail, or appear at some stage of crack growth. The importance of Mode II crack propagation in rock can be found in literature using both analytical (Bobet and Einstein 1998; Rao et al. 2003) and numerical (Bobet 2001; Tang et al. 2001) approaches.

1.3 Interaction of Hydraulic Fractures and Natural Fractures

The increased interest in exploration and production of low permeability reservoirs makes the design and evaluation of hydraulic fracturing treatments in these reservoirs a new challenge for industry. Many of the low permeability gas reservoirs, such as gas-bearing shales, and methane-bearing coals, are usually found crisscrossed by one more or sets of natural fractures where fracture can grow in a complicated manner.

Under these circumstances, it is often found that the fracturing fluid and proppant can reopen and flow through the pre-existing fractures, as well as create new fractures in the rock (Fisher et al. 2002). Also, shear stresses accumulated in the rock mass (due to the natural anisotropy of stresses and the presence of discontinuities such as natural fractures and faults) tend to be released during a treatment, triggering shear slippage along the discontinuities (Warpinski et al. 2004). In **Fig. 1.2,** microseismic fracture mapping reveals that complex network of fractures can be created in shale reservoir during fracture stimulation.

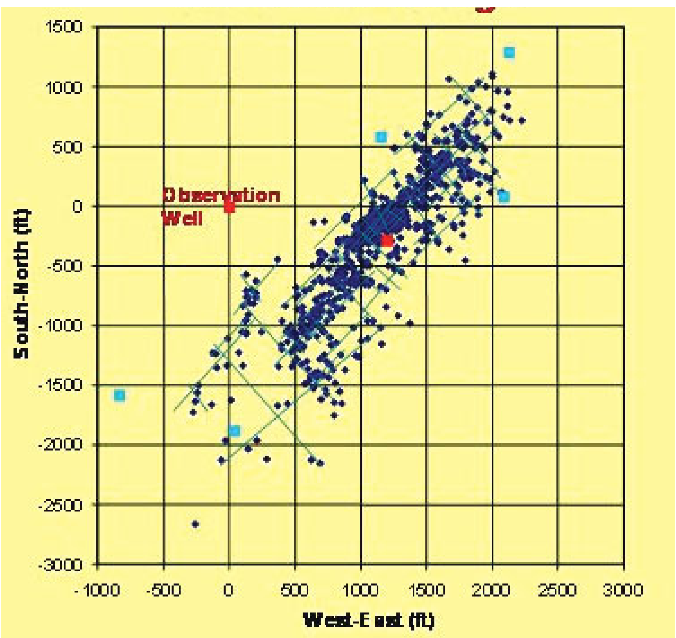

Fig. 1.2 Complex network of fractures created in shale reservoirs by fracture stimulation (images courtesy of Halliburton (Matt Blauch and Grieser)).

The problem of induced and natural fracture interaction has been the subject of many theoretical (Potluri et al. 2005), experimental/analytical (Blanton 1982; Warpinski and Teufel 1987), and numerical (Cooke and Underwood 2001; Koshelev and Ghassemi 2003; Thiercelin and Makkhyu 2007; Wu et al. 2004; Zhang and Jeffrey 2006) studies.

Blanton (1982) presented a simple analytical fracture interaction criterion relating differential stress and angle of interaction to extrapolate the lab results to field simulations. Warpinski and Teufel (1987) derived a fracture interaction criterion to predict whether the hydraulic fracture causes a shear slippage on the natural fracture plane causing arrest of the propagating fracture or dilates the natural fracture leading to excessive leakoff. Renshaw and Pollard (1995) provided a criterion for crack behavior that is near and orthogonal to un-bonded interfaces.

Potluri et al. (2005) reviewed various fracture interaction criteria and presented a systematic criteria for different types of fracture propagation modes near natural fractures, based on the conditions of differential stress, angle of intersection, and fracture toughness, and pressure drop within the natural fractures. However, for these analytical attempts, the in-situ stresses along the natural discontinuities were assumed not to have been affected by the hydraulic fracture, i.e., the mechanical interactions between the hydraulic fracture and the natural fracture were not considered.

Cooke and Underwood (2001) investigated the local sliding, de-bonding and the subsequent opening along bedding contacts using a Displacement Discontinuity (DD) method to study the probable fracture intersection modes with natural bedding contacts. The bedding contacts they considered were sliding-only interfaces, opening-only interfaces, and both sliding and opening interfaces. However the fracture considered in their study is far-field tension stress driven instead of fluid driven.

Koshelev and Ghassemi (2003) simulated the trajectory of a hydraulically driven crack near natural fractures, and interface between two inhomogeneous blocks using the complex variable hypersingular boundary element method (BEM). They demonstrated that natural fractures and other inhomogeneities can generate unstable fracture configurations under different initial crack inclination, loading, and geometry. But the pressure distribution along the hydraulic fracture was assumed to be constant and fluid flow remained to be solved in their simulated process.

Wu et al. (2004) studied fracture behavior crossing a bi-material interface. They used Griffith type global fracture criterion with anisotropic specific fracture energy, in addition to conventional mass and energy balances. The basic assumption in their study that fluid within the fracture follows a uniform pressure and that the interface is welded and no-slipping remained to be improved.

Zhang et al. (2006) considered fluid flow in the hydraulic fracture and obtained the resulting pressure distribution as it intersected the natural fracture and examined the conditions for further fracture propagation. The rock formation was modeled as an impermeable homogeneous elastic medium, and the fluid was modeled as an incompressible, Newtonian fluid injected at a constant rate. The frictional stress on the surfaces of pre-existing fractures was assumed to obey the Coulomb law. The DD method and the finite difference method were employed to deal with this coupling mechanism of rock fracture and fluid flow.

Thiercelin and Makkhyu (2007) presented a semi-analytical model based on the dislocation theory to predict the reactivation of a natural fault with an approaching hydraulic fracture. They assumed that re-initiation occurs prior to fracture touching the interface. They analyzed the maximum tensile stress on the opposite side of the natural fractures to determine the most probable location of fracture re-initiation. However, the influence of natural fracture reactivation on the change of in-situ stress and the resultant change of fracture response and interaction mode were not considered.

As a result of the complex nature of the problem, these investigations have been limited to the case of one HF approaching a single joint. The results have shown that the fracture patterns that can occur for hydraulically induced fractures propagating near natural fractures can be complex, and are determined by the state of stress in the neighborhood of the intersection and joint material properties. Generally, four types of interaction have been recognized using the 2D plain strain studies, as shown in **Fig. 1.3**; a hydraulic fracture can across the natural fracture without changing direction or it can be terminated by the natural fracture, it can propagate along the natural fracture, or reinitiate across the with an offset or jog (Zhang and Jeffrey 2006).

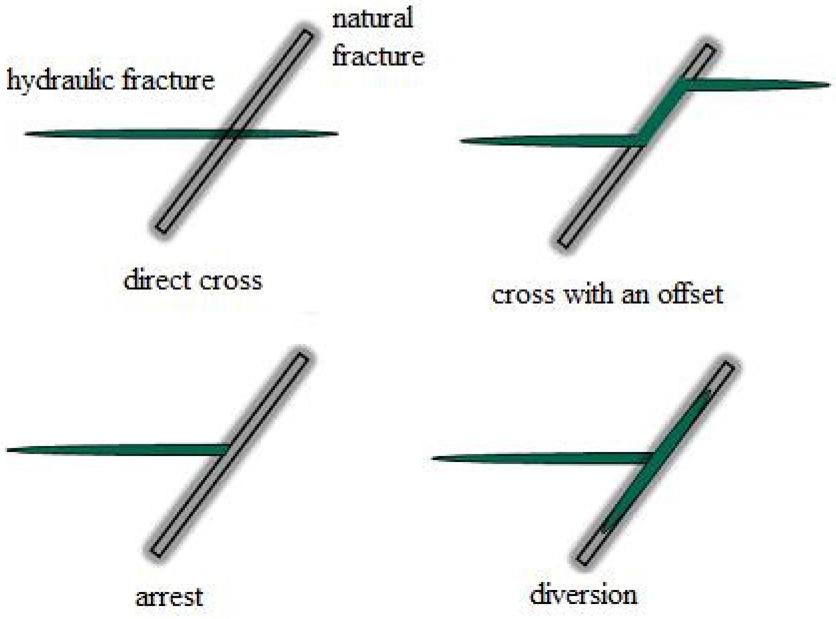

Fig. 1.3 Four types of interaction between hydraulic fracture and natural fracture (artwork from Zhang et al. (2006)).

Despite their limitations, numerical modeling has become an indispensable tool for researchers to obtain a more complete picture of the detailed process of fracture propagation near natural discontinuities.

Hydraulic fracture growth behavior in a naturally-fracture rock differs greatly from that of an intact rock. Models that can couple fluid flow, rock deformation, frictional and opening behavior of the natural interface and fracture propagation mechanics are needed to allow estimation of the stimulated volume when fracturing unconventional energy resources. Often, the model ought to consider poroelastic the effects of pore fluid diffusion on rock deformation to better understand the pressure history recorded during stimulation jobs.

1.4 Research Objectives

The main objectives of this study are:

- To study the interaction between a hydraulic fracture and a natural fracture.
- To study (via a parametric analysis) the effect of the model input parameters, such as rock, joint, and fluid properties, on the stresses/displacements distribution and the possible slipping/opening along the joint.
- To observe the general behavior of natural fractures and hydraulic fractures.
- To model the process of hydraulic fracture tip approaching pre-existing natural fractures.
- To quantify the orientation and extension of the stimulated fracture.

1.5 Sign Convention

In rock mechanics, compressive stresses are generally considered as positive for the convenience of engineering use. In this thesis, in order to be consistent with the rock mechanics literature, all equations are presented using the *compression positive convention*. This sign convention is adopted for the remainder of this thesis.

2 MODEL SETUP

2.1 Constant Displacement Discontinuity Method

Consider a line crack over a line segment $|x| \le a,\ y = 0$ in an infinite elastic material, as shown in **Fig. 2.1**. There is a constant displacement discontinuity when crossing over the crack, which can be defined as (Crouch and Starfield 1983):

$$\begin{aligned} D_x &= u_x(x,0_-) - u_x(x,0_+) \\ D_y &= u_y(x,0_-) - u_y(x,0_+) \end{aligned} \qquad \text{(2.1)}$$

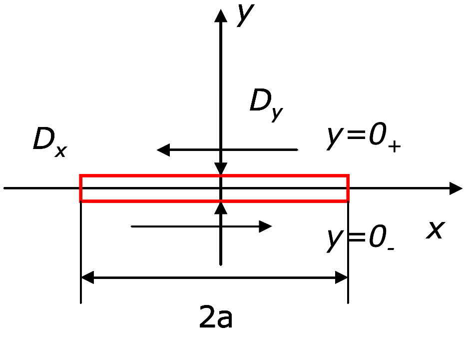

Fig. 2.1 Constant displacement discontinuity components over a line segment.

The displacements and stresses at a point (*x,y*) due to the constant displacement discontinuity D_x, D_y over the line segment are given by Crouch (1983):

$$\begin{aligned} u_x &= D_x\left[2(1-\nu)f_{,y} - yf_{,xx}\right] + D_y\left[-(1-2\nu)f_{,x} - yf_{,xy}\right] \\ u_y &= D_x\left[(1-2\nu)f_{,x} - yf_{,xy}\right] + D_y\left[2(1-\nu)f_{,y} - yf_{,yy}\right] \end{aligned} \qquad \text{(2.2)}$$

$$\begin{aligned}
\sigma_{xx} &= 2GD_x\left[2f_{,xy} + yf_{,xyy}\right] + 2GD_y\left[f_{,yy} + yf_{,yyy}\right]\\
\sigma_{yy} &= 2GD_x\left[-yf_{,xyy} + yf_{,xyy}\right] + 2GD_y\left[f_{,yy} - yf_{,yyy}\right]\\
\sigma_{xy} &= 2GD_x\left[f_{,yy} + yf_{,yyy}\right] + 2GD_y\left[-yf_{,xyy}\right]
\end{aligned} \tag{2.3}$$

where

$$\begin{aligned}
&f(x,y) = -\frac{1}{4\pi(1-\nu)}[y(\arctan\frac{y}{x-a} - \arctan\frac{y}{x+a}) -\\
&(x-a)In\sqrt{(x-a)^2+y^2} + (x+a)In\sqrt{(x+a)^2+y^2}\,]
\end{aligned} \tag{2.4}$$

Knowing the analytical solution for a single, constant elemental displacement discontinuity (DD), we can find the numerical solution to any problem by discretizing a curved crack with enough elements and by summing the effects of all N elements. The discretized form of displacement discontinuity equation can be formed as (Crouch and Starfield 1983):

$$\begin{aligned}
\overset{i}{\sigma}_s &= \sum_{j=1}^{N} \overset{ij}{A}_{ss}\,\overset{j}{D}_s + \sum_{j=1}^{N} \overset{ij}{A}_{sn}\,\overset{j}{D}_n\\
\overset{i}{\sigma}_n &= \sum_{j=1}^{N} \overset{ij}{A}_{ns}\,\overset{j}{D}_n + \sum_{j=1}^{N} \overset{ij}{A}_{nn}\,\overset{j}{D}_n
\end{aligned} \tag{2.5}$$

, and

$$\begin{aligned}
\overset{i}{u}_s &= \sum_{j=1}^{N} \overset{ij}{B}_{ss}\,\overset{j}{D}_s + \sum_{j=1}^{N} \overset{ij}{B}_{sn}\,\overset{j}{D}_n\\
\overset{i}{u}_n &= \sum_{j=1}^{N} \overset{ij}{B}_{ns}\,\overset{j}{D}_n + \sum_{j=1}^{N} \overset{ij}{B}_{nn}\,\overset{j}{D}_n
\end{aligned} \tag{2.6}$$

where $\overset{j}{D}_s$ and $\overset{j}{D}_n$ are the shear and normal components of discontinuity with respect to the local co-ordinates *s* and *n* at the *j*th element. $\overset{i}{\sigma}_s$ and $\overset{i}{\sigma}_n$ are the shear and normal stress at the midpoint of the i^{th} element. u_s^i and u_n^i are the shear and normal displacement at the midpoint of the i^{th} element. A and B are the influence coefficient matrix accounting for the different positions and orientations of each element.

Given the boundary conditions on each element, we can solve the system of algebraic equations of Eq. (2.5) and (2.6), and get the values of elemental DD that are necessary to produce the boundary condition, element by element along the crack. Once the displacement discontinuities D_s^j and D_n^j along the crack are found, the displacements and stresses at any point in the body can be determined by using Eq. (2.5) and (2.6) with the influence coefficients calculated for the point of interest.

2.2 Crack Tip Element

The theory of linear elastic fracture mechanics shows that the relative displacement between the crack surfaces in the small vicinity of the crack tip is proportional to $r^{1/2}$ (r is measured from the tip along the crack). Therefore, the constant DD method cannot produce accurate estimate of the stresses and displacements near the crack tip. To account for the $r^{1/2}$ variation, we used a special crack tip element at the crack tip. The schematic for a left crack tip is shown in **Fig. 2.2** and the DD for a left crack tip element can be written as (Yan 2004):

$$\begin{aligned} D_x &= H_s\left(\frac{a+\xi}{a}\right)^{0.5} \\ D_y &= H_n\left(\frac{a+\xi}{a}\right)^{0.5} \end{aligned} \quad \text{......} (2.7)$$

where H_s and H_n are the tangential and normal displacement discontinuity quantities at the center of the crack tip element.

Substitution of Eq. (2.7) into Eq. (2.2) and (2.3), the displacements and stresses at the crack tip then can be expressed in terms of H_s and H_n. The corresponding influence coefficient functions are given in **Appendix B** for completeness.

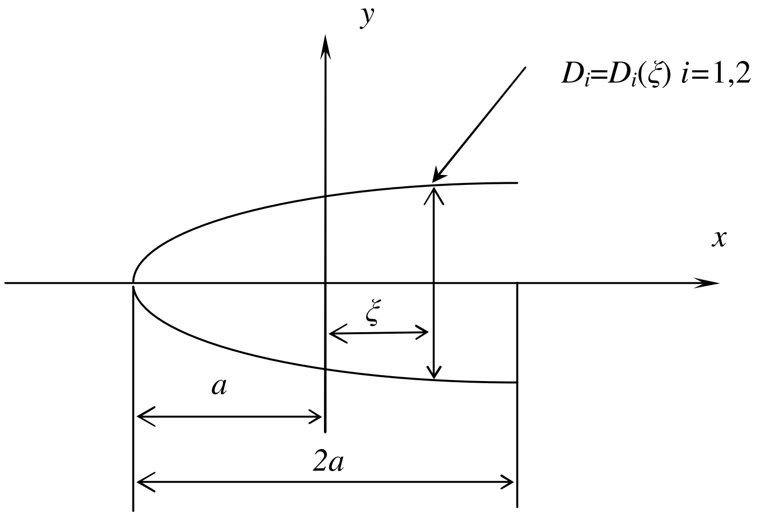

Fig. 2.2 Special crack tip displacement discontinuity at the left crack tip.

2.3 Fracture Propagation Scheme

We used the structural criterion (which has been described in detail in Dobroskok's (2005) paper) for modeling and automatic tracking of tensile and shear mode crack propagation.

The tensile driving force f_I is defined as averaged tangential stress ahead of the crack tip (Dobroskok et al. 2005):

$$f_I = \bar{\sigma}_{\theta\theta} = \frac{1}{d}\int_0^d \sigma_{\theta\theta}(r)dr\,,\ \bar{\sigma}_{\theta\theta} < 0 \quad \text{(2.8)}$$

where d is the characteristic size of the fracture process zone (FPZ) (see Section **3.1.2** for definition).

The shear driving force f_{II} is defined using Mohr-Coulomb criterion, relating to the averaged shear stress and tangential stress ahead of the crack tip (Dobroskok et al. 2005):

$$f_{II} = sign(\bar{\sigma}_{r\theta})\bar{\sigma}_{r\theta} - \tan\phi(-\bar{\sigma}_{\theta\theta}) = c\,,\ \bar{\sigma}_{\theta\theta} \geq 0 \quad \text{(2.9)}$$

where ϕ is rock friction angle, c is rock cohesion, and

$$\bar{\sigma}_{r\theta} = \frac{1}{d}\int_0^d \sigma_{r\theta}(r)dr \quad \text{(2.10)}$$

The normalized driving forces can be defined as (Dobroskok et al. 2005): Mode I (normalized tensile driving force, F_I):

$$F_I = \frac{f_I}{\sigma_t} = \frac{\bar{\sigma}_{\theta\theta}}{\sigma_t}, \bar{\sigma}_{\theta\theta} < 0 \quad \text{(2.11)}$$

where σ_t is rock tensile strength; Mode II (normalized shear driving force, F_{II}):

$$F_{II} = \frac{f_{II}}{c} = \frac{sign(\bar{\sigma}_{r\theta})\bar{\sigma}_{r\theta} - \tan\phi(-\bar{\sigma}_{\theta\theta})}{c}, \bar{\sigma}_{\theta\theta} \geq 0 \quad \text{(2.12)}$$

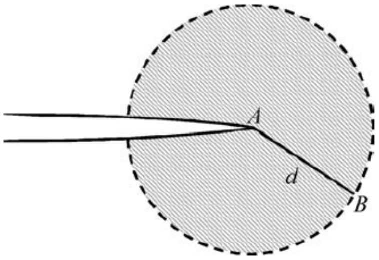

Fig. 2.3 Structural criterion: average stress over the segment *d* (length of FPZ) in the small vicinity of the crack tip (after Dobroskok et al. 2005).

To find the direction of crack propagation, normalized tensile and shear driving forces ahead of the crack tip are evaluated over a distance equal to the length of a FPZ, in directions comprising angles from $-\pi$ to $+\pi$ with the current tip element, as shown in **Fig. 2.3**. The directions and the values of the maximum normalized tensile or shear driving force are determined and a new element is added according to the criterion summarized in **Table 2.1**.

For Mode I (tensile mode) propagation, the propagation direction is the direction in which the normalized tensile driving force is maximum:

$$\theta_I = \left\{\theta : \max_{\theta} F_I(\theta)\right\} \qquad (2.13)$$

For Mode II (shear mode) propagation, the propagation direction is in the direction in which the normalized shear driving force is maximum:

$$\theta_{II} = \left\{\theta : \max_{\theta} F_{II}(\theta)\right\} \qquad (2.14)$$

The corresponding maximum normalized tensile and shear driving forces at θ_I and θ_{II} are denoted as $F_{IMAX} = F_I(\theta_I)$ and $F_{IIMAX} = F_{II}(\theta_{II})$, respectively.

Table 2.1 Different possibility, mode and direction of crack propagation (Dobroskok et al. 2005)

Maximum Normalized Driving Forces	Mode	Direction
$F_{\mathrm{IMAX}}<1$, $F_{\mathrm{IIMAX}}<1$	does not propagate	
$F_{\mathrm{IMAX}}>1$, $F_{\mathrm{IIMAX}}<1$	Mode I	$\theta_p = \theta_I$
$F_{\mathrm{IMAX}}<1$, $F_{\mathrm{IIMAX}}>1$	Mode II	$\theta_p = \theta_{II}$
$F_{\mathrm{IMAX}} > F_{\mathrm{IIMAX}} >1$	Mode I	$\theta_p = \theta_I$
$F_{\mathrm{IIMAX}} > F_{\mathrm{IMAX}} >1$	Mode II	$\theta_p = \theta_{II}$

In the case of a small FPZ ($d / \ell \leq 0.1$), the stresses at the crack tip (see **Fig. 2.4**) are calculated by the asymptotic analytical equation, which can be written as (Dobroskok et al. 2005):

$$\sigma_{\theta\theta}(r,\theta) = \frac{1}{\sqrt{2\pi r}} \cos^3 \frac{\theta}{2} (K_I - 3K_{II} a) \quad \text{.......} \quad (2.15)$$

$$\sigma_{r\theta}(r,\theta) = \frac{1}{\sqrt{2\pi r}} \cos^3 \frac{\theta}{2} [K_I a + K_{II}(1-2a^2)] \quad \text{.......} \quad (2.16)$$

where $a = \tan(\theta / 2)$.

As Eq. (2.15) and (2.16) are only valid at a small vicinity near the tip region, in the case of a large FPZ ($d / \ell > 0.15$ (ℓ: half length of the crack)), the stresses at the crack tip are calculated as stresses at field points based on Eq. (2.5).

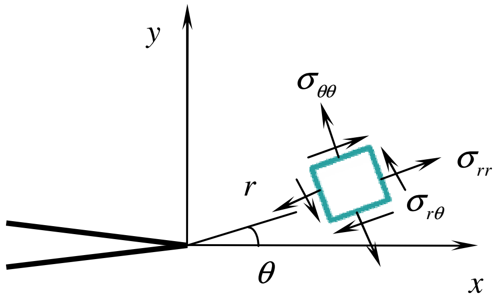

Fig. 2.4 Stress state in the vicinity of the crack tip.

While evaluating the driving forces, the induced stresses at a point in the current time step are calculated by summing the influence of the fictitious fluid sources over all elements in the system and over all preceding time steps. The boundary conditions on a newly added element are considered to be the same as those of the initial crack.

2.4 Newtonian Fluid Flow Within the Hydraulic Fracture

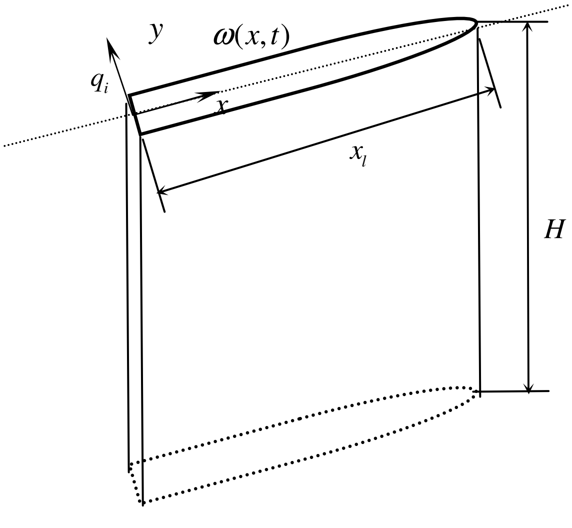

Fig. 2.5 Geometry for a plane strain fracture and the fluid flow within the fracture.

Apart from the assumption of constant fluid pressure distribution along the hydraulic fracture, we also model the fluid flow within the fracture as an incompressible Newtonian fluid in our study, as our focus is stimulation of unconventional gas reservoirs that are mostly treated with water.

The hydraulic fracture can be considered in a plane strain condition in the *xy* plane, when fracture height *H* >>fracture length *L*, as plotted in **Fig. 2.5**. Ignoring the fracture leakoff term, the continuity equation for flow of an incompressible fluid in the hydraulic fracture can be written as:

$$\frac{\partial \omega}{\partial t} = \frac{\partial q}{\partial x} \quad \text{..........} \quad (2.17)$$

where ω is the hydraulic fracture width, and q is the fluid flux through a cross-section of the fracture. Fluid flux can be expressed with respect to the fracture width and pressure gradient along the hydraulic fracture based on Poiseuille's law (Batchelor 1967):

$$q = \frac{\omega^3}{12\mu} \frac{\partial p_f}{\partial x} \quad \text{..........} \quad (2.18)$$

where p_f is the fluid pressure within the hydraulic fracture.

The boundary condition of the problem is:

$$q(0,t) = q_i = const \quad \text{..........} \quad (2.19)$$

where q_i is the fluid injection rate at the wellbore (x=0). At the fracture tip, it is assumed that the net fluid pressure becomes zero, which can be expressed as:

$$p_f(x_l,t) - \sigma_n = 0 \quad \text{..........} \quad (2.20)$$

where σ_n is the far-field stress normal to the fracture surface. Initially, the fracture is closed, so the initial condition is:

$$\omega(x,0)=0 \quad (2.21)$$

Eq. (2.17) is discretized using the implicit finite difference method from time t_m to t_{m+1}:

$$\frac{\omega_i^{m+1}-\omega_i^m}{\Delta t}=\frac{q_{i+1/2}^{m+1}-q_{i-1/2}^{m+1}}{\Delta x} \quad (2.22)$$

where $\Delta t = t_{m+1}-t_m$ and $\Delta x = x_{i+1/2}-x_{i-1/2}$.

Let $\omega_{i+1/2}^{m+1}=\frac{\omega_{i+1}^{m+1}+\omega_i^{m+1}}{2}$, and $\omega_{i-1/2}^{m+1}=\frac{\omega_{i-1}^{m+1}+\omega_i^{m+1}}{2}$. According to Eq. (2.18) we can get:

$$q_{i+1/2}=\frac{(\omega_{i+1}^{m+1}+\omega_i^{m+1})^3}{8\times 12\mu}\frac{p_{i+1}^{m+1}-p_i^{m+1}}{\Delta x} \quad (2.23)$$

$$q_{i-1/2}=\frac{(\omega_i^{m+1}+\omega_{i-1}^{m+1})^3}{8\times 12\mu}\frac{p_i^{m+1}-p_{i-1}^{m+1}}{\Delta x} \quad (2.24)$$

Substituting Eq. (2.24) into Eq. (2.22) yields:

$$\omega_i^{m+1}-\omega_i^m = \frac{\Delta t}{(8)\times 12\mu(\Delta x)^2}\left[(\omega_{i+1}^{m+1}+\omega_i^{m+1})^3 p_{i+1}^{m+1}-(\omega_{i+1}^{m+1}+\omega_i^{m+1})^3 p_i^{m+1}-(\omega_i^{m+1}+\omega_{i-1}^{m+1})^3 p_i^{m+1}+(\omega_i^{m+1}+\omega_{i-1}^{m+1})^3 p_{i-1}^{m+1}\right] \quad (2.25)$$

The boundary conditions in Eq. (2.19) and (2.20) can be written in discretized form into:

For *i*=1,

$$q^m{}_{1/2}=q_l \quad (2.26)$$

For *i*=*n*,

$$p^m{}_n=\sigma_n \quad (2.27)$$

Initial condition can be written into:

$$\omega_i^0=\omega(x_i,0)=0 \quad (2.28)$$

Combining Eq. (2.25), (2.26), (2.27) and (2.28) yields:

$$a_i p_{i-1}^{m+1} + b_i p_i^{m+1} + c_i\, p_{i+1}^{m+1} = d_i \tag{2.29}$$

where

$$\left.\begin{aligned} a_i &= (\omega_i^{m+1} + \omega_{i-1}^{m+1})^3 \\ b_i &= -(\omega_i^{m+1} + \omega_{i+1}^{m+1})^3 - (\omega_i^{m+1} + \omega_{i-1}^{m+1})^3 \\ c_i &= (\omega_i^{m+1} + \omega_{i+1}^{m+1})^3 \\ d_i &= \frac{\omega_i^{m+1} - \omega_i^m}{(\Delta t / 8\mu'(\Delta x)^2)} \end{aligned}\right. \quad \text{for } i\text{=2 to } n\text{-1} \tag{2.30}$$

where $\mu' = 12\mu$

$$a_n = 0, b_n = 1, d_n = \sigma_{\infty,n} \tag{2.31}$$

and

$$\begin{aligned} a_1 &= 0 \\ b_1 &= -(\omega_1^{m+1} + \omega_2^{m+1})^3 \\ c_1 &= (\omega_1^{m+1} + \omega_2^{m+1})^3 \\ d_1 &= \frac{\omega_1^{m+1} - \omega_1^m - \frac{\Delta t}{\Delta x} q_l}{(\Delta t / 8\mu'(\Delta x)^2)} \end{aligned} \tag{2.32}$$

When the fluid pressure along the fracture has a prescribed value and uniformly distributed, the fracture width can be explicitly solved for by using the DD method as described Section **2.1.** However, the main challenge for modeling a Newtonian fluid flow model is to determine two unknown and dependent variables, the fracture width and the fluid pressure distribution along the fracture. The two underlying coupling mechanisms are: 1) The fracture aperture (as mechanical response of the reservoir rock) changes with the applied loading which is imposed on the fracture surfaces by the fluid pressure; 2) The fluid pressure and the resultant pressure gradient along the fracture are related to the fracture width according to the Poiseuille's law. An iterative process is needed to solve for the pressure distribution and the fracture aperture.

The iteration process can be explained as follows. During each time step, at k^{th} iteration between width and fluid pressure along the fracture, a trial solution for the fluid pressure $p_i^{m+1(k)} = p^{(k)}(x_i, t_{m+1})$ along the fracture is first used then, the DD method as described in Section **2.1** is used to solve the fracture width $\omega_i^{m+1(k)} = \omega^{(k)}(x_i, t_{m+1})$. This fracture width $\omega_i^{m+1(k)} = \omega^{(k)}(x_i, t_{m+1})$ is then substituted into Eq. (2.29) to solve for a new fluid pressure distribution $p_i^{m+1(k+1/2)} = p^{(k+1/2)}(x_i, t_{m+1})$ along the fracture. The process is continued within each time step until convergence i.e., when the difference between the two sets of width/fluid pressure approaches zero (or is less than a very small value).

To shorten and stabilize the iteration process, a relaxation factor α is used to get the fluid pressure for the next cycle of iteration.

$$p_i^{m+1(k+1)} = p_i^{m+1(k)} + \alpha(p_i^{m+1(k+1/2)} - p_i^{m+1(k)}) \quad \text{......} \quad (2.33)$$

The fracture length is increased by a fixed element size, and the time length is adjustable within each time step. The length of each time step is first assumed to be a certain value, and then the facture volume is calculated by numerical integration of the fracture length and calculated values of fracture width. If the volume pumped is greater /smaller than the assumed time length, then the time is increased/decreased by small increments. The newly adjusted time length is then used to calculate the next approximation of fracture width. This procedure is repeated until convergence criterion meets i.e., when the difference between two sets of time length approaches zero.

3 MODEL VERIFICATION

3.1 Evaluation of SIF

3.1.1 Different SIF Calculated by Using Different Lengths of Tip Element, Lengths of Ordinary Element and *d* (Length of FPZ)

The stress intensity factor (SIF) is a parameter used to characterize the stress field near the crack tip, and it is used to evaluate the stress ahead of the crack tip and further determine fracture propagation direction and mode according to the structural criterion as explained in Section **2.3**. The magnitude of SIF depends on the geometric configuration, the size and location of the crack and loading conditions of the body. SIF can be obtained by using analytical, numerical and experimental methods. In a boundary element modeling, SIF is usually calculated in two approaches. One is using the DD at the crack tip as expressed by the following equation (Yan 2004):

$$\begin{aligned} K_I &= \frac{G}{4(1-\nu)}\sqrt{\frac{2\pi}{r}}D_n(r) \\ K_{II} &= \frac{G}{4(1-\nu)}\sqrt{\frac{2\pi}{r}}D_s(r) \end{aligned} \qquad \text{..............} \quad (3.1)$$

where $D_n(r)$ and $D_s(r)$ are the normal and shear components of DD at a distance r from the crack tip.

The other approach for calculating SIF at the crack tip is using the stresses ahead of the crack tip by the following equation (Rice 1968):

$$\begin{aligned} K_I &= \sigma_n(r)\sqrt{2\pi r} \\ K_{II} &= \sigma_s(r)\sqrt{2\pi r} \end{aligned} \qquad (3.2)$$

where $\sigma_n(r)$ and $\sigma_s(r)$ are the normal and shear components of the stresses at the point located along the tangent of the crack, and at a distance r from the crack tip as shown in **Fig. 3.1.**

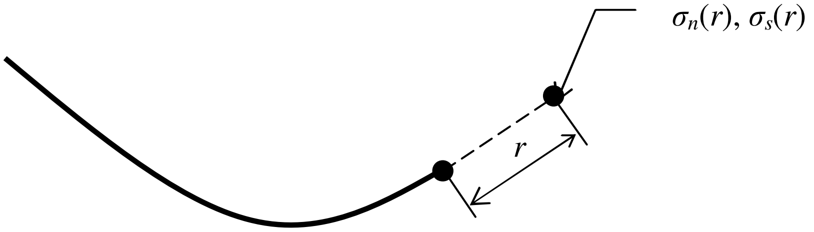

Fig. 3.1 SIF calculated based on the stresses ahead of the crack tip.

The program has been extended to include tip element at each crack tip, and fracture propagation has been enabled from both crack tips. To verify the accuracy of the code for calculating SIF at the crack tip, the SIF of a straight crack in an infinite elastic space, as shown in **Fig. 3.2**, was checked against the analytical value by using different lengths of tip element, lengths of ordinarily element and d (length of FPZ).

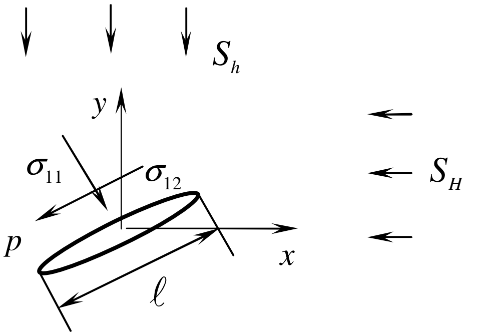

Fig. 3.2 A slanted pressurized crack under biaxial stresses in an infinite elastic medium.

The analytical solution for SIF at the crack tip is (Woo and Ling 1984):

$$K_I = \sigma_I \sqrt{\pi a} \quad (3.3)$$

$$K_{II} = \sigma_{II} \sqrt{\pi a} \quad (3.4)$$

where $a = \frac{\ell}{2}$ and

$$\sigma_I = \sigma_{11} - p \quad (3.5)$$

$$\sigma_{II} = \sigma_{12} \quad (3.6)$$

σ_{11} and σ_{12} are far-field stresses with respect to the local coordinates of the crack. SIFs calculated based on DDs by using Eq. (3.1) and on stresses by using Eq. (3.2) are shown and compared in **Table 3.1**.

Table 3.1 SIFs calculated by using DDs and stresses

SIF calculated based on DDs										
	$\ell_{tip} = 0.6\ell$		$\ell_{tip} = 0.5\ell$		$\ell_{tip} = 0.4\ell$		$\ell_{tip} = 0.3\ell$		$\ell_{tip} = 0.2\ell$	
	$\ell_{ord} = 0.1\ell$		$\ell_{ord} = 0.1\ell$		$\ell_{ord} = 0.1\ell$		$\ell_{ord} = 0.1\ell$		$\ell_{ord} = 0.1\ell$	
K_I	1.34E+06	0.71%	1.30E+06	0.69%	1.25E+06	0.78%	1.21E+06	1.17%	1.17E+06	2.35%
K_{II}	1.06E+06	0.70%	1.02E+06	0.68%	9.86E+05	0.78%	9.51E+05	1.16%	9.21E+05	2.34%
	$\ell_{tip} = 0.1\ell$		$\ell_{tip} = 0.075\ell$		$\ell_{tip} = 0.05\ell$		$\ell_{tip} = 0.05\ell$			
	$\ell_{ord} = 0.1\ell$		$\ell_{ord} = 0.1\ell$		$\ell_{ord} = 0.1\ell$		$\ell_{ord} = 0.05\ell$			
K_I	1.17E+06	7.22%	1.19E+06	10.89%	1.26E+06	18.43%	1.17E+06	7.61%		
K_{II}	9.20E+05	7.26%	9.40E+05	10.90%	9.91E+05	18.43%	9.24E+05	7.69%		
SIF calculated based on stresses, *d*=0.01*l*										
	$\ell_{tip} = 0.2\ell$		$\ell_{tip} = 0.1\ell$		$\ell_{tip} = 0.075\ell$		$\ell_{tip} = 0.05\ell$		$\ell_{tip} = 0.05\ell$	
	$\ell_{ord} = 0.1\ell$		$\ell_{ord} = 0.1\ell$		$\ell_{ord} = 0.1\ell$		$\ell_{ord} = 0.1\ell$		$\ell_{ord} = 0.05\ell$	
K_I	1.02E+06	-10.34%	1.02E+06	-6.75%	1.03E+06	-4.05%	1.08E+06	1.28%	1.01E+06	-7.30%
K_{II}	8.07E+05	-10.35%	8.00E+05	-6.72%	8.13E+05	-4.04%	8.47E+05	1.29%	7.96E+05	-7.23%
SIF calculated based on stresses, *d*=0.05*l*										
	$\ell_{tip} = 0.2\ell$		$\ell_{tip} = 0.1\ell$		$\ell_{tip} = 0.075\ell$		$\ell_{tip} = 0.05\ell$		$\ell_{tip} = 0.05\ell$	
	$\ell_{ord} = 0.1\ell$		$\ell_{ord} = 0.1\ell$		$\ell_{ord} = 0.1\ell$		$\ell_{ord} = 0.1\ell$		$\ell_{ord} = 0.05\ell$	
K_I	8.6E+05	-25.05%	8.40E+05	-22.88%	8.47E+05	-21.34%	8.65E+05	-18.60%	8.27E+05	-24.15%
K_{II}	6.7E+05	-25.06%	6.62E+05	-22.86%	6.67E+05	-21.33%	6.81E+05	-18.59%	6.51E+05	-24.10%

It can be observed that SIFs calculated by stress formulae generally improve as the length of tip element gets smaller. The optimum ratio of ℓ_{tip} to ℓ_{ord} when the error is the smallest is 0.5. The error is the smallest when ℓ_{tip}=0.05ℓ, ℓ_{ord}=0.1ℓ, and d=0.01ℓ, which is about 1.28% when compared with the analytical values. However, the results are not very good for SIFs calculated by using large d values (when $d=0.05\ell$), as SIF calculated based on the stress formulae is only valid in a very mall vicinity of the crack tip. The type of DD we used is real DD with equal length ordinary elements, so it is less accurate in estimating the stress ahead of the crack tip compared with the complex variable Boundary Element Method used by Dobroskok et al. (2005).

The accuracy of SIF calculation based on DDs at the crack tip element is dependent on the selection of ℓ_{tip} and ℓ_{ord}. The most accurate estimate of K_I and K_{II} are obtained when $\ell_{tip} = 0.5\ell$ and $\ell_{ord} = 0.1\ell$. The SIF calculated by using DD formulae when $\ell_{tip} = 0.1\ell_{ord}$ and $l_{ord} = 0.1\ell$ gives an error of about 7.22%, which is acceptable for numerical estimates of rock engineering problems, and that is what we used in the following numerical calculation in this thesis.

Table 3.2 also shows that SIFs calculated by DD formulae have the same error for cracks slanted at different angles with respect to *x*-axis. Therefore the crack propagation direction, which is determined by the value of K_I / K_{II}, can be modeled exactly.

Table 3.2 SIFs calculated based on DDs

	Analytical			Numerical			Error (%)		
Angle	KI	KII	KII/KI	KI	KII	KII/KI	KI	KII	KII/KI
30	0.4431	0.7675	1.7321	0.4752	0.8230	1.7320	7.23%	7.23%	0.00%
45	0.8862	0.8862	1.0000	0.9503	0.9503	1.0000	7.23%	7.23%	0.00%
60	1.3293	0.7675	0.5774	1.4254	0.8230	0.5774	7.23%	7.23%	0.00%
90	1.7725	0.0000	0.0000	1.9006	0.0000	0.0000	7.23%	0.00%	0.00%

For both simplicity and accuracy, in the following numerical examples in this thesis, SIFs are calculated by choosing ℓ_{tip} and ℓ_{ord} to be 0.1ℓ (ℓ: the original half crack length) to avoid remeshing of the elements with crack growth, and by using DD formulae, as SIFs calculated by this approach is independent on the selection of *d*. SIF calculated by the stress formulae will be dependent on the selection of *d*, so this approach is not adopted in the following numerical examples.

3.1.2 Selection of *d* (Length of FPZ)

Another important parameter in the modeling of the crack propagation process is *d*, the characteristic length of the fracture process zone. **Fig. 3.3** illustrates a macro-crack (continuous traction-free crack) with its surrounding zone in a rock. The damaged zone ahead of the traction-free crack is referred to as the fracture process zone (FPZ) and it plays an important role in the analysis of growth of the crack. Within the FPZ many micro-failure mechanisms including matrix microcracking, matrix interface debonding, crack deviation and branching take place. A FPZ is called a small FPZ if $d / \ell \leq 0.1$ and non-small for $d / \ell > 0.15$ (ℓ: half length of the crack) (2005).

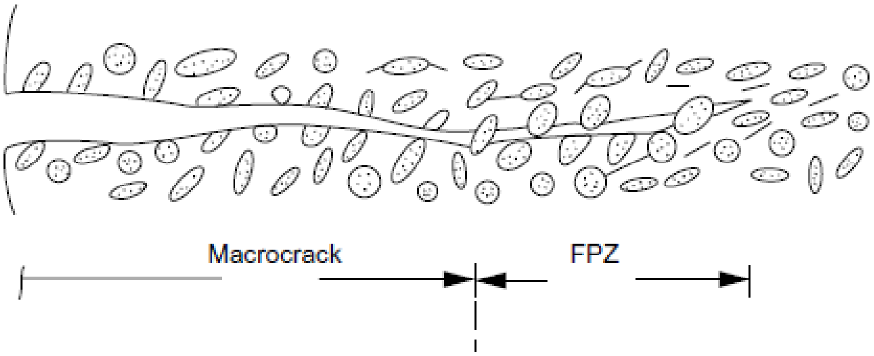

Fig. 3.3 A fracture process zone (Gdoutos 2005).

The length of the FPZ, *d*, depends on the geometry and size of the structure, the type of material, and the considered scale of study, and in practice they are to be found experimentally. As shown in Dobroskok et al (2005), fracture would display different propagation trajectories for a small FPZ case ($d/\ell = 0.05$) and a non-small FPZ case ($d/\ell = 0.25$). It is important to carefully select this value in order to get reliable modeling results.

As another test case, the propagation of a slanted pressurized crack under biaxial stresses in an elastic space was modeled using different values of *d*, and the results are plotted in **Fig. 3.4.** (The input parameters were: half crack length ℓ =1m, minimum horizontal stress S_h=-0.5MPa, maximum horizontal stress S_H=-3MPa, internal fluid pressure within the fracture *p*=2.5MPa, cohesion *c*=2.2MPa, and tensile strength T_0=2.0MPa). The calculated crack trajectories are similar and crack propagates in Mode I in three cases of small FPZ: $d=0.1\ell$, $d=0.05\ell$, and $d=0.01\ell$. The modeling results are not sensitive to the variation of *d* as long as *d* falls in the small FPZ category.

However, when d is set to 0.5ℓ (non-small FPZ), the fracture does not propagate forward. Due to the singularity of the stress distribution around the crack tip, the calculated averaged driving forces around the tip is a function depending strongly on d. The averaged normal and shear driving force will decline very rapidly with the increase of d. Therefore, propagation may not occur if a very large d is selected.

Zhang (2002) showed that there is an empirical relation between Mode I fracture toughness and the tensile strength of the rock:

$$T_0 = 6.88\, K_{IC} \qquad (3.7)$$

which is valid for general rocks from soft to hard under the condition of quasi-static or low-speed impact loading. As pointed by Dobroskok (2005) for a small FPZ,

$$K_{IC} = \sqrt{\frac{\pi\, d}{2}}\, T_0 \qquad (3.8)$$

Therefore, it can be estimated that $d \approx 0.013\text{m}$. For most cracks of length over 1m, d is within the range of a small FPZ. As we use real DD with equal length ordinary elements, the stress ahead of the crack tip determined by SIF formulae Eq.(2.15) and (2.16) is only valid for the very small vicinity of the crack tip. Therefore, in this thesis we only focused on cases of small FPZ.

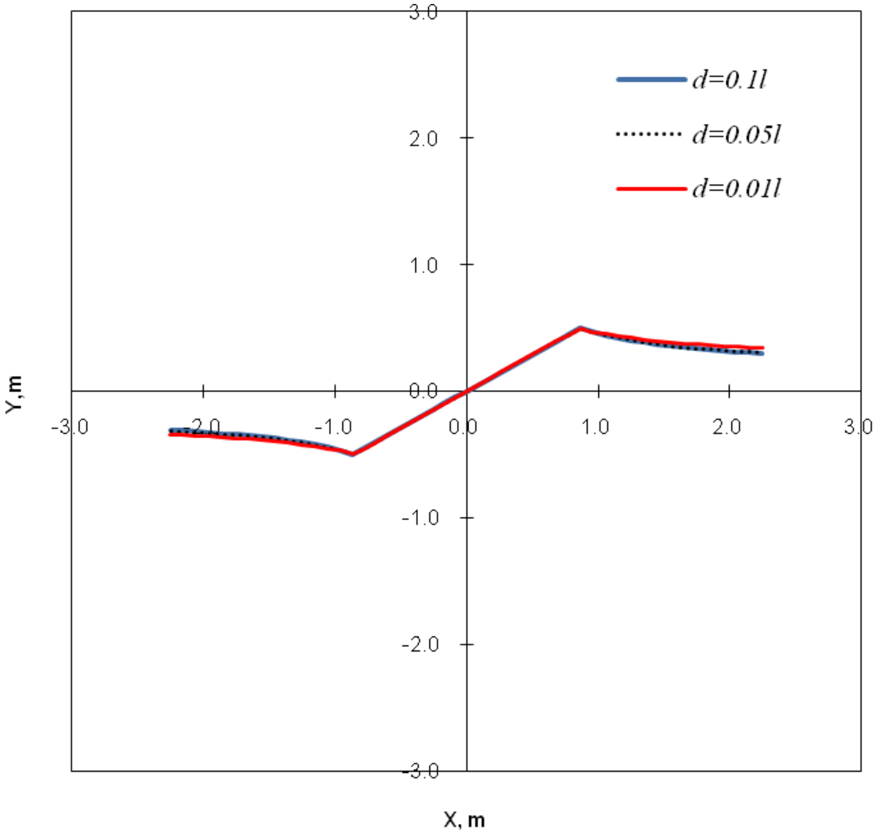

Fig. 3.4 Fracture trajectories calculated with different *d* for a slanted pressurized crack under biaxial stresses in an infinite elastic medium.

3.2 Fracture Propagation (Elastic Case)

3.2.1 Crack Propagation Under Biaxial Stress in an Infinite Elastic Rock

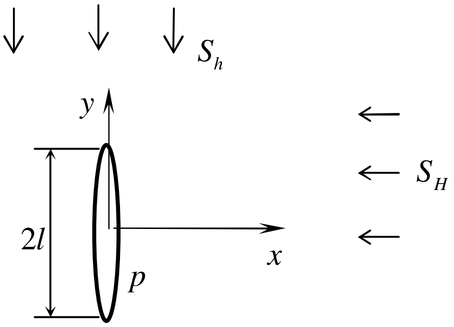

Fig. 3.5 An initially straight pressurized crack under biaxial stresses.

Using the example in Dong and de Pater's paper (2001), the propagation path of a pressurized crack under biaxial compressive stresses in an infinite elastic rock is simulated (see **Fig. 3.5**). The input parameters are listed in **Table 3.3**. The maximum circumferential stress criterion was used in our example as in Dong and de Pater's paper. Constant pressure distribution inside the crack was assumed.

Table 3.3 Input parameters in Section 3.2.1

E	Young's modulus	2.0×10^{04}	MPa
l	initial half crack length	0.02	m
υ	Poisson's ratio	0.2	
K_{IC}	Mode I critical stress intensity factor	0.6	MPa·m$^{1/2}$

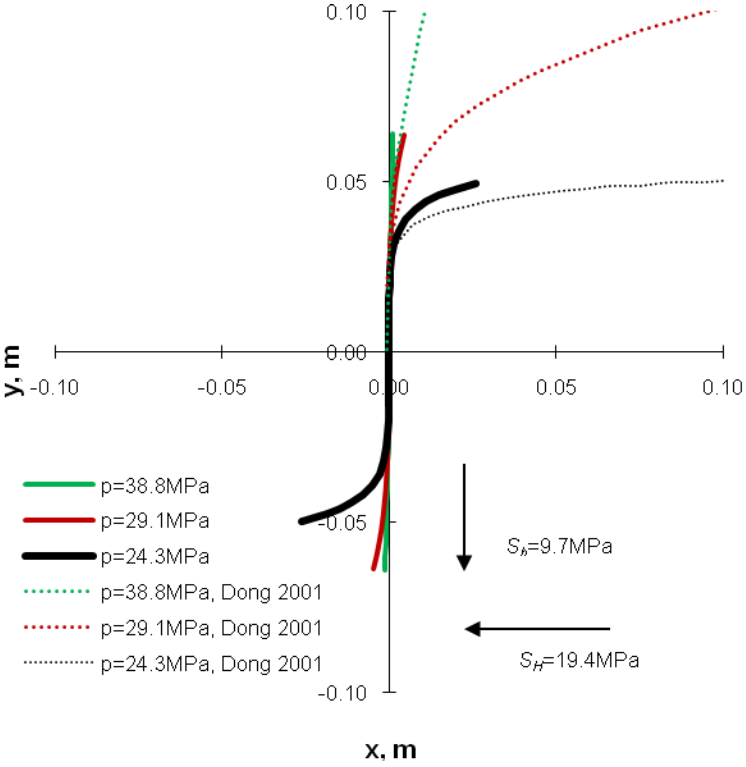

Fig. 3.6 Crack trajectories under different internal pressures.

Fig. 3.6 shows the reorientation of crack trajectories under different internal pressures (*p*=24.3, 29.1 38.8 MPa) in the crack. **Fig. 3.7** shows the reorientation of crack trajectories under different maximum horizontal stresses (S_H=22.6, 19.4, 9.7 MPa). Similarly as those obtained by Dong (2001), the crack would reorient from its original direction (the direction of S_h) and propagate along the direction of $\mathrm{S_H}$ under the far-field compressive stresses. Different curves show that for crack with lower internal pressure or for a stress field with bigger difference between maximum horizontal stress S_H and minimum horizontal stress S_h (higher degrees of anisotropy of the stress field), the direction of the crack path change more quickly.

As quadratic boundary elements were used by Dong while we used constant elements along the crack and tip element implemented at the crack tip, the preciseness of the fracture tip SIF calculation and our model results of fracture paths are slightly from those predicted by Dong.

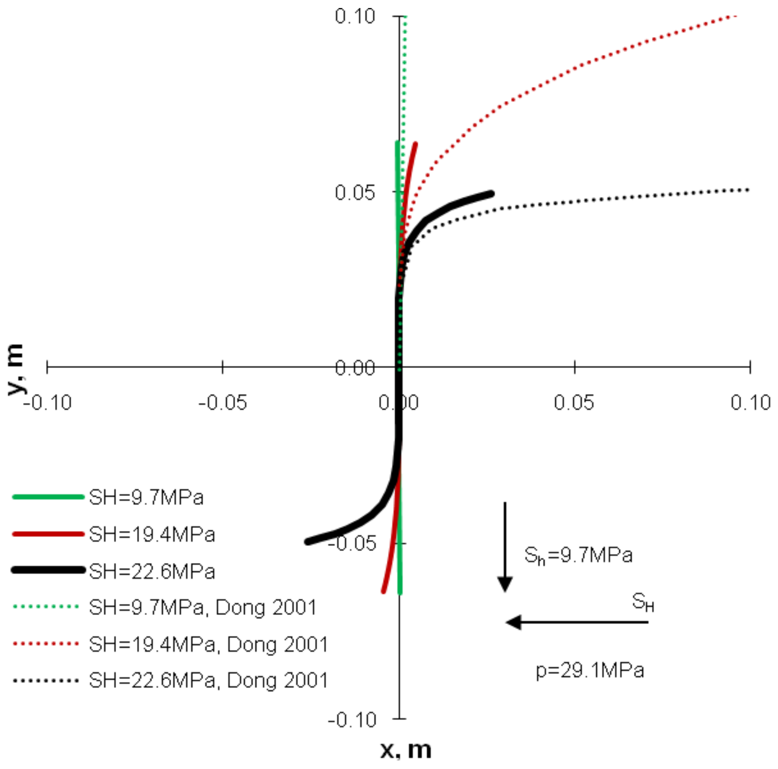

Fig. 3.7 Crack trajectories under different maximum horizontal stresses.

3.2.2 Crack Propagation under Uniaxial Stress in an Infinite Elastic Medium

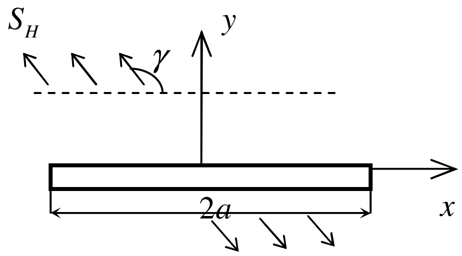

Fig. 3.8 A line crack under uniaxial stress in an infinite elastic medium.

We also investigated the propagation of a straight line crack with a length of $2a = 2\text{m}$ in an infinite elastic space under plane-strain conditions as shown in **Fig. 3.8.** The crack surfaces are subjected to far-field tension, S_H, at different angles γ with respect to the x-axis. We modeled the crack with l_{tip} and l_{ord} equal to $0.1l$ and d=0.01l. To compare our results with previous studies, the maximum circumferential stress criterion was also used in the program. In view of the symmetry in geometry and mechanical loading of the problem, only half of the crack is plotted in **Fig. 3.9.** The crack grows in the direction perpendicular to the direction of far-field uniaxial tension as the crack is subjected to the greatest tension at this direction and can propagate most easily. The model results match the results in Mogilevskaya's (2005) paper.

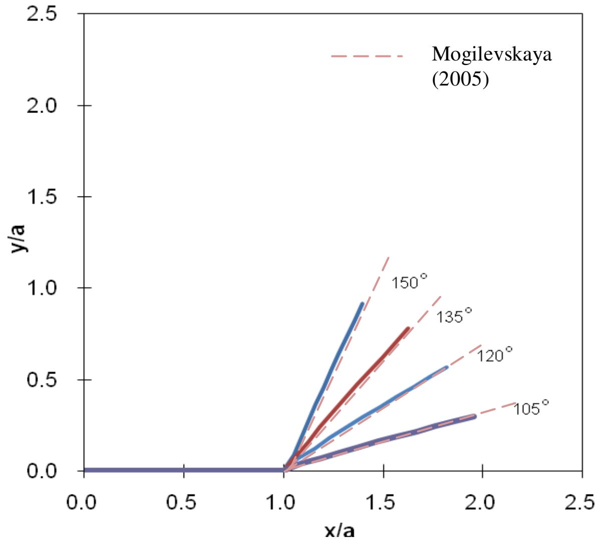

Fig. 3.9 Crack growth under uniaxial stress in an infinite elastic medium.

4 JOINT ELEMENT

4.1 Joint Element

For many problems in rock mechanics, the total stresses at any point in the rock can be represented as the sum of the **initial stresses** and the stress changes at that point, which is usually called the **induced stress** (Crouch and Starfield 1983).

$$\sigma_{ij} = (\sigma_{ij})_0 + \sigma_{ij}^{'} \quad \text{..........} \quad (4.1)$$

Similarly, total displacement can be represented as the **initial displacement** and the **induced displacement**.

$$\sigma_{ij} = (\sigma_{ij})_0 + \sigma_{ij}^{'} \quad \text{..........} \quad (4.2)$$

4.1.1 Joint Stick Mode (Elastic Joint Element)

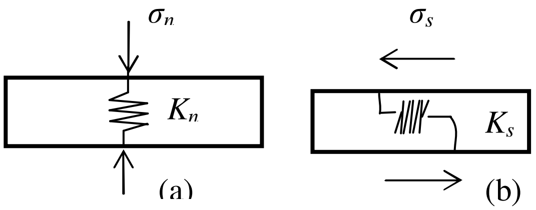

Fig. 4.1 Representation of an elastic joint element (a) normal stiffness; (b) shear stiffness.

4.1.1.1 Joint Element Excluding Initial Joint Deformation

For an elastic joint element (shown in **Fig. 4.1)** with zero initial deformations, the joint elements deform only in response to the induced stress caused for example by an approaching hydraulic fracture. The relation between tractions and the DD's on the joint surface are (Crouch and Starfield 1983):

$$\begin{bmatrix}\overset{i}{\sigma}{}'_n\\ \overset{i}{\sigma}{}'_s\end{bmatrix} = -\begin{bmatrix}K_n^i & 0\\ 0 & K_s^i\end{bmatrix}\begin{bmatrix}\overset{i}{D}{}'_n\\ \overset{i}{D}{}'_s\end{bmatrix} \quad \ldots\ldots\ldots\ldots\ldots\ldots\ldots\ldots\ldots\ldots\ldots\ldots (4.3)$$

where $\overset{i}{\sigma}{}'_n$, $\overset{i}{\sigma}{}'_s$ are the induced normal and shear stresses, and $\overset{i}{D}{}'_n$, $\overset{i}{D}{}'_s$ are the components of induced normal and shear DD vector on the i^{th} element of the joint surface. $K_n{}^i$ and $K_s{}^i$ are the normal and the shear rigidity of the joint. For a joint (having N elements) undergoing elastic deformation, the induced stresses on any element *i* are given by (Crouch and Starfield 1983):

$$\left.\begin{aligned}\overset{i}{\sigma}{}'_s &= \sum_{j=1}^{N}\left(\overset{ij}{A}_{ss}\,\overset{j}{D}{}'_s + \overset{ij}{A}_{sn}\,\overset{j}{D}{}'_n\right)\\ \overset{i}{\sigma}{}'_n &= \sum_{j=1}^{N}\left(\overset{ij}{A}_{ns}\,\overset{j}{D}{}'_s + \overset{ij}{A}_{nn}\,\overset{j}{D}{}'_n\right)\end{aligned}\right\} \text{for } i\text{=1 to N} \quad \ldots\ldots\ldots\ldots\ldots\ldots\ldots\ldots (4.4)$$

where $\overset{ij}{A}_{ss}$, $\overset{ij}{A}_{sn}$, $\overset{ij}{A}_{ns}$, $\overset{ij}{A}_{nn}$ are the boundary influencing coefficients as defined in Eq. (2.5). From Eq. (4.3) and (4.4), we can rewrite the system of equations in the following form:

$$0 = (\overset{i}{K}_s)(\overset{i}{D}{}'_s) + \sum_{j=1}^{N}\left[\overset{ij}{A}_{ss}\,\overset{j}{D}{}'_s + \overset{ij}{A}_{sn}\,\overset{j}{D}{}'_n\right]$$

for i=1 to N.. (4.5)

$$0 = (\overset{i}{K}_n)(\overset{i}{D}{}'_n) + \sum_{j=1}^{N}\left[\overset{ij}{A}_{ns}\,\overset{j}{D}{}'_s + \overset{ij}{A}_{nn}\,\overset{j}{D}{}'_n\right]$$

which can be simplified as:

$$\begin{bmatrix}0\\0\end{bmatrix} = \begin{bmatrix}A_{ss}+K_s & A_{sn}\\ A_{ns} & A_{nn}+K_n\end{bmatrix}\begin{bmatrix}D'_s\\ D'_n\end{bmatrix} = \left[A+K\right]\begin{bmatrix}D'_s\\ D'_n\end{bmatrix} \quad \text{...} \quad (4.6)$$

By introducing the **total joint deformation** ($\overset{i}{D}_s$ and $\overset{i}{D}_n$), which can be expressed as the sum of the **initial total joint deformation** ($(\overset{i}{D}_s)_0$ and $(\overset{i}{D}_n)_0$) and the **induced deformation** (Crouch and Starfield 1983):

$$\begin{aligned}\overset{i}{D}_s &= (\overset{i}{D}_s)_0 + \overset{i}{D}{}'_s\\ \overset{i}{D}_n &= (\overset{i}{D}_n)_0 + \overset{i}{D}{}'_n\end{aligned} \quad \text{..} \quad (4.7)$$

and assuming zero **initial joint deformation** for a joint, we write Eq. (4.5) as:

$$0 = (\overset{i}{K}_s)(\overset{i}{D}_s) + \sum_{j=1}^{N}\left[\overset{ij}{A}_{ss}\,\overset{j}{D}_s + \overset{ij}{A}_{sn}\,\overset{j}{D}_n\right]$$

for i=1 to N.. (4.8)

$$0 = (\overset{i}{K}_n)(\overset{i}{D}_n) + \sum_{j=1}^{N}\left[\overset{ij}{A}_{ns}\,\overset{j}{D}_s + \overset{ij}{A}_{nn}\,\overset{j}{D}_n\right]$$

This type of joint element has the assumption that the natural fracture under consideration has already reached equilibrium with geologic time and is closed and does not deform elastically or plastically under far-field stress prior to the process of hydraulic fracturing. As the initial deformation on a fault was assumed to be zero, the initial stress field around a hydraulic fracture was not affected by the presence of the fault (Crouch and Starfield 1983).

4.1.1.2 Joint Element Including Initial Joint Deformation

In Section **4.1.1.1**, we used a joint element without considering the initial joint deformation, which means the initial stress field prior to fracture propagation was not affected by the presence of the fault. Another type of joint element would include initial joint deformation prior to fracture propagation process. In this type of scenario, the initial stress field is disturbed by the initial deformation of the fault under the action of the far-field stress prior to the fracture propagation process. The joint is deformed (possibly plastically) under initial far-field stresses prior to the process of hydraulic fracturing.

The **initial total stress** can be expressed as the sum of the far-field stress and the **initial induced stress** (Crouch and Starfield 1983).

$(\sigma_{ij})_0 = (\sigma_{ij})_0^{\infty} + (\sigma_{ij}^{'})_0$ .... (4.9)

(For a joint **exclude initial joint deformation**, we can obtain that

$(\sigma_{ij})_0 = (\sigma_{ij})_0^{\infty}$ .... (4.10))

Similarly, the **initial displacements** can be expressed as the sum of the far-field displacements and the **initial induced displacements**.

$$(u_i)_0 = (u_i)_0^{\infty} + (u_i^{'})_0 \tag{4.11}$$

For a joint system of N elements with elastic deformation, the **initial total stresses** at element *i* are (Crouch and Starfield 1983):

$$\begin{aligned} (\overset{i}{\sigma}_s)_0 &= -(\overset{i}{K}_s)(\overset{i}{D}_s)_0 \\ (\overset{i}{\sigma}_n)_0 &= -(\overset{i}{K}_n)(\overset{i}{D}_n)_0 \end{aligned} \tag{4.12}$$

where $(\overset{i}{D}_s)_0$ and $(\overset{i}{D}_n)_0$ are the **initial total joint deformation**. The initial induced stresses at element *i* are (Crouch and Starfield 1983):

$$\begin{aligned} (\overset{i}{\sigma}{}_s^{'})_0 &= \sum_{j=1}^{N}\left[\overset{ij}{A}_{ss}(\overset{j}{D}_s)_0 + \overset{ij}{A}_{sn}(\overset{j}{D}_n)_0 \right] \\ (\overset{i}{\sigma}{}_n^{'})_0 &= \sum_{j=1}^{N}\left[\overset{ij}{A}_{ns}(\overset{j}{D}_s)_0 + \overset{ij}{A}_{nn}(\overset{j}{D}_n)_0 \right] \end{aligned} \tag{4.13}$$

where $\overset{ij}{A}_{ss}$, $\overset{ij}{A}_{sn}$, $\overset{ij}{A}_{ns}$, $\overset{ij}{A}_{nn}$ are the boundary influencing coefficients as defined in Eq. (2.5). Combining Eq. (4.9), (4.12) and (4.13), we can obtain:

$$\begin{aligned} -(\overset{i}{\sigma}_s)_0^{\infty} &= (\overset{i}{K}_s)(\overset{i}{D}_s)_0 + \sum_{j=1}^{N}\left[\overset{ij}{A}_{ss}(\overset{j}{D}_s)_0 + \overset{ij}{A}_{sn}(\overset{j}{D}_n)_0 \right] \\ -(\overset{i}{\sigma}_n)_0^{\infty} &= (\overset{i}{K}_n)(\overset{i}{D}_n)_0 + \sum_{j=1}^{N}\left[\overset{ij}{A}_{ns}(\overset{j}{D}_s)_0 + \overset{ij}{A}_{nn}(\overset{j}{D}_n)_0 \right] \end{aligned} \quad \text{for } i\text{=1 to N} \tag{4.14}$$

which can be simplified as

$$\begin{bmatrix} -(\sigma_s)_0^\infty \\ -(\sigma_n)_0^\infty \end{bmatrix} = \begin{bmatrix} A_{ss}+K_s & A_{sn} \\ A_{ns} & A_{nn}+K_n \end{bmatrix} \begin{bmatrix} (D_s)_0 \\ (D_n)_0 \end{bmatrix} = \left[A+K\right] \begin{bmatrix} (D_s)_0 \\ (D_n)_0 \end{bmatrix} \text{ ....} (4.15)$$

Initial total joint deformation $(\overset{i}{D}_s)_0$ and $(\overset{i}{D}_n)_0$ can therefore be solved. The same form of equation can also be derived in relation to the total joint deformation D_s and D_n (Crouch and Starfield 1983):

$$\left.\begin{array}{l} -(\overset{i}{\sigma}_s)_0^\infty = (\overset{i}{K}_s)(\overset{i}{D}_s) + \sum_{j=1}^{N} \left[\overset{ij}{A}_{ss}(\overset{j}{D}_s) + \overset{ij}{A}_{sn}(\overset{j}{D}_n) \right] \\ -(\overset{i}{\sigma}_n)_0^\infty = (\overset{i}{K}_n)(\overset{i}{D}_n) + \sum_{j=1}^{N} \left[\overset{ij}{A}_{ns}(\overset{j}{D}_s) + \overset{ij}{A}_{nn}(\overset{j}{D}_n) \right] \end{array}\right. \text{ for } i\text{=1 to N ....} (4.16)$$

In this assumption, the mechanical response of a natural fracture under far-field stresses would distort the initial stress field prior to the propagation of hydraulic fracture.

4.1.2 Joint Slip Mode

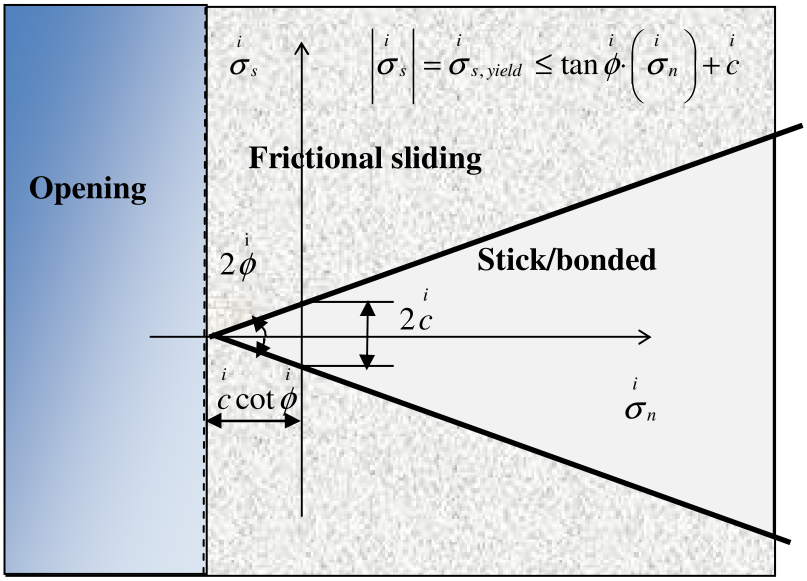

Fig. 4.2 Mohr diagram for a MC joint element under different contact mode under different stress conditions.

During elastic deformation, there is a constraint between the normal and shear stresses across the joint, which is given by the Mohr-Coulomb condition (**Fig. 4.2).** The total shear stress across a Mohr-Coulomb joint element cannot exceed the value specified by Eq. (4.17) (Crouch and Starfield 1983)**.**

$$\left|\overset{i}{\sigma}_s\right| \le \overset{i}{\sigma}_{s,yield} = \tan\overset{i}{\phi}\cdot\left(\overset{i}{\sigma}_n\right)+\overset{i}{c} \quad \text{.......} \quad (4.17)$$

where $\overset{i}{\phi}$ is the angle of friction, and $\overset{i}{c}$ is the cohesion. It requires that the element be allowed to undergo a certain amount of inelastic deformation or permanent slip, when the total shear stress on a joint element, $\left|\overset{i}{\sigma}_s\right|$, exceeds the total yield stress $\overset{i}{\sigma}_{s,yield}$.

The simulation of the joint displacements and stresses under yield condition is explained as follows. Suppose the current values of the DD components on element *i* are $\overset{i}{D}{}_n^{'}$, $\overset{i}{D}{}_s^{'}$ (**if initial joint deformation is excluded**). If no inelastic deformation occurred during this or any previous loading the total normal stress and shear stress are:

$$\begin{aligned} (\overset{i}{\sigma}_s)^{(k)}_{total} &= (\overset{i}{\sigma}_s)_0 + \overset{i}{\sigma}{}_s^{'} \\ (\overset{i}{\sigma}_n)^{(k)}_{total} &= (\overset{i}{\sigma}_n)_0 + \overset{i}{\sigma}{}_n^{'} \end{aligned} \tag{4.18}$$

Combining Eq. (4.18) with Eq. (4.4), we can get

$$\begin{aligned} (\overset{i}{\sigma}_s)_{total} &= (\overset{i}{\sigma}_s)_0 + \sum_{j=1}^{N}\left[\overset{ij}{A}_{ss}\overset{j}{D}{}_s^{'} + \overset{ij}{A}_{sn}\overset{j}{D}{}_n^{'}\right] \\ (\overset{i}{\sigma}_n)_{total} &= (\overset{i}{\sigma}_n)_0 + \sum_{j=1}^{N}\left[\overset{ij}{A}_{ns}\overset{j}{D}{}_n^{'} + \overset{ij}{A}_{nn}\overset{j}{D}{}_n^{'}\right] \end{aligned} \tag{4.19}$$

According to Eq. (4.17), the yield stress is:

$$\overset{i}{\sigma}_{s},_{yield} = \overset{i}{c} + (\overset{i}{\sigma}_n)_{total} \cdot \tan\overset{i}{\phi} \tag{4.20}$$

The magnitude of the shear stress $(\overset{i}{\sigma}_s)_{total}$ calculated from Eq. (4.19) cannot exceed the yield stress defined in Eq. (4.20). If the element is yielding, the total shear stress must equal the yield stress, so combining Eq. (4.19) and (4.20), we can get the governing equation for the shear deformation at the i^{th} joint element if joint yield occurs:

$$\pm\overset{i}{\sigma}_{s,yield} = (\overset{i}{\sigma}_s)_0 + \sum_{j=1}^{N}\left[\overset{ij}{A}_{ss}\,\overset{j}{D}_s' + \overset{ij}{A}_{sn}\,\overset{j}{D}_n'\right] \tag{4.21}$$

The positive value of the yield stress $\overset{i}{\sigma}_{s,yield}$ is used if the total shear stress $(\overset{i}{\sigma}_s)_{total}$ is positive, and the negative value is used if it is negative.

$$sign(\overset{i}{\sigma}_{s,yield}) = sign((\overset{i}{\sigma}_s)_{total}) \tag{4.22}$$

(In a convention system where compression is positive, σ_s is positive if point to the left with respect to the outward of a surface.)

The governing equation for the normal deformation is obtained from Eq. (4.5) for a joint element **excluding initial joint deformation:**

$$0 = (\overset{i}{K}_n)(\overset{i}{D}_n') + \sum_{j=1}^{N}\left[\overset{ij}{A}_{ns}\,\overset{j}{D}_s' + \overset{ij}{A}_{nn}\,\overset{j}{D}_n'\right] \tag{4.23}$$

The **initial joint deformation** is zero for a joint in this case, so $\overset{i}{D}_s = \overset{i}{D}_s'$ and $\overset{i}{D}_n = \overset{i}{D}_n'$ and Eq. (4.21), (4.23), and (4.10) can be written as:

$$\begin{aligned}
&\pm\overset{i}{\sigma}_{s,yield} - (\overset{i}{\sigma}_s)^{\infty} = \sum_{j=1}^{N}\left[\overset{ij}{A}_{ss}\,\overset{j}{D}_s + \overset{ij}{A}_{sn}\,\overset{j}{D}_n\right] \\
&0 = (\overset{i}{K}_n)(\overset{i}{D}_n) + \sum_{j=1}^{N}\left[\overset{ij}{A}_{ns}\,\overset{j}{D}_s + \overset{ij}{A}_{nn}\,\overset{j}{D}_n\right]
\end{aligned} \tag{4.24}$$

Similarly, the governing equation for the normal deformation is obtained from Eq. (4.14) for a joint element **including initial joint deformation:**

$$-(\overset{i}{\sigma}_n)^{\infty}_0 = (\overset{i}{K}_n)(\overset{i}{D}_n)_0 + \sum_{j=1}^{N}\left[\overset{ij}{A}_{ns}(\overset{j}{D}_s)_0 + \overset{ij}{A}_{nn}(\overset{j}{D}_n)_0\right] \text{ for } i\text{=1 to N} \quad\ldots\ldots\ldots\ldots (4.25)$$

Therefore, the corresponding system of equations is:

$$\begin{bmatrix} \pm\sigma^{\infty}_{s,yield} - \sigma^{\infty}_{s} \\ -\sigma^{\infty}_{n} \end{bmatrix} = \begin{bmatrix} A_{ss} & A_{sn} \\ A_{ns} & A_{nn} + K_n \end{bmatrix} \begin{bmatrix} (D_s)_0 \\ (D_n)_0 \end{bmatrix} \quad\ldots\ldots\ldots\ldots (4.26)$$

Similarly, the positive value of the yield stress $\overset{i}{\sigma}_{s,yield}$ is used if the total shear stress $(\overset{i}{\sigma}_s)_{total}$ is positive, and the negative value is used if it is negative, as expresses in Eq. (4.22).

The same form of equation can also be derived in relation to the total joint deformation D_s and D_n (Crouch and Starfield 1983):

$$\begin{aligned} \pm\overset{i}{\sigma}_{s,yield} - (\overset{i}{\sigma}_s)^{\infty} &= \sum_{j=1}^{N}\left[\overset{ij}{A}_{ss}\overset{j}{D}_s + \overset{ij}{A}_{sn}\overset{j}{D}_n\right] \\ -(\overset{i}{\sigma}_n)^{\infty} &= (\overset{i}{K}_n)(\overset{i}{D}_n) + \sum_{j=1}^{N}\left[\overset{ij}{A}_{ns}\overset{j}{D}_s + \overset{ij}{A}_{nn}\overset{j}{D}_n\right] \end{aligned} \quad\ldots\ldots\ldots\ldots (4.27)$$

4.1.3 Joint Opening Mode

Joint separation or tensile cracking is another possible failure mode for the joint element, as shown in **Fig. 4.2**. According to the Mohr-Coulomb condition, the tensile strength of a joint element can be expresses as:

$$\overset{i}{\sigma}_n = \overset{i}{c}\cot\overset{i}{\phi} \tag{4.28}$$

When the tensile stress across an element is greater than the tensile strength $\overset{i}{\sigma}_n$, the element needs to be allowed to crack open, in which the total normal and shear stresses become zero.

The total stress on element *i* is equal to the summation of far-field stress and induced stress:

$$(\overset{i}{\sigma})^{total} = (\overset{i}{\sigma})^{\infty} + (\overset{i}{\sigma})^{ind} \tag{4.29}$$

For a joint with N element, if element *i* becomes an open joint element, the equation takes the form:

$$\begin{aligned} 0-(\overset{i}{\sigma}_s)^{\infty} &= (\overset{i}{\sigma}_s)^{ind} = \sum_{j=1}^{N}\left[\overset{ij}{A}_{ss}\overset{j}{D}_s+\overset{ij}{A}_{sn}\overset{j}{D}_n\right] \\ 0-(\overset{i}{\sigma}_n)^{\infty} &= (\overset{i}{\sigma}_n)^{ind} = \sum_{j=1}^{N}\left[\overset{ij}{A}_{ns}\overset{j}{D}_s+\overset{ij}{A}_{nn}\overset{j}{D}_n\right] \end{aligned} \tag{4.30}$$

where A_{ss}, A_{sn}, A_{ns}, A_{nn} are the influence coefficient matrix accounting for the different positions and orientations of each element as defined in Eq. (2.5).

The simulation of the joint displacements and stresses under opening mode is as follows. Suppose the current values of the DD components at element *i* are $\overset{i}{D}_n$, $\overset{i}{D}_s$, if no opening mode occurred during this or any previous loading, calculate the total normal stress and shear stress along the joint. If $(\overset{i}{\sigma}_n)_{total} \ge \overset{i}{c} \cdot \cot \overset{i}{\phi}$, governing Eq. (4.30) is used to calculate $\overset{i}{D}_n$ and $\overset{i}{D}_s$.

4.2 Numerical Procedure

For problems involving joint elements, the contact type (stick, yield or open) and the displacements/stresses of each element along the joint are unknown. But if the contact mode is known, the corresponding governing equations relating the stresses and DD in Section 4.1 can be used to solve the DD at each element. Then, the stresses along the joint can be obtained and used to check the contact state again. If the new and the old contact modes are not in agreement, the assumed contact mode must be changed and DD must be solved again. The process will be stopped when the new and the assumed contact modes are the same and resultant DD and stresses along the joint converge. The iterative procedure can be summarized and listed as follows (see Appendix C for the detailed flowchart):

1) Within each time step, at *k*th iteration and at element *i*, first a joint contact type (for example stick mode) is assumed and the corresponding *k*th estimates for the normal and shear displacements $\overset{i}{D}_n^{(k)}$, $\overset{i}{D}_s^{(k)}$ at the *i*th element are obtained using Eq.(4.8) or (4.16).

2) The total normal and shear stresses at the *i*th element $(\overset{i}{\sigma}_n)_{total}^{(k)}$ and $(\overset{i}{\sigma}_s)_{total}^{(k)}$ are calculated by Eq. (4.31) as followed:

The total stress on a joint element in the system is obtained by adding the far-field stress σ^{∞} and the induced stress σ^{ind} resulting from the deformation of all elements present in the system which is:

$$\begin{aligned} \overset{i}{(\sigma_s)}{}^{(k)}_{total} &= \overset{i}{(\sigma_s)}{}^{\infty}_{0} + \sum_{j=1}^{N}\left[\overset{ij}{A}_{ss}\overset{j}{D}_s{}^{(k)} + \overset{ij}{A}_{sn}\overset{j}{D}_n{}^{(k)}\right] \\ \overset{i}{(\sigma_n)}{}^{(k)}_{total} &= \overset{i}{(\sigma_n)}{}^{\infty}_{0} + \sum_{j=1}^{N}\left[\overset{ij}{A}_{ns}\overset{j}{D}_s{}^{(k)} + \overset{ij}{A}_{nn}\overset{j}{D}_n{}^{(k)}\right] \end{aligned} \quad \text{.....................................} (4.31)$$

3) Calculate the yield stress at the k^{th} iteration according to Eq. (4.20). Then a check is made to see whether the yield/opening condition is met or not according to Eq. (4.20) and (4.28).

4) If the yield condition is met, Eq. (4.24) or (4.27) is used to compute the next approximation of the normal and shear displacements at the i^{th} elements $\overset{i}{D}_n{}^{(k+1)}$ and $\overset{i}{D}_s{}^{(k+1)}$.

5) If the yield condition is not met, Eq.(4.8) or (4.16) are used to compute the next approximation of the normal and shear displacements at the i^{th} elements, $\overset{i}{D}_n{}^{(k+1)}$ and $\overset{i}{D}_s{}^{(k+1)}$.

6) If the opening condition is met, Eq.(4.30) is used to compute the next approximation of the normal and shear displacements at the i^{th} elements, $\overset{i}{D}_n{}^{(k+1)}$ and $\overset{i}{D}_s{}^{(k+1)}$.

7) Continue to step 2) and check the contact mode again. If the new contact mode does not match the old one, the assumed contact mode must be changed and DD must be solved again. Continue the iterative process until DD and stresses at each element *i* converge (the difference between the stresses of two iteration cycles approaches zero or less than a small value: $Error = \sum_{i=1}^{N}((\overset{i}{\sigma}_n)_{total}^{(k+1)} - (\overset{i}{\sigma}_n)_{total}^{(k)})^2 + \sum_{i=1}^{N}((\overset{i}{\sigma}_s)_{total}^{(k+1)} - (\overset{i}{\sigma}_s)_{total}^{(k)})^2 \leq 10^{-3} Pa^2$) or maximum number of iteration is reached. The joint problems in our study can usually converge quickly before maximum number of iteration is reached.

8) We then continue to simulate the next time step and repeat the entire procedure.

4.3 Numerical Examples

4.3.1 Compression of a Single Joint

As an example, consider the initial deformation of a horizontal joint of length 2m under in-situ compressive stress S_h=1MPa (see **Fig. 4.3**). The normal and shear rigidity of the joint is set to be $K_n = 0.5\text{MPa/m}$ and $K_s = 0.25\text{MPa/m}$.

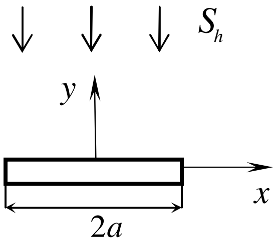

Fig. 4.3 Compression of a single joint.

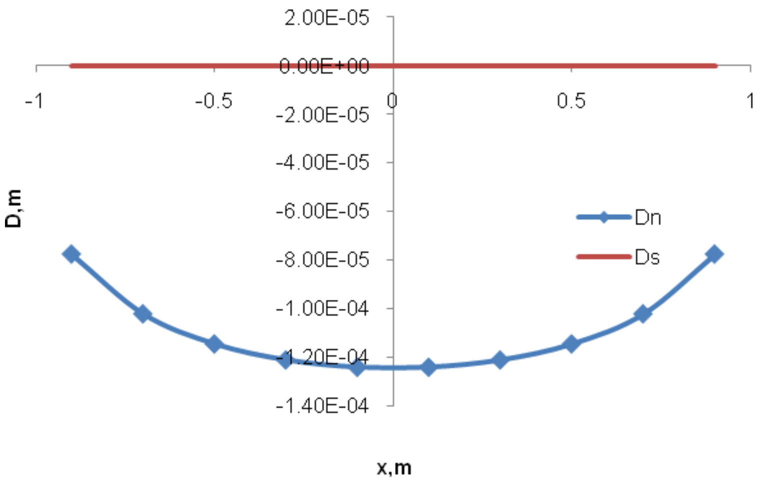

Fig. 4.4 Shear and normal displacement (D_s, D_n) along the joint surface (initial joint deformation included).

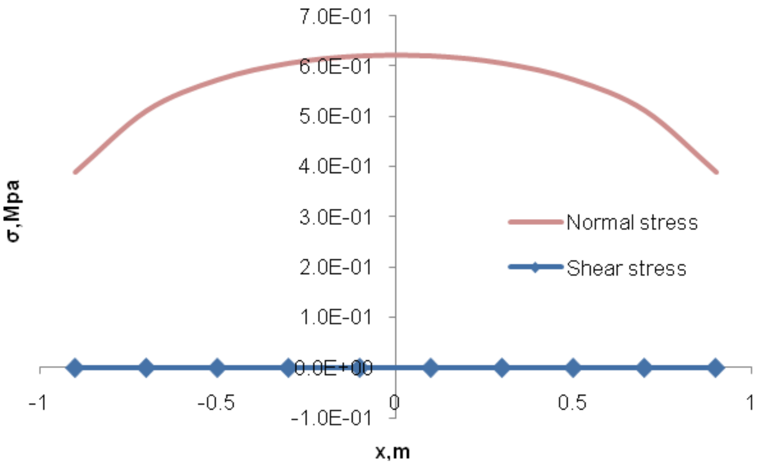

Fig. 4.5 Shear and normal stress along the joint surface (initial joint deformation included).

The mechanical response of a horizontal natural fracture under far-field compressive stresses calculated by using 10 equal length joint elements including initial joint deformation is shown in **Fig. 4.4** and **Fig. 4.5**. The governing equation **Eq. (4.15)** in this case is reduced to $-(\overset{i}{\sigma_n})_0^\infty = (\overset{i}{K_n})(\overset{i}{D_n}) + \sum_{j=1}^{N} \overset{ij}{A_{nn}}(\overset{j}{D_n})$ or $[\sigma_n^\infty] = [A_{nn} + K_n][-D_n]$. Therefore, uniaxial compressive stress will cause a negative D_n, indicating joint closure (it is assumed here that the initial aperture of the joint is much bigger than the maximum relative closure of the two joint surfaces, which is only at the order of 10^{-4}m. Therefore, the two joint surfaces have not come into contact or penetrated into each other.) The total normal stress along the joint surface is positive (compressive) and is smaller than the magnitude of the far-field compressive stress, as the joint acts like a spring that it absorbs some of the external force/energy by deformation (relative joint closure). (A joint with higher value of normal stiffness would deform less, and the degree of stress absorption is less.) Shear displacement and shear stress in this case is zero along the joint surface.

In comparison, the mechanical response of a horizontal natural fracture under far-field compressive stresses without considering the initial joint deformation is shown in **Fig. 4.6** and **Fig. 4.7**. As can be seen, the total normal and shear stresses on the joint corresponds to the far-field compressive stress S_h and zero far-field shear stress, respectively. As we have excluded the initial joint deformations under far-field stresses, assuming the joint has reached equilibrium under geological time, so the model yields results that there is no slippage or relative normal displacement along the joint.

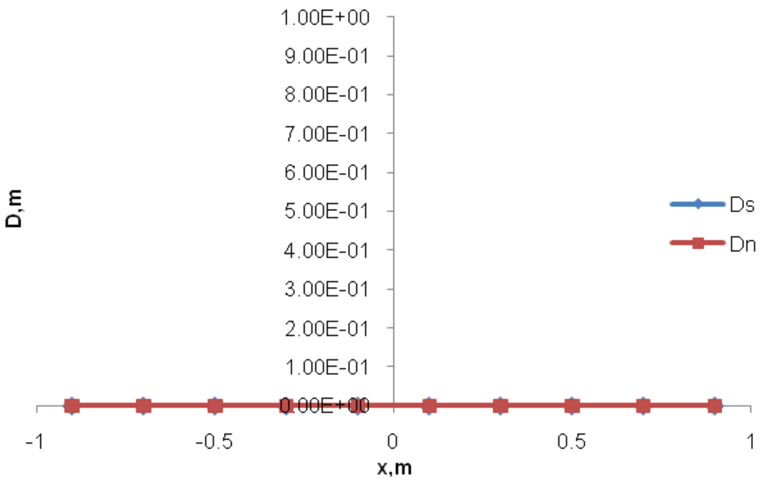

Fig. 4.6 Shear and normal displacement (D_s, D_n) along the joint surface (initial joint deformation not included).

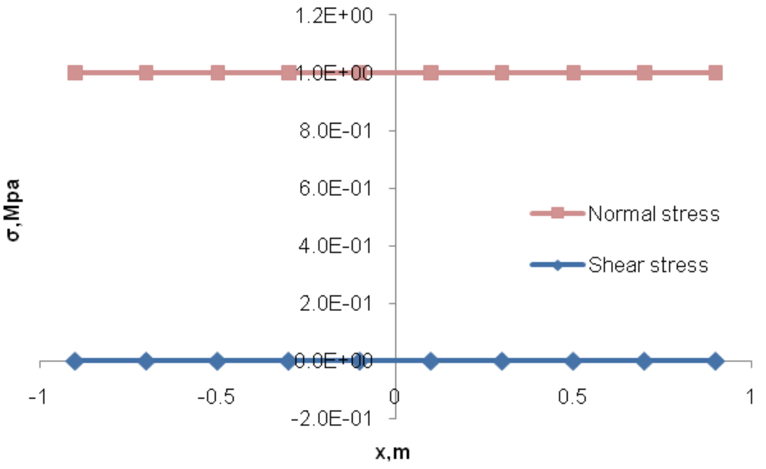

Fig. 4.7 Shear and normal stress along the joint surface (initial joint deformation not included).

In summary, both two models can be used for describing joint behaviors under far-field stresses. But the selection of which model to use depends on the specific considerations for the particular fracturing situations. For fracturing in a naturally-fractured reservoir of long geological history, the second model in which initial joint deformation is excluded seems to have a better representation of the mechanical response (stresses/displacements) of the natural joints as we could expect. And especially when investigating the induced stresses/displacements along the natural joint due to fracturing, the initial joint deformation probably is of less importance to the problem, and can therefore be ignored or regarded as zero.

Therefore more examples were simulated by using the second approach and shown in the following sections, to verify whether this approach can give us reasonable and good approximations for simulating problems involving joint deformation.

4.3.2 A Slanted Single Joint under Biaxial Stresses

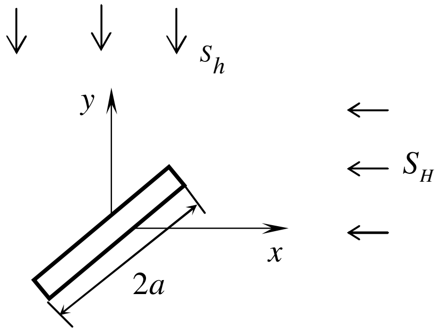

Fig. 4.8 A slanted joint under biaxial stresses.

The mechanical response of a slanted single joint under far-field biaxial stress S_H=4MPa, S_h=3MPa is checked (see **Fig. 4.8**). The slant angle of the joint relative to the direction of SH is 45°, and the normal and shear rigidity of the joint is $K_n = 0.5\text{MPa/m}$ and $K_s = 0.25\text{MPa/m}$. The half length of the joint a=1m.

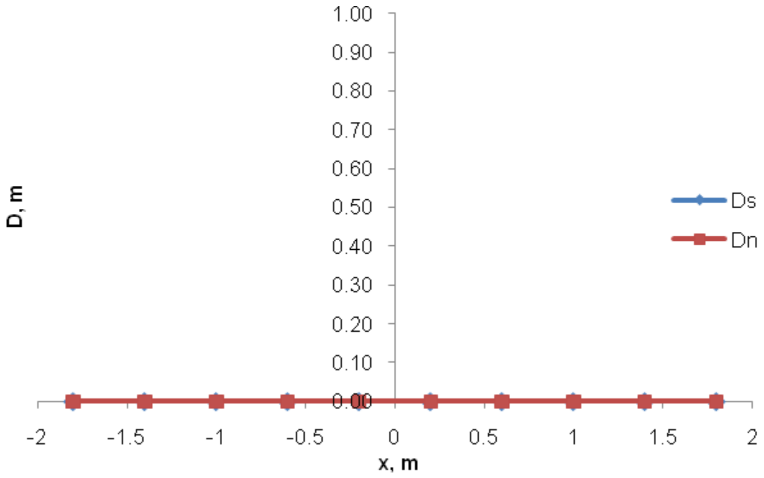

Fig. 4.9 Shear and normal displacement (D_s , D_n) along the joint surface for a slanted joint under biaxial stresses (initial joint deformation not included).

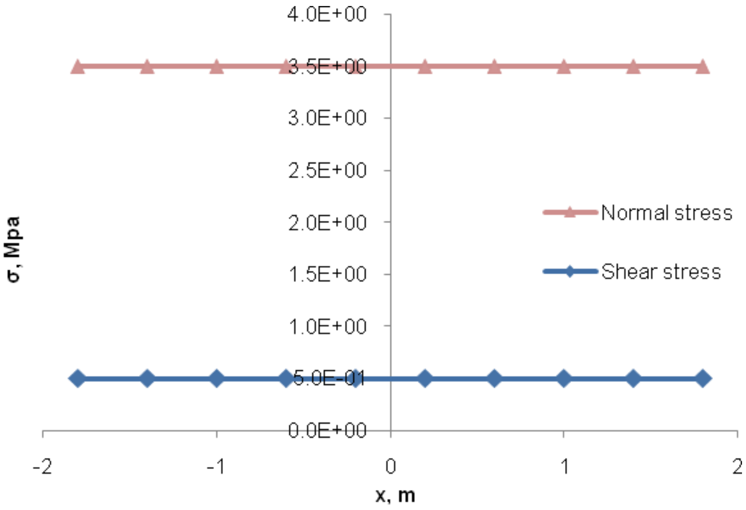

Fig. 4.10 Shear and normal stress along the joint surface for a slanted joint under biaxial stresses (initial joint deformation not included).

As can be seen from **Fig. 4.9** and **Fig. 4.10**, the total shear and normal stresses on the joint are the far-field stresses in the joint direction. The joint is closed and has not slipped under far-field stresses.

4.3.3 Shear of a Single Joint

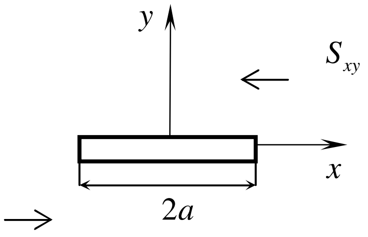

Fig. 4.11 Shear of a single joint.

The mechanical response of a horizontal joint under far-field shear stress is checked in this example (see **Fig. 4.11**). The normal and shear rigidity of the joint is assumed to be $K_n = 0.5\text{MPa/m}$ and $K_s = 0.25\text{MPa/m}$. The frictional angle $\phi = 30°$, far-field stress S_{xy}=2.2MPa, and cohesion $c = 0.22\text{MPa}$.

The stresses and displacements along the joint are shown in **Fig. 4.12** and **Fig. 4.13**. As far-field shear stress has exceeded the yield stress of the joint, which in this case is equal to the cohesion 0.22 MPa, the joint undergoes permanent slippage along the surface, so that the total shear stresses remain at the value of the yield stresses. As can be seen from **Fig. 4.12**, the normal closure and normal stresses are zero in this case of only shear loading (no dilation is considered). Slippage along the joint is symmetric and parabolic.

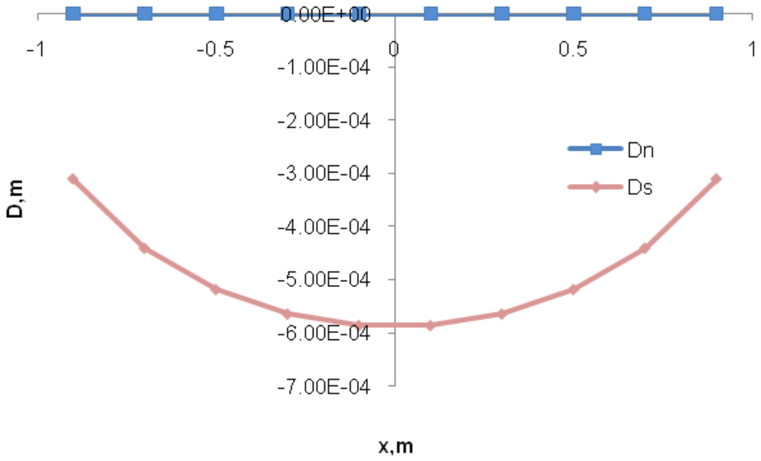

Fig. 4.12 Normal and shear displacement (D_n, D_s) along a joint surface under plastic deformation (initial joint deformation not included).

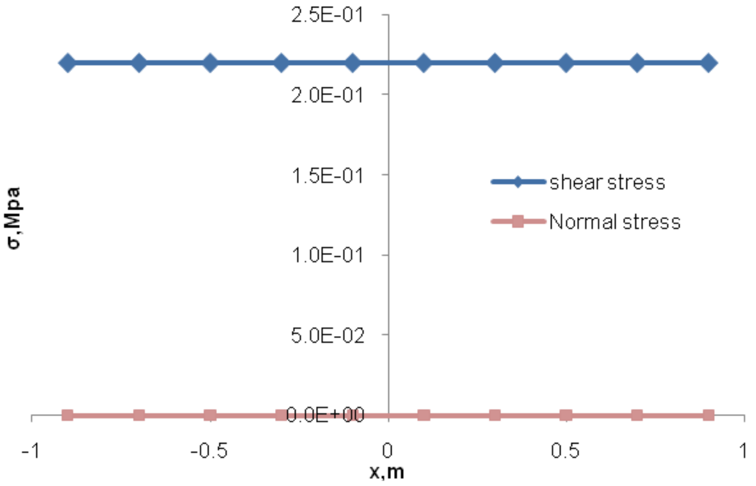

Fig. 4.13 Normal and shear stress along a joint surface under plastic deformation (initial joint deformation not included).

4.3.4 Assessment of Accuracy

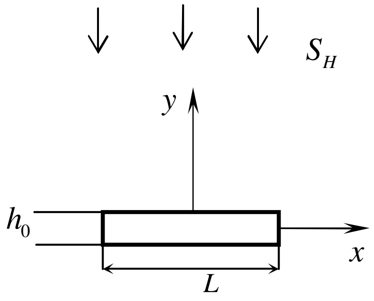

Fig. 4.14 A rectangular opening subjected to far-field compressive stress.

The accuracy of the joint element approach can be checked by using the numerical example in (Crouch 1976) p.137, which essentially examines the stresses and displacement in the vicinity of an excavation in an infinite elastic medium. As shown in **Fig. 4.14**, a single rectangular opening of width *L* and height h_0, in an infinite body is subjected to a uniaxial stress $S_H = p$. The stresses and displacements in the vicinity of the opening and along the *x*-axis are checked. This problem is solved by using the joint element method. I used 10 elements to model the rectangular opening with "**mined" joint elements** (crack elements) and 10 elements along *x*-axis at each side of the rectangular opening as "**unmined" joint elements**. Poisson's ratio of the rock is $v = 0.2$.The rectangular length to height ratio is $L/h_0 = 10$. The ratio of far field stress *p* to the shear modulus *G* was taken as $p/G = 2.4\times10^{-3}$.

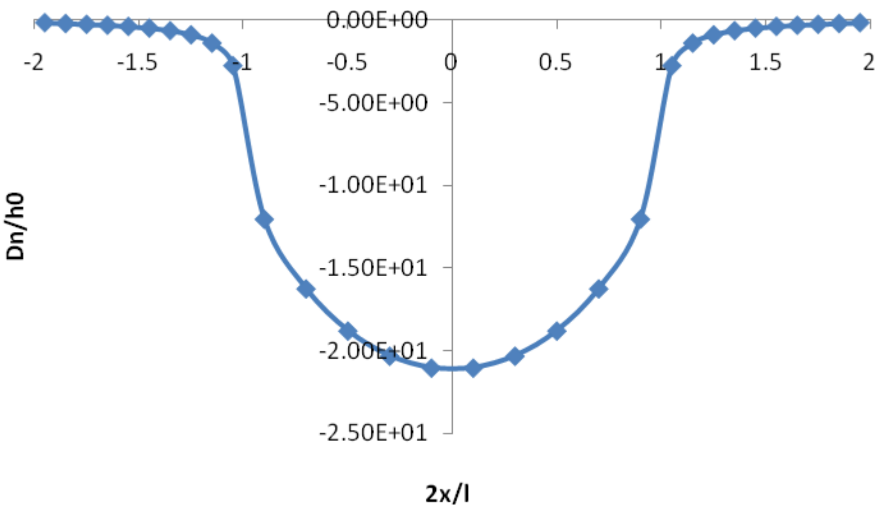

Fig. 4.15 Dimensionless normal displacements at *y*=0 using joint element solution.

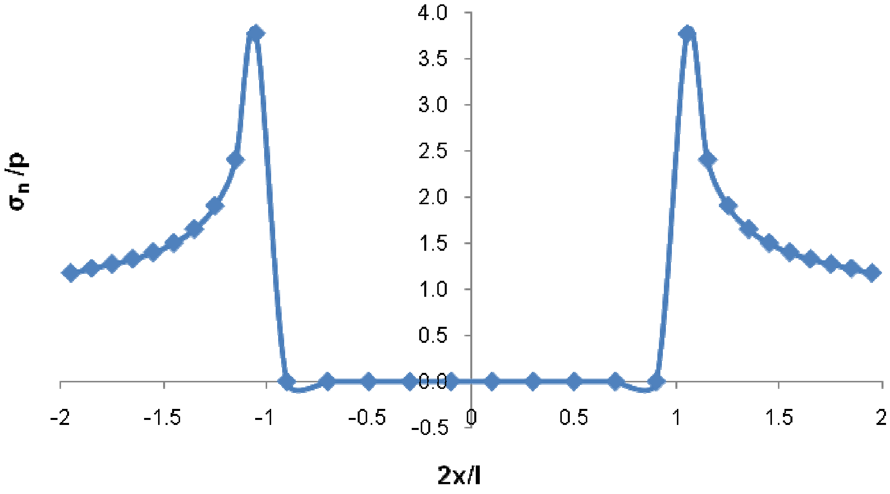

Fig.4.16 Dimensionless normal stresses at *y*=0 obtained using joint element solution.

Dimensionless normal displacement and stresses along *y*=0 are shown in **Fig. 4.15** and **Fig.4.16**. We can see that the two surfaces of the rectangular excavation are closed relative to each other under far-field compressive stress (negative D_n indicating relative closure) and that two surfaces outside the excavation approaches zero displacement. The total normal stress distribution is zero along the excavation and approaches to far-field compressive stress outside the excavation. At locations near the excavation, there is stress localization which is about 3.77 times of the far-field stress. This value matches well with results when only crack element of DD method is used to model the stresses within and outside the excavation along y=0 (Crouch 1976). Therefore, we may come to the conclusion that joint element method can give us fairly accurate results when determining the stress and displacement distribution for problems involving natural fractures and hydraulic fractures (which can be regarded as mined elements with nonzero total normal stresses imposed on the surface).

5 HYDRAULIC FRACTURE AND NATURAL FRACTURE INTERACTION

5.1 Introduction

The objectives of the initial phase of modeling are:

- To study the interaction between a hydraulic fracture (HF) and a natural fracture (NF). Carry out a parametric analysis to explore the effect of model input parameters on the displacements and stresses, and the possible slipping or opening of a pre-existing NF (observe NF and HF mechanical interaction).
- To model the process of HF tip approaching a NF to trace the orientation and extension of the HF.

5.2 Mechanical Responses of a Natural Fracture

5.2.1 Problem Definition

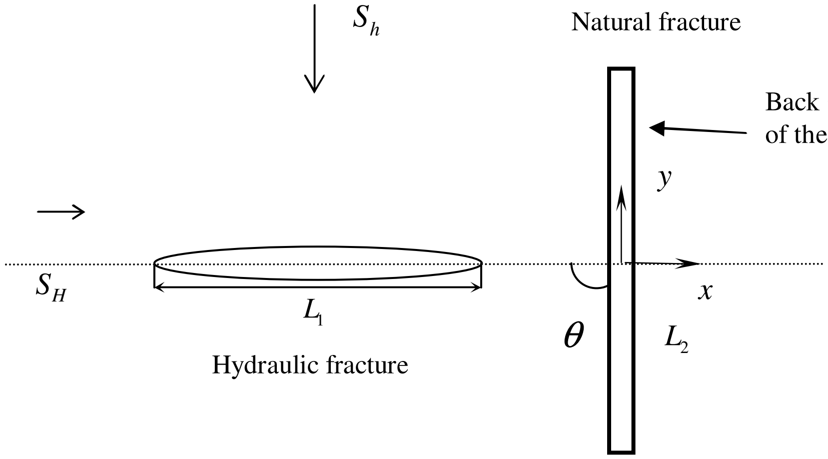

Fig. 5.1 A hydraulic fracture located near a natural fracture.

The first modeling was done assuming a stationary hydraulically induced fracture located near a NF that is oriented θ degrees to the maximum horizontal in-situ stress S_H (see **Fig. 5.1**). The fracture is assumed to be subjected to a constant pressure distribution along its length. The stress and displacement distributions along the NF are checked. The natural fractures/faults are considered to have reached mechanical equilibrium under far-field stresses with geological time (joint model as described in Section **4.1.1.1**). With the introduction of a new HF, the stress field near the NF would experience perturbation, possibly leading to slip/opening. This process along with the most probable location for fracture re-initiation along the NF is investigated below.

For a given rock tensile strength, T_0, the criterion for the tensile crack initiation is (Jaeger et al. 2007):

$$-\sigma_p > T_0 \quad (5.1)$$

where σ_p (see **Fig. 5.2**) is the maximum tensile stress (minimum principal stress, compression positive) defined as:

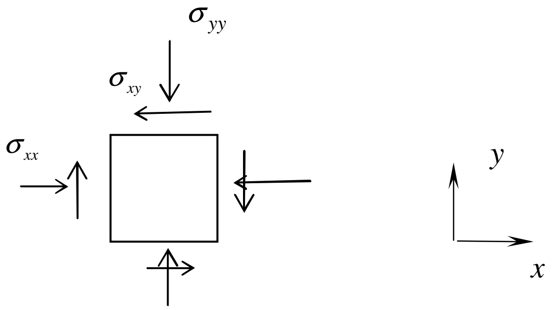

Fig. 5.2 Stress components around a rock element.

$$\sigma_p = 0.5\left(\sigma_{xx} + \sigma_{yy}\right) - \sqrt{\left[0.5\left(\sigma_{xx} - \sigma_{yy}\right)\right]^2 + \sigma_{xy}^{\ 2}} \quad \text{...} (5.2)$$

When the joint is considered ideally smooth and without any secondary flaws along its surface, the zones of tension are the probable locations for new tensile crack re-initiation.

A complete investigation of the interaction between a HF and a NF should include stages of HF tip approaching, fracture coalescence, fluid flow into the NF, and the subsequent initiation of the secondary fracture from the NF. In this thesis, the HF induced stress change and the resultant slippage or tensile opening along the NF are studied for the stage of an approaching HF tip (Section 5.2.2 and 5.2.3), and the stage of fluid flow into the NF (Section 5.2.4).

5.2.2 Parametric Studies

The model inputs are listed in **Table 5.1.** Joints with different magnitude of bonding strengths were investigated in our study. We considered three sets of joint properties: a weak joint (c=0, T_0=0), an infinitely strong joint (c=∞, T_0=∞), and a joint with moderate strength (ϕ=26.6°, c=2.2MPa, T_0=0.2MPa). The distance between the HF tip and NF was modeled to be 0.2m, 0.1m, and 0.05m. The NF (length of 2m) was modeled with 50 constant DD elements with equal length and the HF (length of 2m) was modeled with 20 constant DD elements with equal length. Modeling results are discussed in details as follows.

Table 5.1 Input parameters in Section 5.2.2

Joints	Rock	HF
Geometry: • Orientation $\theta = 90°$ • Length $L_2 = 2\text{m}$	In-situ Stresses: • $S_H = -2.1\text{MPa}$ • $S_h = -1.9\text{MPa}$	Geometry • Length $L_1 = 2m$ • Distance with NF d_0
Mechanical Properties: • Friction angle: ϕ • Cohesion: c • Tensile strength: T_0 • Normal stiffness $K_n = 0.5\times10^6\text{MPa/m}$ • Shear stiffness $K_s = 0.25\times10^6\text{MPa/m}$	Mechanical Properties: • Young's modulus $E = 1.4\times10^4\text{MPa}$ • Poisson's ratio $v = 0.1$	Fluid Properties: • Fluid pressure $p = 3.9\text{MPa}$

The weak joint has zero cohesion and tensile strength, so it cannot sustain any shear and tensile forces and is always ready to slip or open. In **Fig. 5.3**, the stress distribution along a weak joint, when d_0=0.1m and θ=90° is plotted. The shear stress in this case is zero, and as the yield stress is set to zero in this case, the fault is in a plastic yield condition or "permanent slip" mode. The normal stress and shear stress are zero near the center of the joint, which is an indication of joint opening (normal to the joint surface) at this segment. The maximum tensile stress becomes negative near the center of the opposite side of the joint, and has two peak values located at two locations with symmetry to the x axis. As the tensile limit of the joint is zero and has been exceeded in this case, these two locations could become most probable location for new tensile crack onset before the coalescence of the HF with the NF.

However, the induced tensile crack may not have a sufficient capability to grow further without fluid infiltration. Once the HF coalesces with the NF, and fluid penetrates into the NF, the stress distribution along the joint and the zones of stress localization for new crack re-initiation may change. Therefore, a complete study of HF interaction with NF involving all the subsequent stages is needed for us to have a complete picture of this problem.

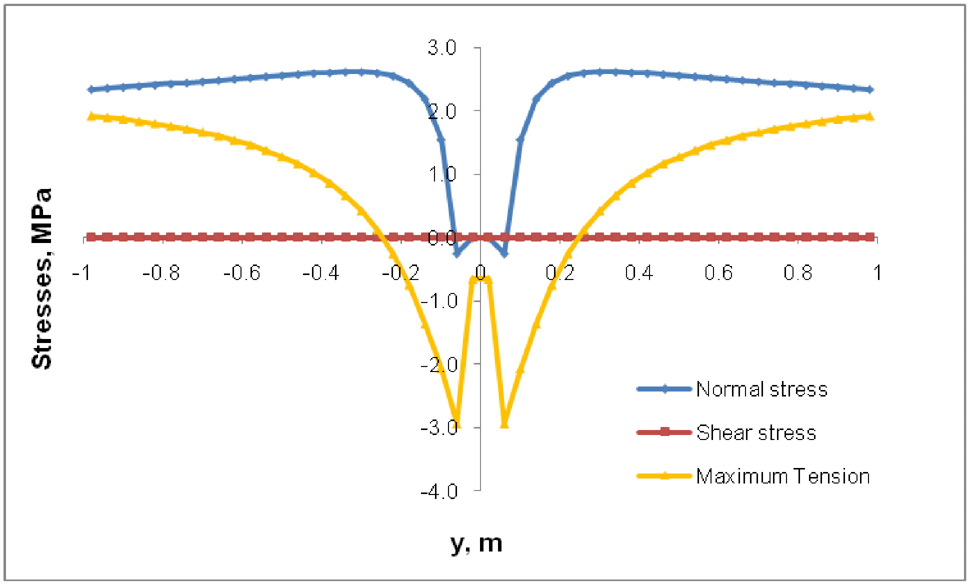

Fig. 5.3 Stress distribution along a weak joint (at *x*=0, d_0=0.1m, θ=90°).

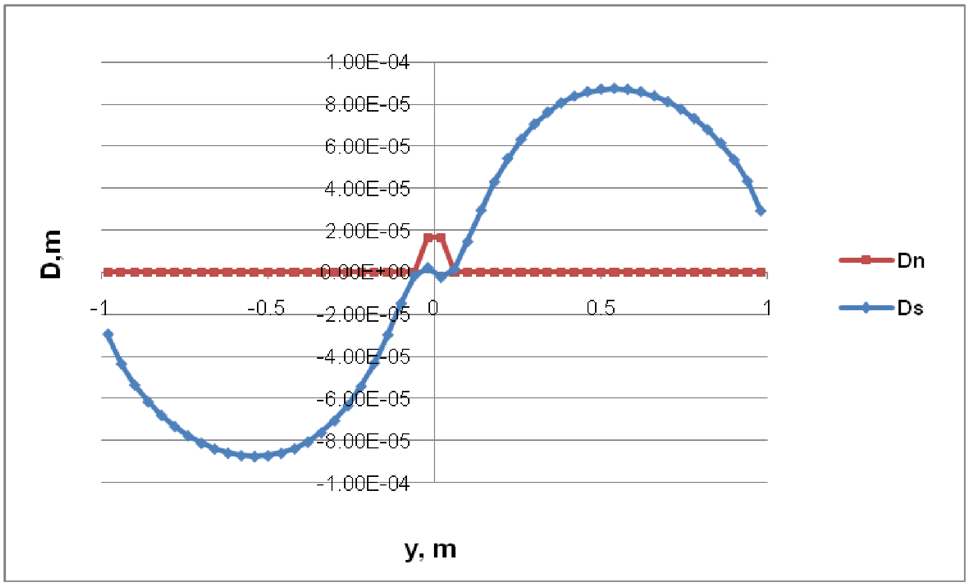

Fig. 5.4 Normal and shear displacement (D_n, D_s) along a weak joint (at x=0, d_0=0.1m, θ=90°).

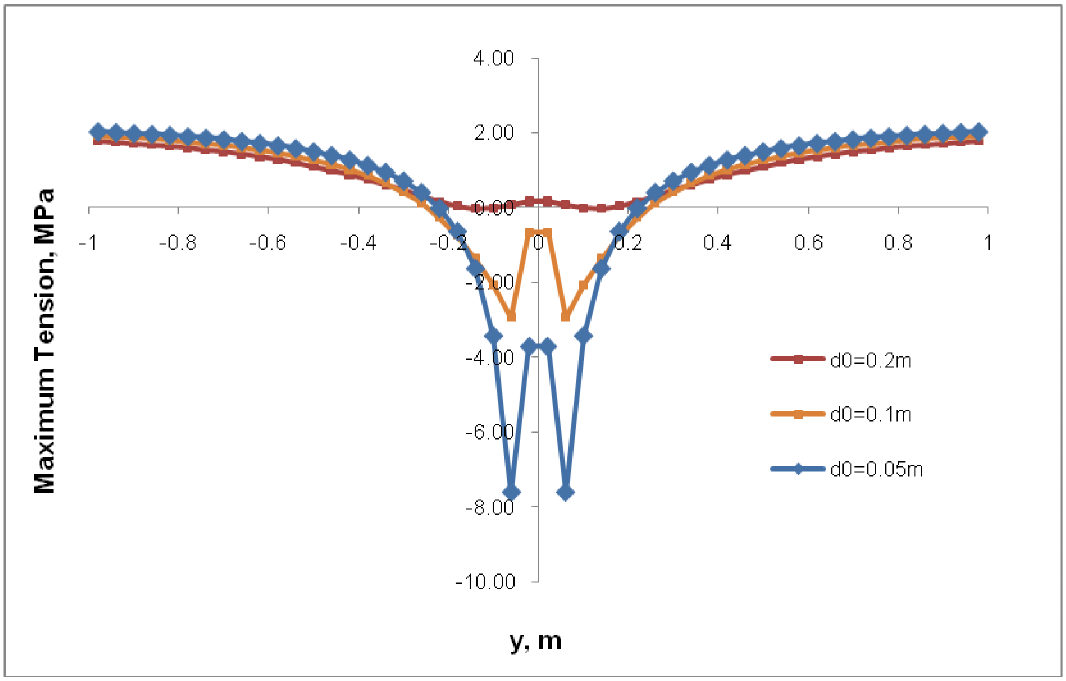

Fig. 5.5 Maximum tensile stress along a weak joint (x=0) at different tip distances (d_0) (θ=90°).

The shear slip and normal displacement is shown in **Fig. 5.4**. The normal displacement is positive, which indicates that HF can induce normal opening near the HF tip region along the joint. Curves of maximum tensile stress generated along the back side of the joint at different distances from the HF tip and NF are plotted in **Fig. 5.5**. With the approaching of HF tip to the NF, the influence of fracture tip is stronger and the tension force gets bigger. The two peak locations move closer to the center of the NF, with the decreasing of the distance between HF tip and NF.

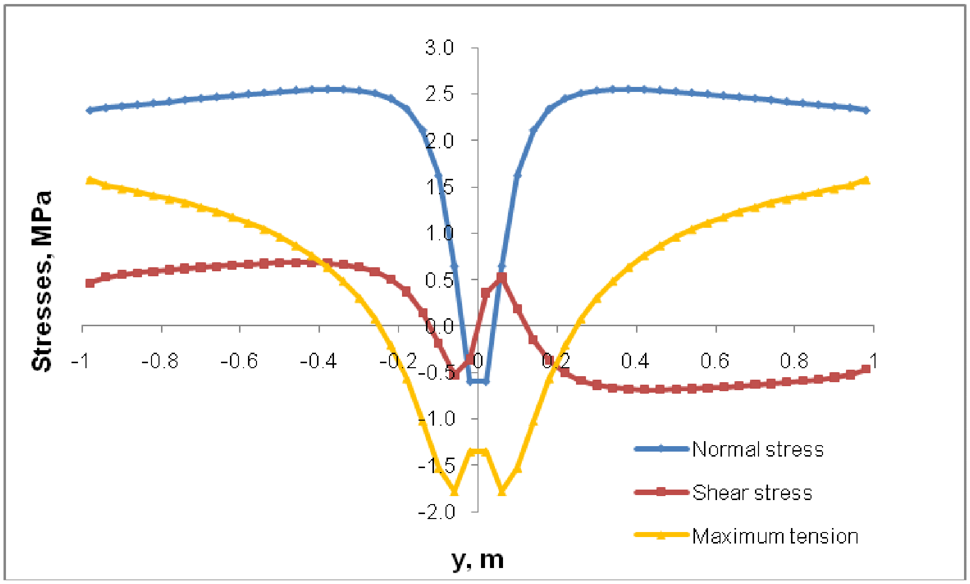

Fig. 5.6 Stress distribution along a strong joint (at x=0, d_0=0.1m, θ=90°).

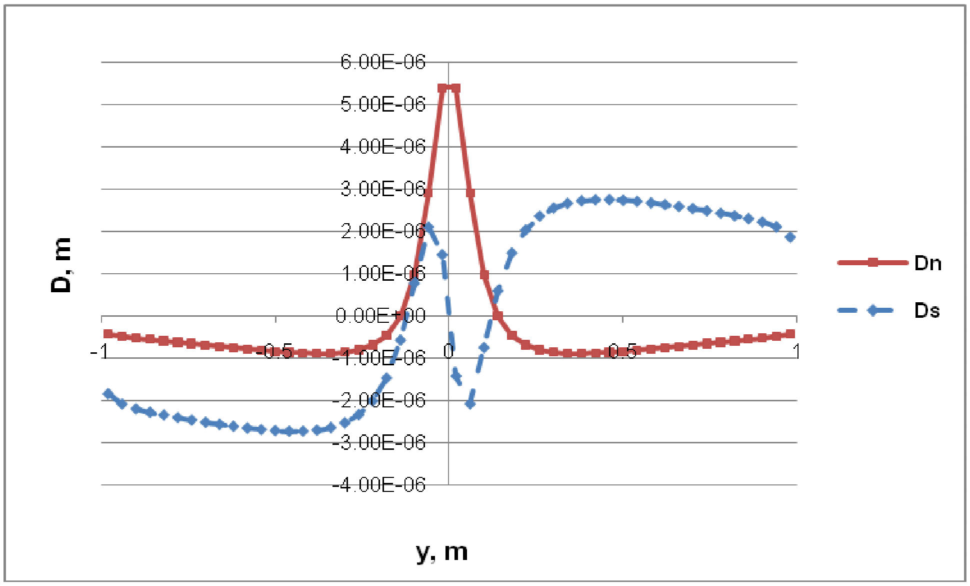

Fig. 5.7 Normal and shear displacement (D_n, D_s) along a strong joint (at x=0, d_0=0.1m, θ=90°).

Stresses and displacements along a strong joint ($c=\infty$, $T_0=\infty$) are calculated and plotted in **Fig. 5.6** and **Fig. 5.7**. A joint with infinite strength is bonded so strongly that tensile failure (joint crack open) and shear failure (joint permanent slip) will never occur on it. From **Fig. 5.6** we can see that everywhere along the joint the shear and normal stress are nonzero, and that yield stress has not been reached (infinite in this case), so everywhere along the joint is in the "stick" contact mode. For a very strong joint, the HF cannot induce enough stresses that can lead to the joint "opening" and "permanent slip". The maximum normal opening at the center of the joint for a strong joint is about 5.39×10^{-6} m as shown in **Fig. 5.7**, which is much smaller than that for a weak joint (about 1.65×10^{-5}m). As could be expected, the induced displacements are much less for a joint with stronger strength.

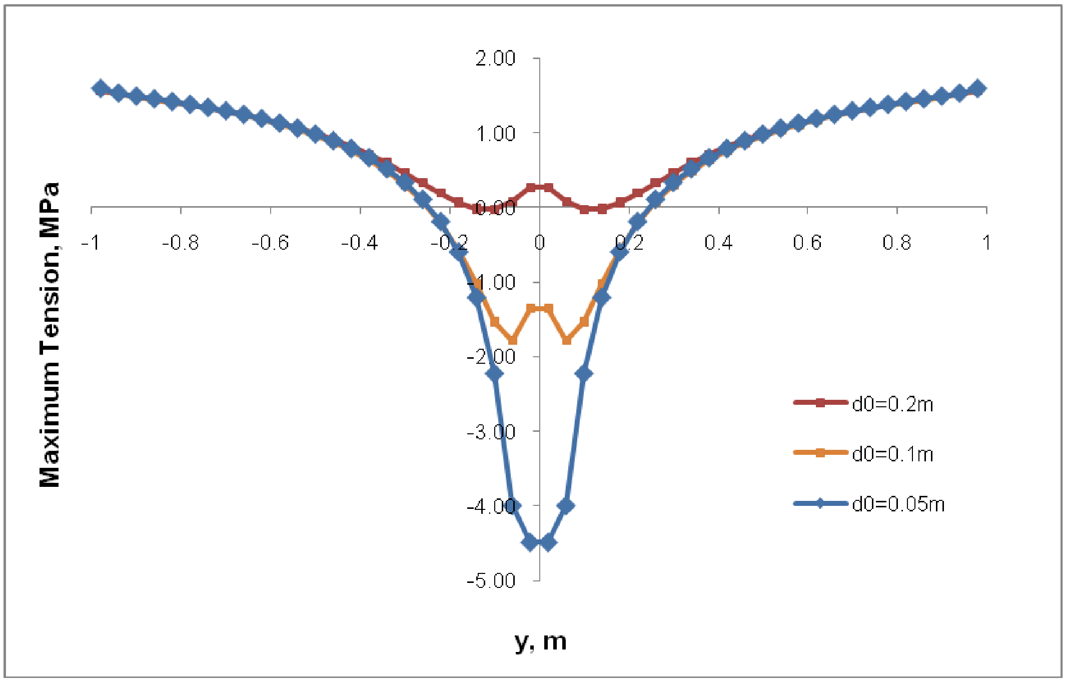

Fig. 5.8 Maximum tensile stress along a strong joint (*x*=0) at different tip distances (*d_0*) (*θ*=90°).

From **Fig. 5.8** we can see that the maximum tensile stress generated at the back side of the strong joint (see **Fig. 5.1**) also increase with the decrease of the distance between HF tip and NF. The joint has an infinite tensile strength in this case, and the induced tension is of finite value, so a very strong joint inhibits crossing of the HF. In comparison with a weak joint, the magnitude of the peak value gets smaller and the location of the two peak values gets closer for a strong joint.

In most practical cases, a natural joint is of moderate strength between these two above limiting cases. Therefore a joint with intermediate strength values (α=26.6°, c=2.2MPa, T_0=0.2MPa) is also simulated to check its mechanical responses. Stresses and displacements along the joint are plotted in **Fig. 5.9** and **Fig. 5.10**, respectively. From

Fig. 5.9, it can be seen that one small segment at the center of joint has zero shear and normal stress corresponding to an "open" contact mode (when the normal stress exceeds the tensile limit of the joint and the joint surfaces open like a crack). When d_0=0.1m, the peak values of maximum tensile stress at the opposite side of the NF is about 2 MPa which exceeds the tensile limit of the joint (0.2 MPa) in this case. So, the onset of new tensile cracks can begin there before the HF coalesces with the NF. Again **Fig. 5.11** shows that the maximum tensile stress increases with the approach of HF tip, and the peak tension becomes more localized near the tip region when the tip is closer to the NF.

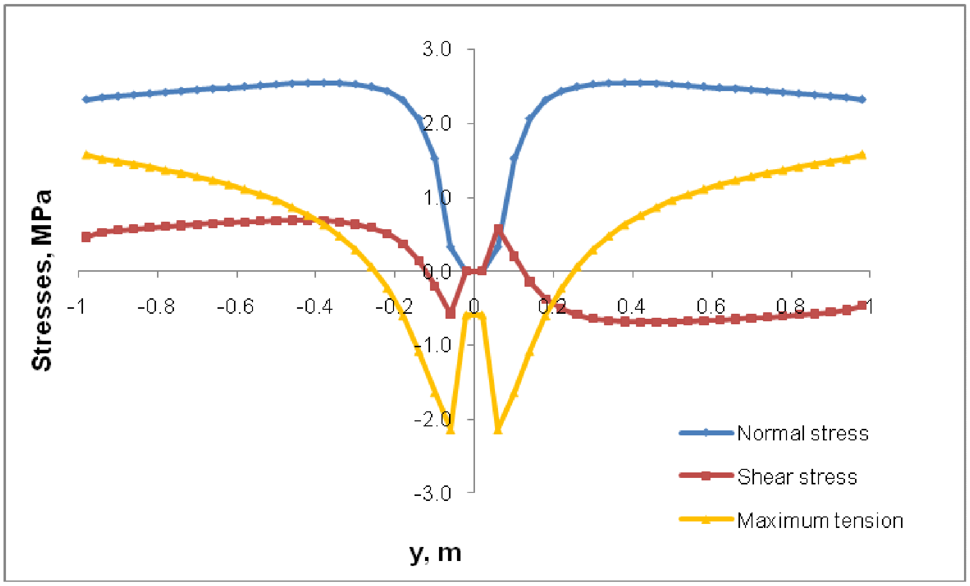

Fig. 5.9 Stress distribution along a moderate joint (at x=0, d_0=0.1m, θ=90°).

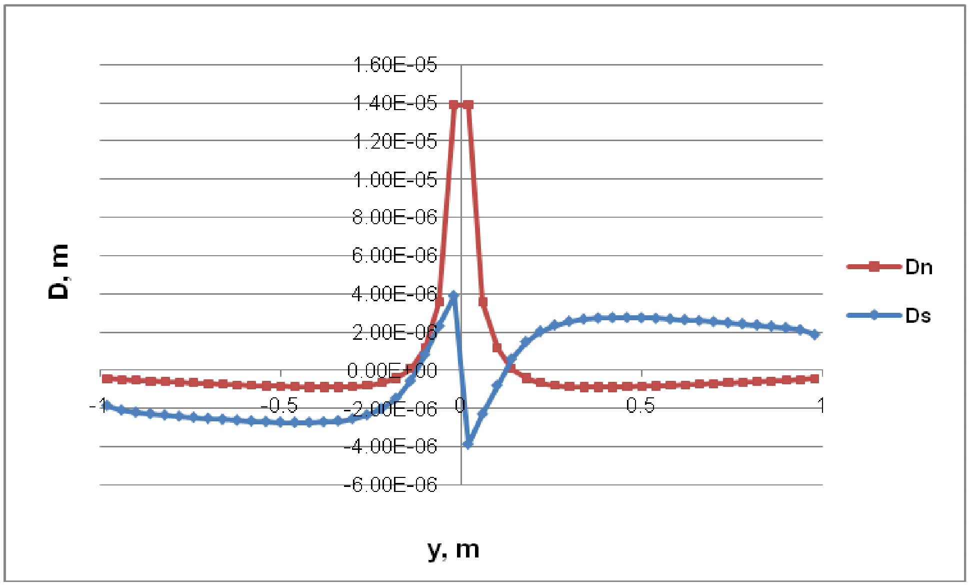

Fig. 5.10 Normal and shear displacement (D_n, D_s) along a moderate joint (at x=0, d_0=0.1m, θ=90°).

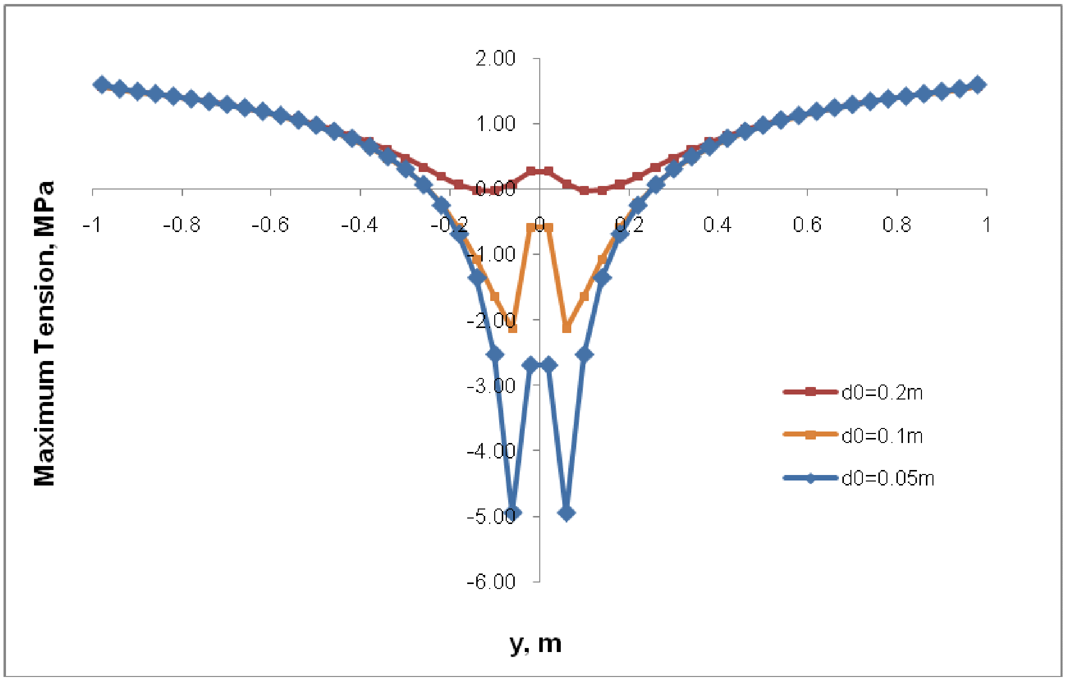

Fig. 5.11 Maximum tensile stress along a moderate joint (x=0) at different tip distances (d_0) (θ=90°).

By comparing **Fig. 5.5**, **Fig. 5.8** and **Fig. 5.11**, it can be concluded that: 1) Before HF reaches the NF, fracture re-initiation is more encouraged when the joint has weaker interfaces, because the induced tension is more likely to exceed the tension limit of the rock; a stronger joint tends to inhibit fracture re-initiation as the induced tension is usually smaller and the tensile strength; 2) In terms of re-initiation location, a fracture step-over (offset) is more likely to happen for HF interacting with a weak joint because the stress localization on the joint tends to be mitigated by NF sliding; direct crossing of the HF is more likely to occur when interacting with a stronger joint.

5.2.3 Discussion

The mechanical response along a joint was compared with a previous study (Chuprakov et al. 2010) of a stationary HF located near a NF. The geometry of the problem is shown in **Fig. 5.1**. The main parameters used are listed in **Table 5.2**.

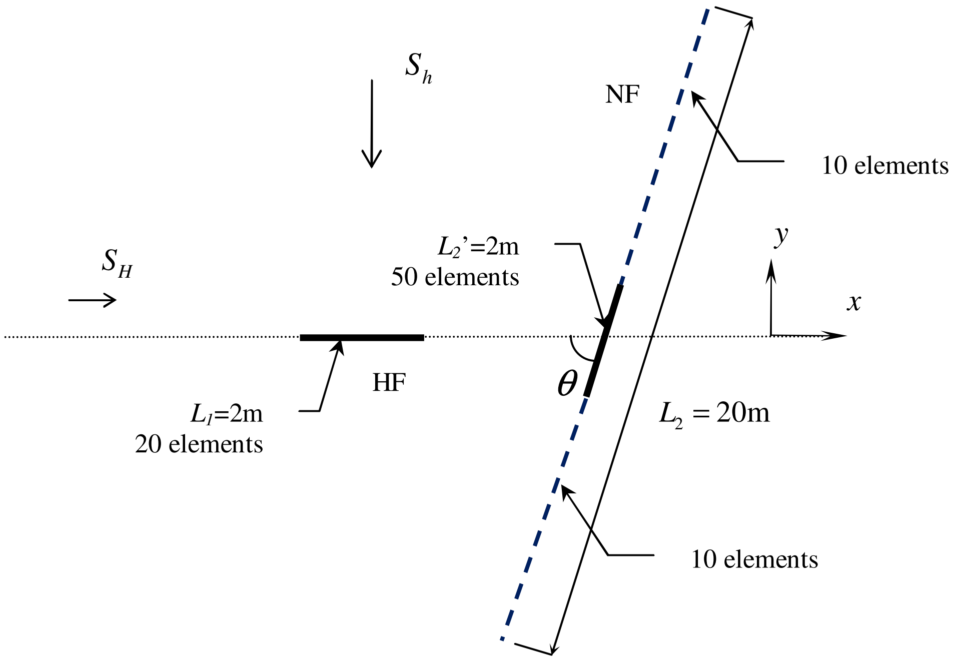

Fig. 5.12 Sketch of mesh arrangement for the NF and HF. Dashed part of the NF is negligible in the interaction between HF and NF, and therefore can be omitted in the modeling.

Seventy elements were used in the simulation of the NF of 20m length, with 50 elements distributed over the central region of the NF (with a length of 2m); 20 equal length elements were used along the HF of length of 2m. Similar results were obtained for modeling only the center of the NF with a length of 2m using 50 equal length elements. The modeling results indicate that the interaction between HF and NF is negligible in regions outside the central portions of the NF (dashed part of NF as sketched in **Fig. 5.12**) and that excluding these regions in the model will not affect the model outputs.

The shear and normal displacement along the joint $D_{s,n}$ are normalized as following: $d_{s,n} = \frac{D_{s,n}}{L_1}\frac{G}{(1-v)\sigma_m}$, in which $\sigma_m = \frac{1}{2}(\sigma_1 + \sigma_3)$ is the mean far-field stress. The shear and normal stresses $S_{t,n}$ along the joint are normalized by the mean far-field stress: $s_{t,n} = \frac{S_{t,n}}{\sigma_m}$.

Table 5.2 Input parameters in Section 5.2.3

Joints	Rock	HF
Geometry: • Orientation $\theta = 40°$ • Length $L_2 = 20\text{m}$	In-situ Stresses: • $S_H = -2.1\text{MPa}$ • $S_h = -1.9\text{MPa}$	Geometry • Length $L_1 = 2\text{m}$ • Distance with NF $d = 0.1\text{m}$
Mechanical Properties: • Friction angle: $\phi = 26.6°$ • Cohesion $c = 2.2\text{MPa}$ • Tensile strength: $T_0 = 0.2\text{MPa}$ • Normal stiffness $K_n = 0.5\times10^6\,\text{MPa/m}$ • Shear stiffness $K_s = 0.25\times10^6\,\text{MPa/m}$	Mechanical Properties: • Young's modulus $E = 1.4\times10^4\,\text{MPa}$ • Poisson's ratio $v = 0.1$	Fluid Properties: • Fluid pressure $p = 3.9\text{MPa}$

From **Fig. 5.13**, it can be seen that along most part of the joint the shear slip and normal displacement are nearly zero, and that the HF tip would induce a relative joint opening (positive d_n) and shear slip (d_s) near the center of the NF. In **Fig. 5.14**, the normalized stresses along the joint are plotted. At the lower side (y<0) of the NF, there is an opened segment where shear stress and normal stress come to zero. The maximum tensile stress generated along the opposite side of the joint reaches two peak values near the two ends of the opening section. Similar results can be found in Chuprakov et al. (2010). The magnitude and location of the peak of maximum tensile stress are actually very sensitive to various model input parameters. The difference might result from: 1) In Chuprakov et al., the normal opening for the "closed" part sof NF was set to zero. But in this thesis, the relative normal closure/opening could occur along the entire length of the joint (it is assumed that the NF has an initial aperture that is much larger than the induced relative normal displacements (either positive or negative) so that two surfaces of NF will not come into contact or overlap)). Therefore, in our results, the boundary between the HF influenced zone (with nonzero shear and normal displacments) and the closed part of the NF are less disdinct; 2) The shear and normal rigidity of the joint were not considered/mentioned in Chuprakov et al. while a relatively large rigidity is assumed in this thesis to prevent significant normal/shear displacement outside the HF influenced zone; 3) The tensile strength of the rock was not mentioned in Chuprakov et al. The strength of the rock will afftect the jog position (tension peak may occur either at the right or left side of NF (Chuprakov et al. 2010)).

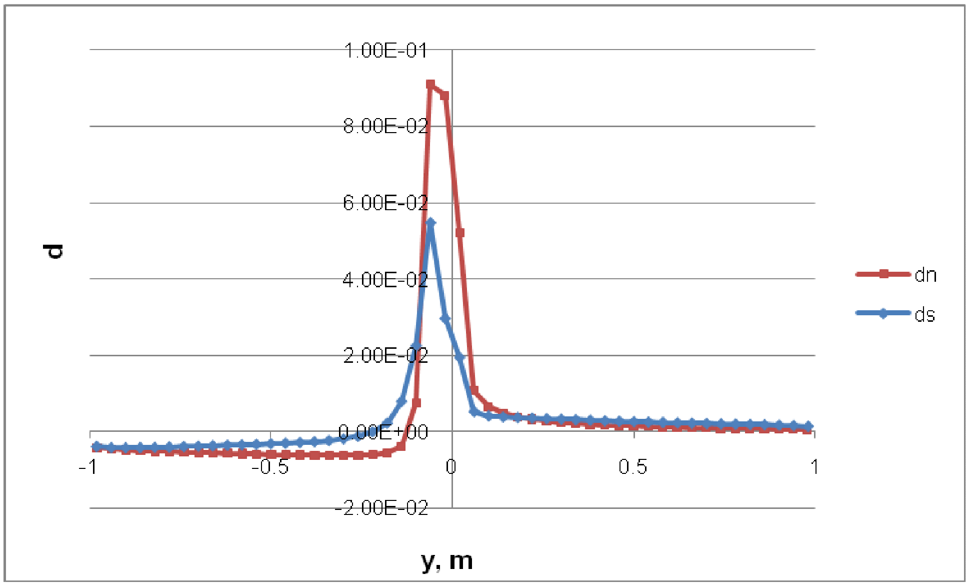

Fig. 5.13 Normalized normal/shear displacements (d_n, d_s) along the NF (x=0).

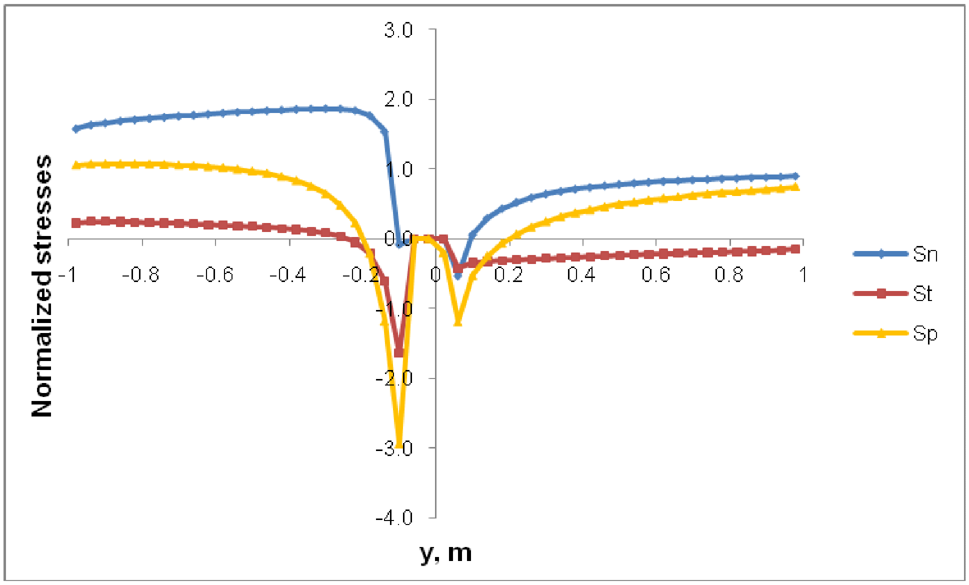

Fig. 5.14 Normalized values of normal stress (s_n), shear stress (s_t), and maximum tensile stress (s_p) along NF (x=0).

5.2.4 Interaction at the Stage when Fluid Flows into the Natural Fracture

The mechanical response of a NF once the fluid is flowing from the HF into the NF is considered in this section. It is assumed that the HF has coalesced with NF, and that the injected fluid propagates along the (y>0) part of the NF (for an acute orientation angle θ) (**Fig. 5.1**). Fluid flow is assumed steady and a constant pressure distribution has been established along both the HF and the infiltrated part of the NF. The input parameters are listed in **Table 5.3**.

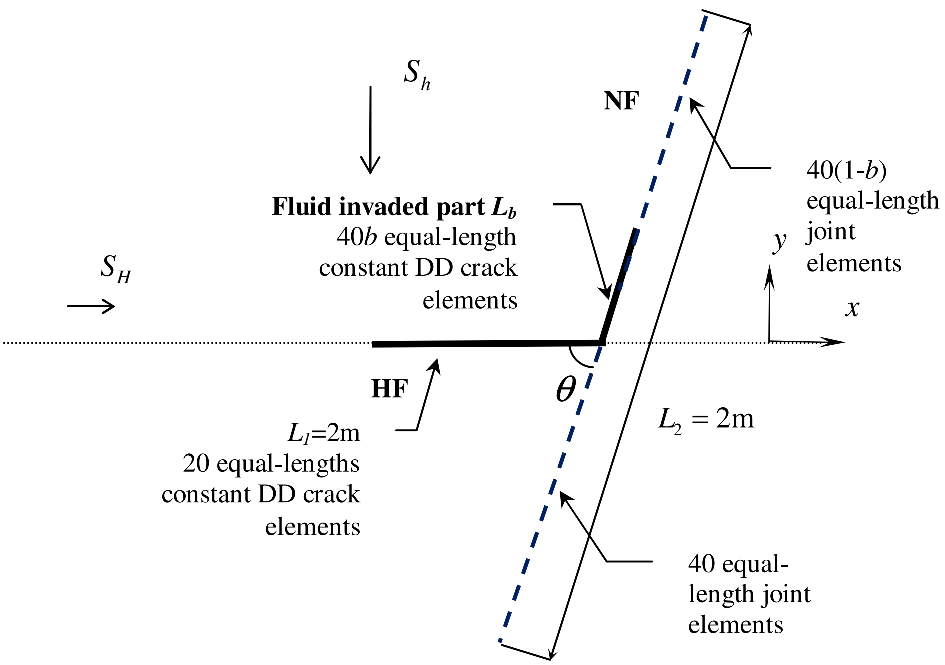

Fig. 5.15 Sketch of mesh arrangement for a HF and NF partly filled with fluid.

In **Fig. 5.15**, mesh arrangement along the HF and NF with partial fluid penetration is plotted. Twenty equal-length constant DD crack elements were implemented along the HF. Eighty equal-length elements were arranged along the NF, with constant DD crack elements along the fluid infiltration part, and joint elements along the unpressurized part of the NF.

Table 5.3 Input parameters in Section 5.2.4

Joints	Rock	HF
Geometry: • Orientation $\theta = 40°$ • Length $L_2 = 2\text{m}$ • Invaded length b	In-situ Stresses: • $S_H = -2.0\text{MPa}$ • $S_h = -2.0\text{MPa}$	Geometry • Length $L_1 = 2\text{m}$ • Distance with NF $d = 0.0\text{m}$
Mechanical Properties: • Friction angle: $\phi = 26.6°$ • Cohesion $c = 0.1\text{MPa}$ • Tensile strength: $T_0 = 0.2\text{MPa}$ • Normal stiffness $K_n = 0.5 \times 10^6\,\text{MPa/m}$ • Shear stiffness $K_s = 0.25 \times 10^6\,\text{MPa/m}$	Mechanical Properties: • Young's modulus $E = 1.4 \times 10^4\,\text{MPa}$ • Poisson's ratio $v = 0.1$	Fluid Properties: • Fluid pressure p

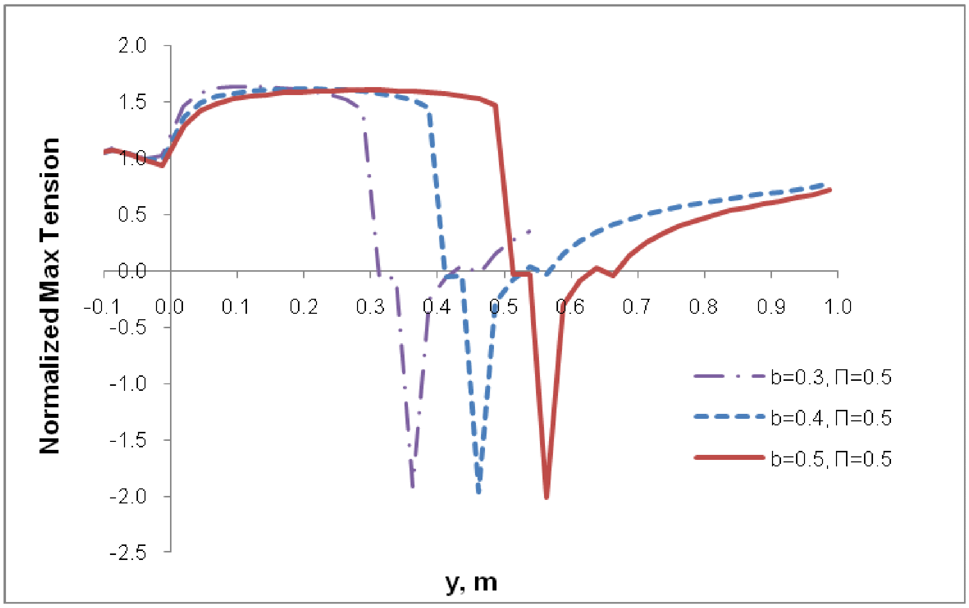

Fig. 5.16 Normalized maximum tensile stress along NF (x=0) at different fluid invaded lengths of NF (b) (p=3.0MPa).

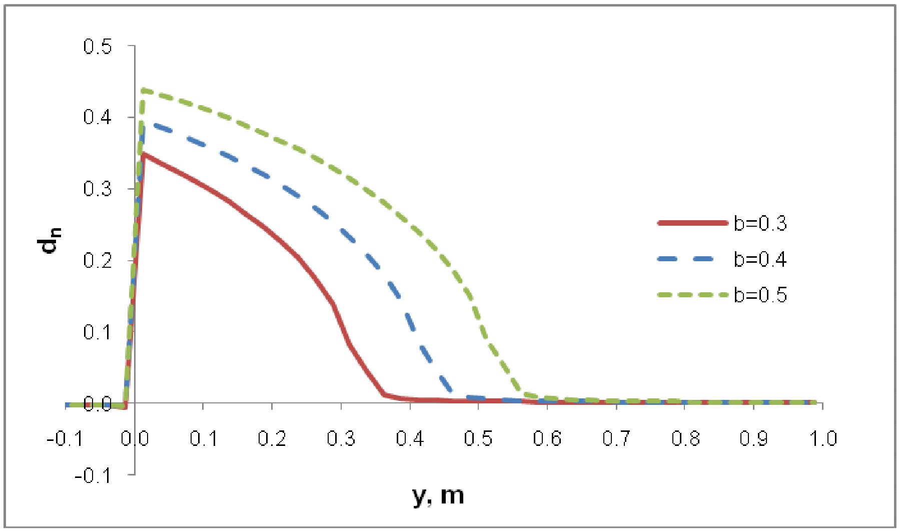

Fig. 5.17 Normalized normal displacement (d_n) along NF (x=0) at different fluid infiltrated lengths of NF (b) (p=3.0MPa).

First consider the normalized maximum tensile stress that develops along the NF when the fluid-infiltrated length of NF is increased without changing the fluid pressure. As can be seen from **Fig. 5.16**, a tensile peak is generated along the NF ahead of the fluid front (the maximum tensile stress, S_p, along the joint is normalized by the mean far-field stress, $s_p = \frac{S_p}{\sigma_m}$ in which $\sigma_m = \frac{1}{2}(\sigma_1 + \sigma_3)$ is the mean far-field stress. The fluid infiltrated length of the NF L_b is normalized with half length of the HF, $b = \frac{L_b}{0.5L_1}$). The value of the tensile peak is about 4MPa, and does not change with increased fluid infiltrated length. The location of the tension peak moves along the NF with the increasing of the fluid infiltrated length.

As can be seen from **Fig. 5.17**, the fluid pressure, which is set to be higher than the far-field compressive stress (by 1MPa), creates an open zone (d_n>0) along the NF. The length of the open zone (d_n>0) is always longer than the length of the fluid infiltrated zone which means there is a fluid lag between the fluid front and end of the open zone. In addition, the tension peak is located at the end of the NF open zone. Therefore, the tension peak is always ahead of the fluid front, and moves with the open zone while fluid infiltrates along the NF. These results are consistent with those of Cooke and Underwood (2001) and Chuprakov et al. 2010. The location of the maximum tensile stress peak is a probable location for further fracture re-initiation.

As another example, let's fix the pressurized length of the HF while increasing the fluid pressure along the HF and NF. The normalized maximum tensile stress along the NF is plotted in **Fig. 5.18**. It can be seen that the value of the tension peak increases and its location moves further to the right part of the NF (y>0) with increasing fluid pressure.

Based on these two example simulations, it can be concluded that the location of peak tension is dependent on both the fluid pressure and fluid infiltrated length of the NF, and its value depends mostly on the fluid pressure.

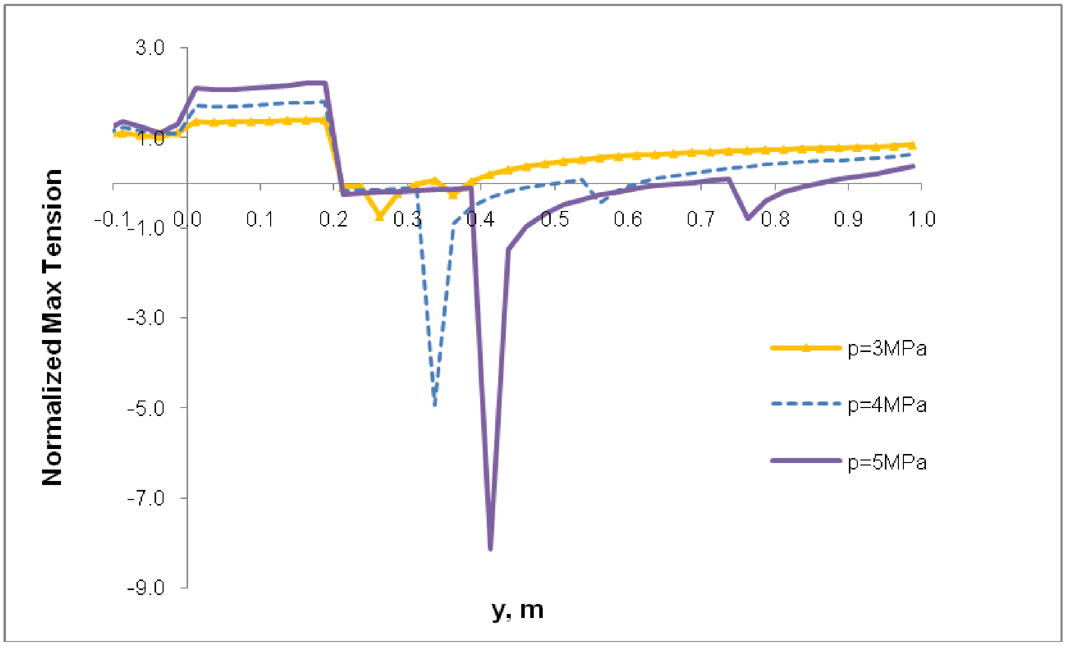

Fig. 5.18 Normalized maximum tensile stress along NF (x=0) at different fluid pressures (p) (b=0.2).

5.2.5 Poroelastic Effect on Mechanical Responses of Natural Fracture

In all previous numerical examples, the rock formation was considered to be elastic and impermeable. In this section, the pore pressure effect on the mechanical responses of the NF is investigated. Again, a uniform pressure distribution along the HF is assumed.

First consider the stage prior to HF coalescing with NF by assuming a stationary HF located near the NF, and monitor the mechanical response of the NF with fluid diffusion from fracture surface into the rock with time. Input parameters are listed in **Table 5.4.** The reservoir rock parameters are used from Westerly Granite as reported in the paper of McTigue (1986).

Table 5.4 Input parameters for granite in Section 5.2.5 (McTigue 1986) (I)

Joints	Rock	HF
Geometry: - Orientation $\theta = 90°$ - Length $L_2 = 2\text{m}$	In-situ Stresses: - $S_H = -2.1\text{MPa}$ - $S_h = -1.9\text{MPa}$	Geometry - Length $L_1 = 2m$ - Distance with NF $d_0 = 0.1$
Mechanical Properties: - Friction angle: $\phi = 26.6°$ - Cohesion: $c = 2.2\text{MPa}$ - Tensile strength: $T_0 = 0.2\text{MPa}$ - Normal stiffness $K_n = 0.5\times10^6\,\text{MPa/m}$ - Shear stiffness $K_s = 0.25\times10^6\,\text{MPa/m}$	Mechanical Properties: - Young's modulus $E = 1.4\times10^4\,\text{MPa}$ - Poisson's ratio $v = 0.1$ - Bulk modulus $K = 4.5\times10^4\,\text{MPa}$ - Porosity $n = 0.01$ - Dynamic permeability $k = 4.053\times10^{-7}\,\text{darcy}$ - Fluid diffusivity $c^f = 6.16\times10^{-5}\,\text{m}^2/\text{s}$	Fluid Properties: - Fluid pressure $p = 3.9\text{MPa}$ - Fluid bulk modulus $K_f = 2.5\times10^3\,\text{MPa}$

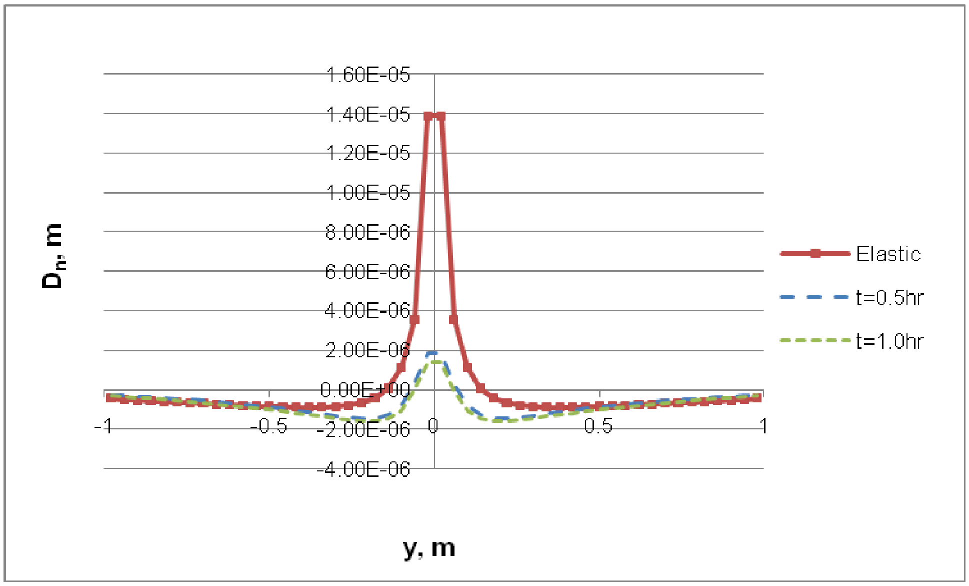

Fig. 5.19 Distribution of normal displacement (D_n) along a moderate joint (x=0) at different time (t) considering poroelastic effects.

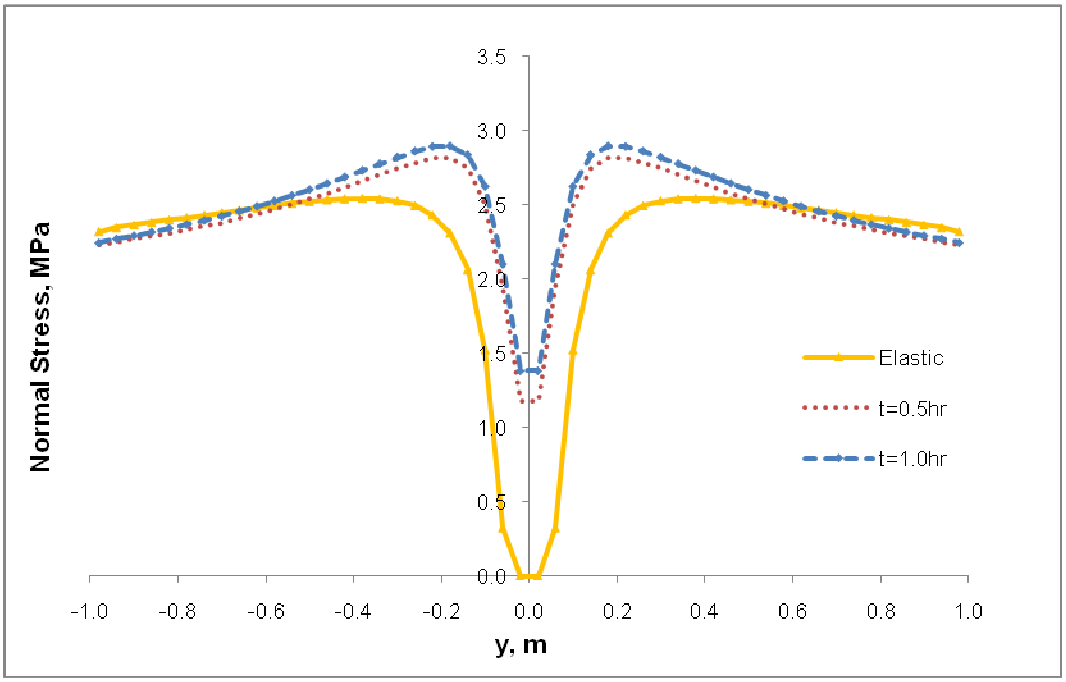

Fig. 5.20 Distribution of normal stress along a moderate joint (x=0) at different time (t) considering poroelastic effects.

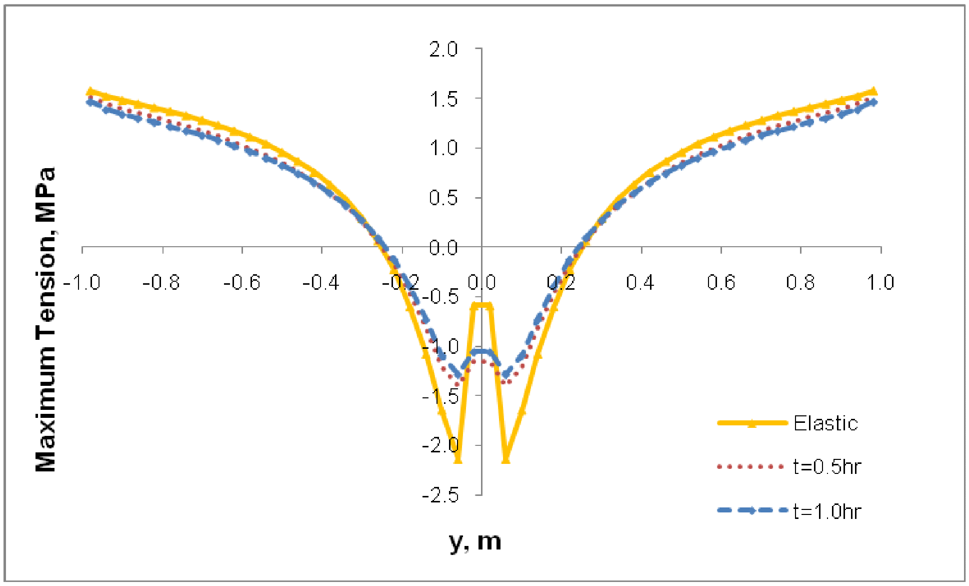

Fig. 5.21 Distribution of maximum tensile stress along a moderate joint (*x*=0) at different time (*t*) considering poroelastic effects.

Distribution of normal displacement (D_n), normal stress, and maximum tensile stress generated along the joint at different times are plotted in **Fig. 5.19**, **Fig. 5.20** and **Fig. 5.21**, respectively. It can be observed that with fluid diffusion from the fracture into the rock matrix, the HF tip induced normal displacement, normal stress and maximum tensile stress all decrease with time near the center of the NF, and slightly increase outside the center region of the NF. The normal stress at the center of the NF changes from zero to positive value (becomes compressive). The value of HF tip induced maximum tensile stress also decreases with time. Therefore, the possibility for fracture re-imitation is less if pore pressure diffusion is included.

Near the center of the NF, HF tip induced stresses are weakened because HF aperture decreases with fluid diffusion into the rock, which is much more influential than the effective stress decrease with pore pressure increase. However, further away from the HF tip influenced region, outside the center of the NF, the factor of effective stresses decrease gradually dominates so the maximum tensile stress and normal stress become more tensile.

The poroelastic effect on the mechanical response of the NF during the stage when fracturing fluid penetrates part of the NF are then considered by assuming a sequence of fluid with moving fluid front. The input parameters are listed in **Table 5.5**. The model ideally should couple the fluid infiltrated length, pressure distribution and time together, but the simulation is simplified by assuming a fluid infiltrated length at each time, and by assuming a uniform pressure distribution along the HF and NF.

Table 5.5 Input parameters for granite in Section 5.2.5 (McTigue 1986) (II)

Joints	Rock	HF
Geometry: • Orientation $\theta = 40°$ • Length $L_2 = 2\text{m}$ • Invaded length b	In-situ Stresses: • $S_H = -2.0\text{MPa}$ • $S_h = -2.0\text{MPa}$	Geometry • Length $L_1 = 2\text{m}$ • Distance with NF $d = 0.0\text{m}$
Mechanical Properties: • Friction angle: $\phi = 26.6°$ • Cohesion $c = 0.1\text{MPa}$ • Tensile strength: $T_0 = 0.2\text{MPa}$ • Normal stiffness $K_n = 0.5\times10^6\text{MPa/m}$ • Shear stiffness $K_s = 0.25\times10^6\text{MPa/m}$	Mechanical Properties: • Young's modulus $E = 1.4\times10^4\text{MPa}$ • Poisson's ratio $v = 0.1$ • Bulk modulus $K = 4.5\times10^4\text{MPa}$ • Porosity $n = 0.01$ • Dynamic permeability $k = 4.053\times10^{-7}\text{darcy}$ • Fluid diffusivity c^f	Fluid Properties: • Fluid pressure $p = 3.0\text{MPa}$ • Fluid bulk modulus $K_f = 2.5\times10^3\text{MPa}$

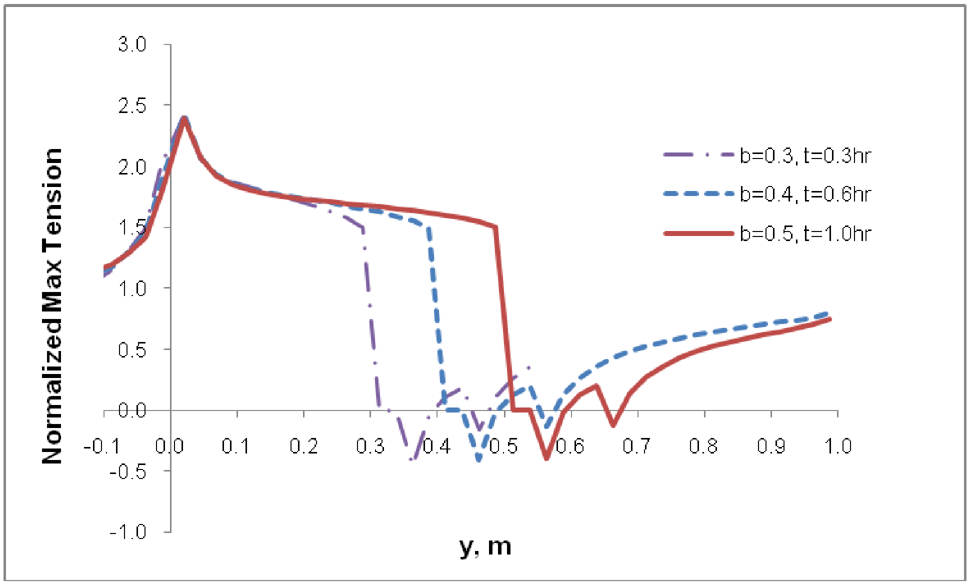

Fig. 5.22 Normalized maximum tensile stress along NF at different fluid invaded lengths along NF (*b*) and time (t) considering poroelastic effects (C_f=6.16×10^{-6}m^2/s).

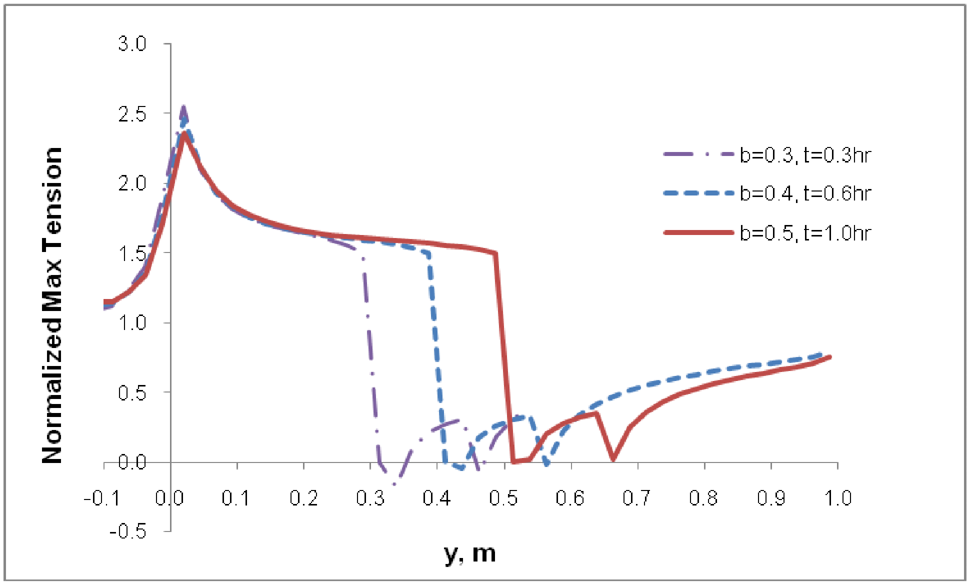

Fig. 5.23 Normalized maximum tensile stress along NF at different fluid invaded lengths along NF (*b*) and time (t) considering poroelastic effects (C_f=6.16×10^{-5}m^2/s).

The normalized maximum tensile stress generated along the NF with increasing time and fluid infiltration (for a fluid diffusivity, C_f , of 6.16×10^{-6}m^2/s and 6.16×10^{-5}m^2/s) are plotted in **Fig. 5.22** and **Fig. 5.23**, respectively. Compared with **Fig. 5.16**, it can be seen that poroelastic effect caused by fluid diffusion can significantly decrease the value of tension peak at each time step, decreasing the possibility for fracture re-initiation along the NF. For a fluid with higher value of diffusivity, poroelastic effect is more significant. As shown in **Fig. 5.23**, tension peak diminishes with time and approaches zero, and the values of tension peaks are reduced more when compared to those plotted in **Fig. 5.22**.

5.3 Hydraulic Fracture Trajectories Near a Natural Fracture

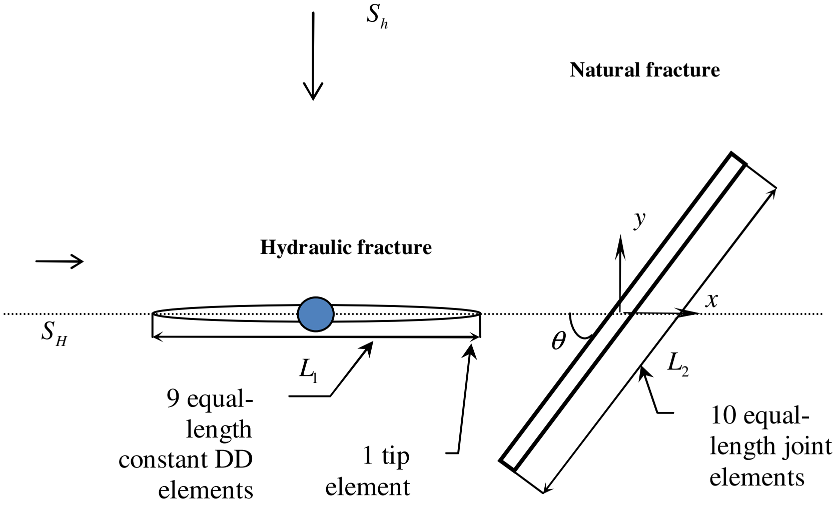

Fig. 5.24 A HF propagating towards a NF and mesh arrangement at initial condition.

Table 5.6 Input parameters for Barnett shale in Section 5.3 (Palmer et al. 2007).

Joints	Rock	HF
Geometry: • Orientation $\theta = 76°$ • Length $L_2 = 2.06\text{m}$	In-situ Stresses: • $S_H = -43\text{MPa}$ • $S_h = -39\text{MPa}$	Geometry • Length $L_1 = 2\text{m}$ • Distance with NF $d = 1\text{m}$ • Slant angle α
Mechanical Properties: • Friction angle: $\phi = 31°$ • Cohesion $c = 2.2\text{MPa}$ • Tensile strength: $T_0 = 2.0\text{MPa}$ • Normal stiffness $K_n = 0.5\times10^4\,\text{MPa/m}$ • Shear stiffness $K_s = 0.25\times10^4\,\text{MPa/m}$	Mechanical Properties: • Young's modulus $E = 2.07\times10^4\,\text{MPa}$ • Poisson's ratio $v = 0.25$	Fluid Properties: • Fluid pressure $p = 44\text{MPa}$

The second modeling attempt was done to model the trajectories of a HF emanating from a wellbore and propagating towards a NF, which is oriented θ degree to the axis of maximum horizontal stress S_H. Fluid pressure distribution along the HF is assumed constant. The mesh arrangement along the hydraulic fracture and natural fracture at the initial condition is plotted in **Fig. 5.24**. The hydraulic fracture half length is initially (at t=0) modeled by using 10 equal length elements, with 9 constant DD elements and one tip element at the fracture tip. The natural fracture is modeled using 10 equal length joint elements. With the growth of hydraulic fracture, the tip element reduces to a constant DD element, and a new tip element is added ahead of the previous tip element. Increment of hydraulic fracture length within each time step is fixed to be one element length, so that remeshing of the fracture is avoided. The input parameters are for Barnett shale (Palmer et al. 2007) as listed in **Table 5.6**. We first checked the fracture trajectories by using joint models that include initial joint deformation (as described in Section **4.1.1.2**).

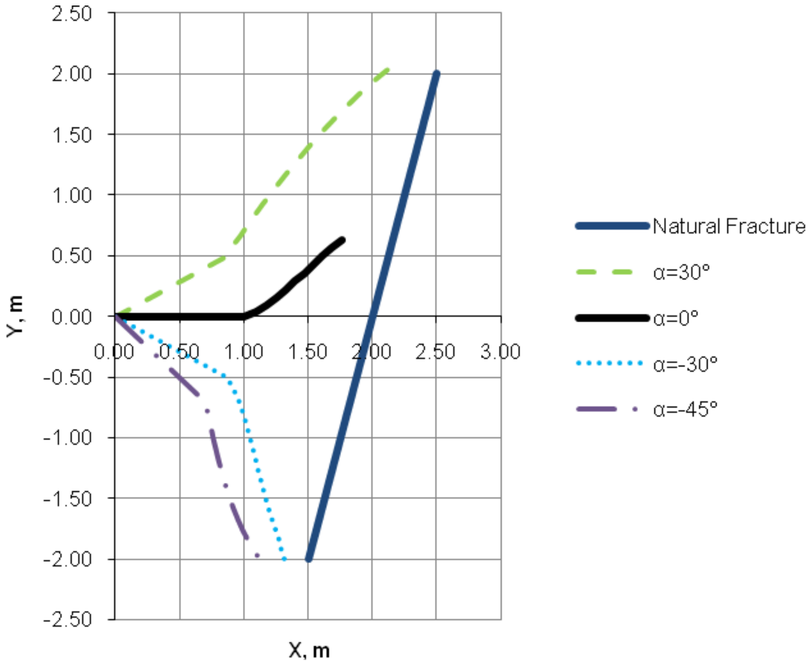

Fig. 5.25 Deflection of HFs at different orientation angles (*α*) when propagating towards a NF.

As can be seen from **Fig. 5.26**, fractures initially slanted at different angles (due to stress localization and ruptures at local flaws or micro-cracks in the rock formation immediately adjacent to the wellbore, fracture could initiate in certain direction initially. Another scenario would be for an inclined well, fracture would initially have an angle with respect to the direction of maximum horizontal stress) would propagate perpendicular to the direction of minimum far-field stresses under biaxial stresses without the presence of a NF. With NF located in front of the HF, the HF would deviate from its original path and bend near the NF, as shown in **Fig. 5.25**. In this case, as the joint model that includes initial deformation under far-field stresses was used, the deformation along the joint has changed the stress field around the HF tip, and therefore has changed its propagation path. It will be shown later that whether the deformation along the joint due to the far-field stresses is considered or not can affect the simulation results of HF trajectories.

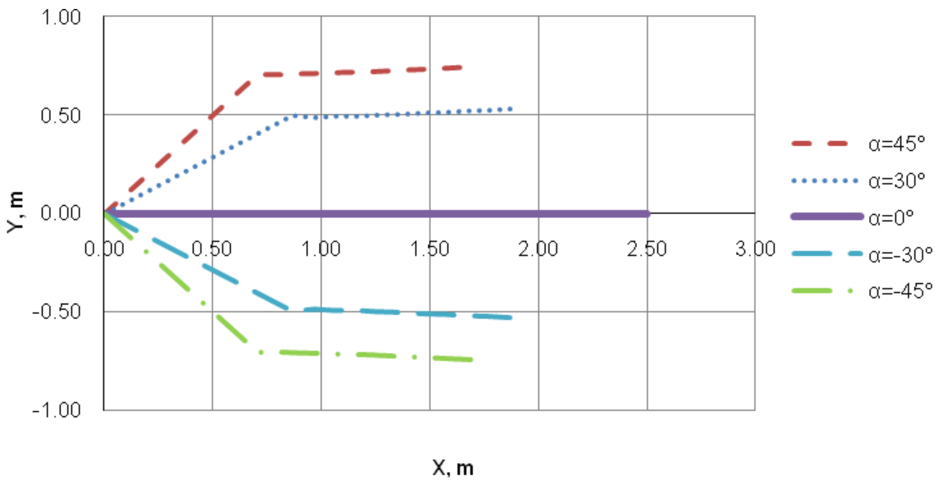

Fig. 5.26 Fracture trajectories propagating under biaxial stresses without the presence of a NF for HF at different slant angles (α).

The fracture deviation behavior would be of great importance for us to predict or monitor during the stimulation practice. Ideally we would like to design a fracturing treatment to create as much as conductive paths as possible, either by directly crossing NF or reinitiating new fractures from the NF. HF fracture bending or blunting at the NF are what we aim to avoid. Therefore, the following parametric studies are conducted to investigate the influence of different rock or fluid properties on the fracture trajectories.

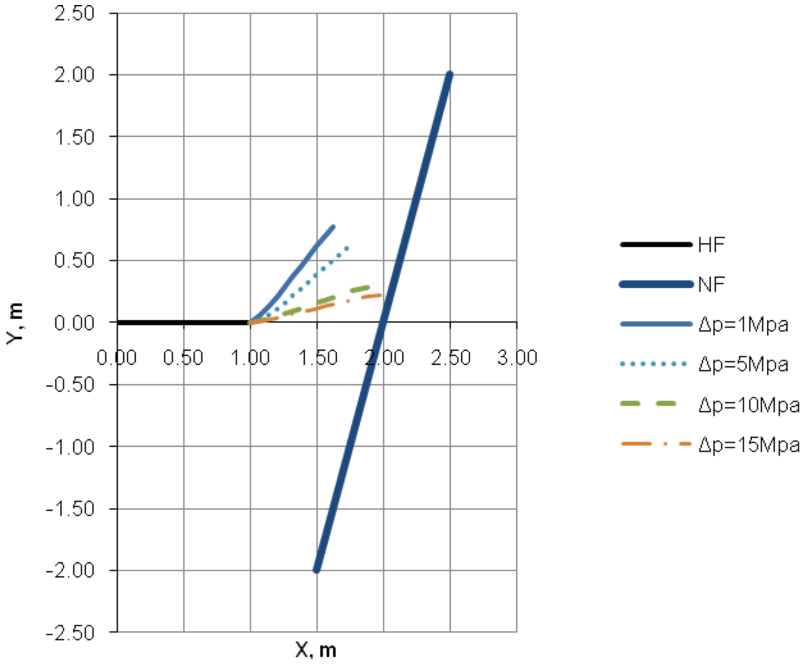

Fig. 5.27 Fracture trajectories under different net pressures (*Δp*).

Net pressure of the HF is a factor that can affect fracture propagation near a NF as shown in **Fig. 5.27**. A fracture under higher net pressure deviates less from its original path**.** A tensile fracture under a higher net pressure has a higher driving force at the fracture tip, so perturbation of the stress field induced by the NF appears to be less influential. The implication for stimulation practices is that fractures with higher net fluid pressure have less bending and are more likely to propagate towards a naturally-fractured reservoir. Once the fracture coalesces with NF, we could expect the onset of even greater pressure drop along the fracture paths; therefore higher net fluid pressure is needed when fracturing naturally-fractured reservoirs.

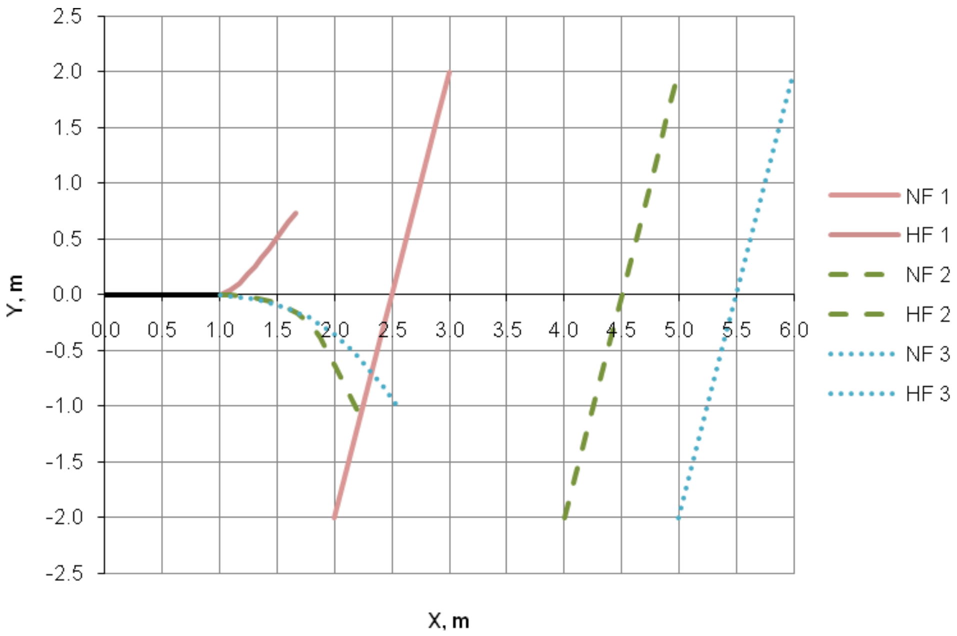

Fig. 5.28 Fracture trajectories under different distances from fracture tip to NF.

The NF may be located at different distances relative to the HF tip. As plotted in **Fig. 5.28**, the smaller the distance between NF and the fracture tip, the greater deviation exhibited at the fracture tip. When the NF is located further from the HF, the influence of deformation along the NF on the stress field around the HF tip gets smaller, so HF deviation becomes smaller. The fracture trajectory may either go to the left or the right side of the original path, depending on the specific in-situ stress field at the fracture tip.

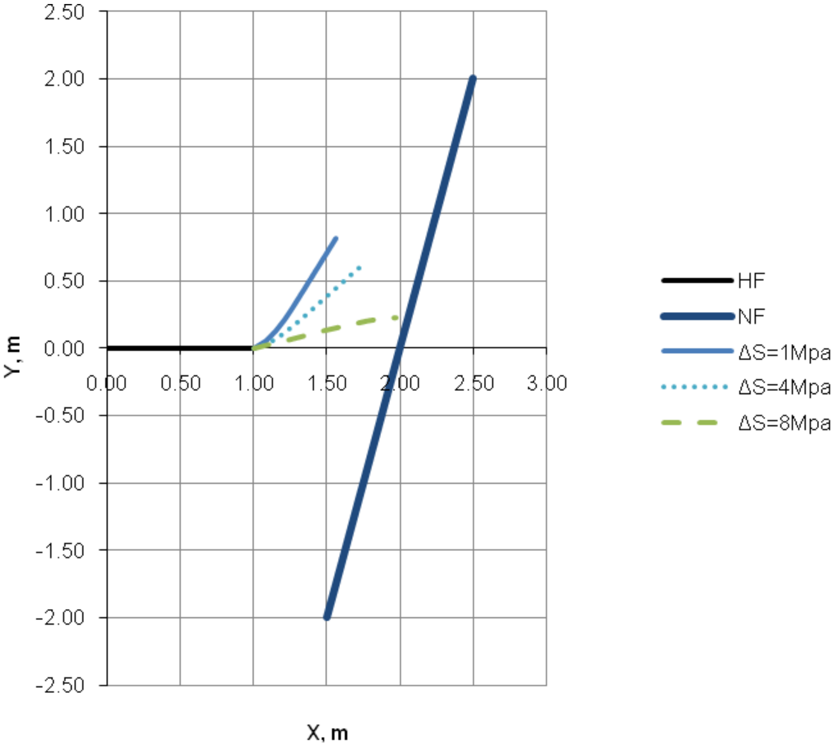

Fig. 5.29 Fracture trajectories under different far-field stress differences (*Δs*).

HF also shows different degrees of deviation from its original paths under different differences between the maximum in-situ stress (S_H) and minimum in-situ stress (S_h), as shown in **Fig. 5.29**. When the difference is small (the stress-field approaches isotropic condition), the perturbation of the stress field at the HF tip brought by the NF is more significant, so the bending of the HF is more significant.

Fracture trajectories calculated by using joint models that do not consider initial joint deformation (as described in 4.1.1.1) are shown in **Fig. 5.30**. As compared with **Fig. 5.25**, fracture paths are not influenced by the presence of NF. Because in this case, joint deformation due to far-field stresses is zero (as demonstrated in Section **4.3.2**, a joint model that excludes initial joint deformation would have zero normal/shear displacements and normal/shear stresses corresponding to the action of the far-field stresses). HF tip-induced joint deformation and stresses are also negligible as the tip is far enough from the NF (about 1m). Therefore, the joint does not perturb the stress-field around HF until the HF tip arrives very close to the NF, so that HF will not deviate significantly from its original path.

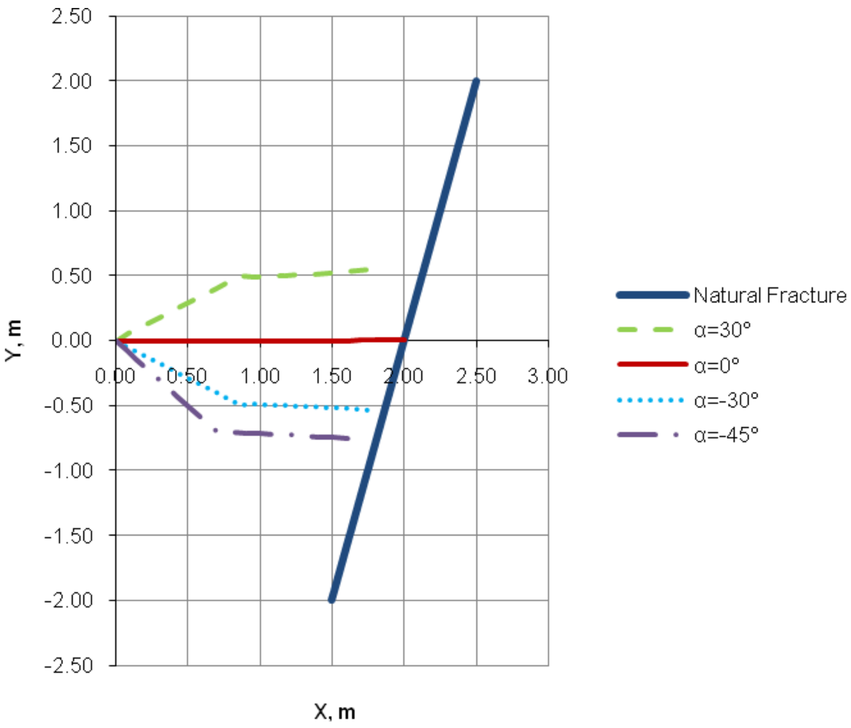

Fig. 5.30 Trajectories of HF propagating towards a NF at different slant angles (*α*).

Analysis based on this type of joint model might give a better representation for formations where the pre-existing fractures have been subjected to the far-field stresses for long time and have reached mechanical equilibrium prior to the process of hydraulic fracturing. Selection of joint model would have direct impact on the modelling results of fracture propagation near NFs. Therefore, carefully consideration of geomechanical characteristics of the reservoir is needed to get reliable modelling results.

5.4 Hydraulic Fracture Propagation by Using Newtonian Fluid Flow

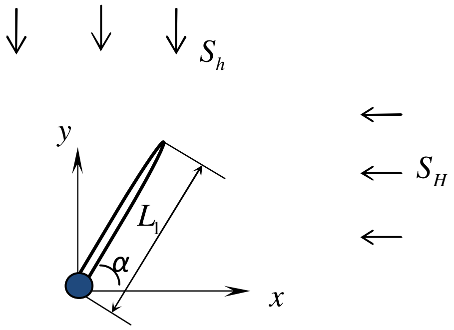

Fig. 5.31 An initially straight pressurized crack under biaxial stresses.

Simulation of the hydraulically induced fracture (**Fig. 5.31**) is carried out assuming a Newtonian fluid flow model. The input parameters are listed in **Table 5.7**. The fracture trajectories were calculated under different fluid injection rates and viscosities, and the results are plotted in **Fig. 5.32** and **Fig. 5.33**.

Table 5.7 Input parameters for simulating a HF using Newtonian fluid model

Rock	HF
In-situ Stresses: • $S_H = -2.0\text{MPa}$ • $S_h = -0.5\text{MPa}$	Geometry • Length $L_1 = 2\text{m}$ • Slant angle α=80°
Mechanical Properties: • Young's modulus $E = 1.4\times10^4\,\text{MPa}$ • Poisson's ratio $v = 0.1$	Fluid Properties: • Injection rate q • Viscosity μ

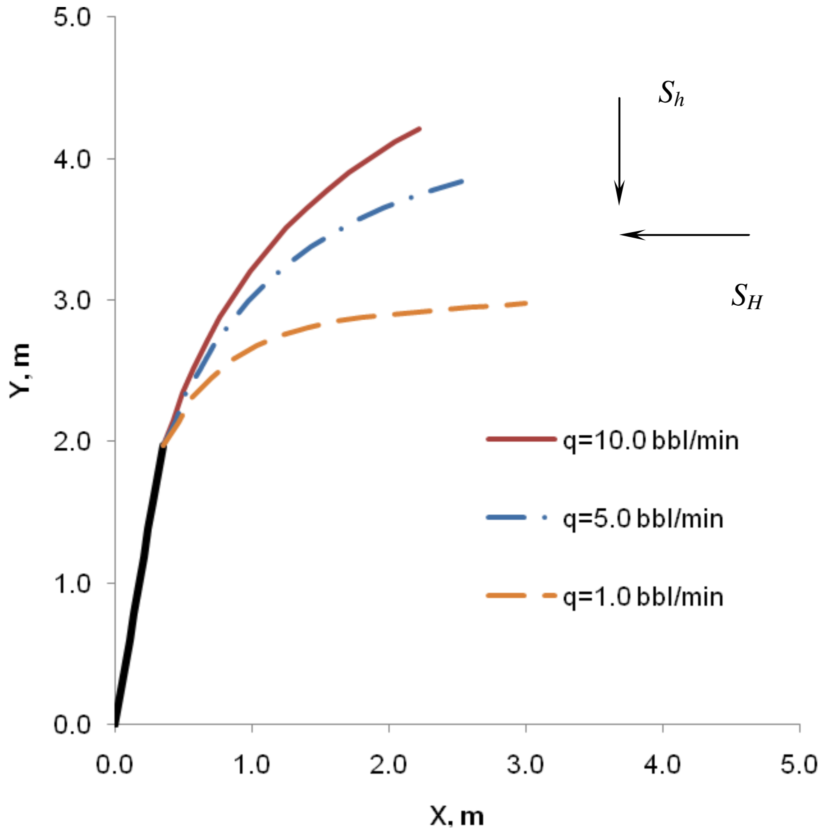

Fig. 5.32 Fracture trajectories under different fluid injection rates (q) at the wellbore (μ=1.0cp).

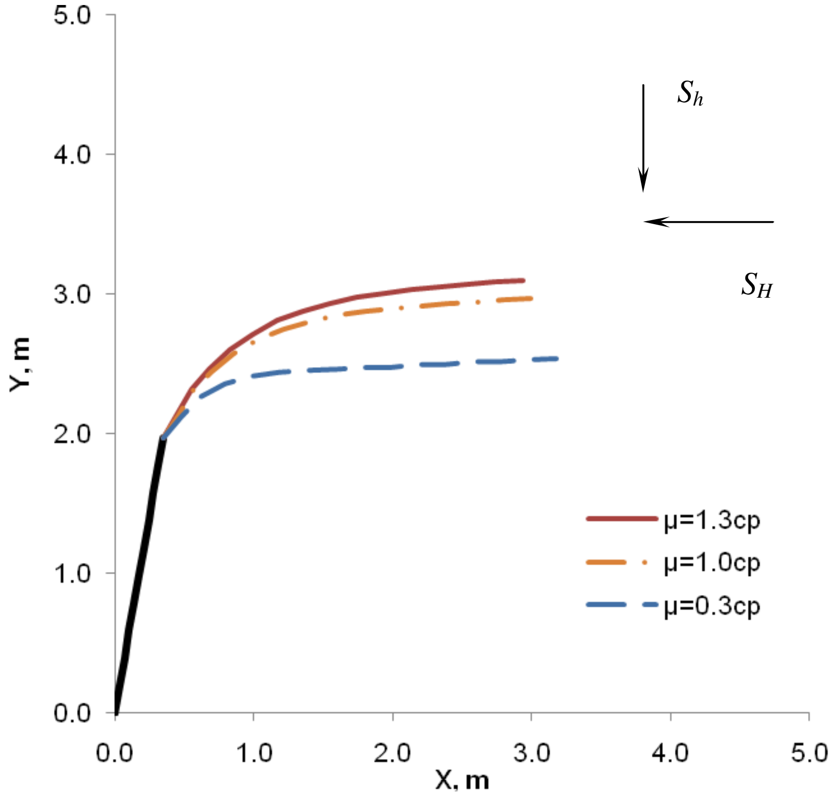

Fig. 5.33 Fracture trajectories under different fluid viscosities (*μ*) (*q*=1.0bbl/min).

As can be seen from **Fig. 5.32**, the fracture, which initially slanted at 80° with the direction of maximum horizontal stress S_H, will gradually turn and propagate along the direction of maximum horizontal stress under the influence of far-field stresses. When the injection rate is higher, which is 10.0bbl/min, the fracture travels longer distance before turning to the direction of maximum horizontal stress, as a fracture under higher injection rate has bigger resistance against the far-field compressive stresses. For lower injection rate, which is 5.0bbl/min and 1.0bbl/min, the fracture will travel shorter distance while turning. Similarly, as shown in **Fig. 5.33**, when the fracturing fluid has higher viscosity (1.3cp, viscosity of water at 10 °C), the hydraulic fracture will travel longer distance before turning than those with a lower viscosity (1.0cp and 0.3cp, viscosity of water at 20 ˚C and 90 ˚C respectively).

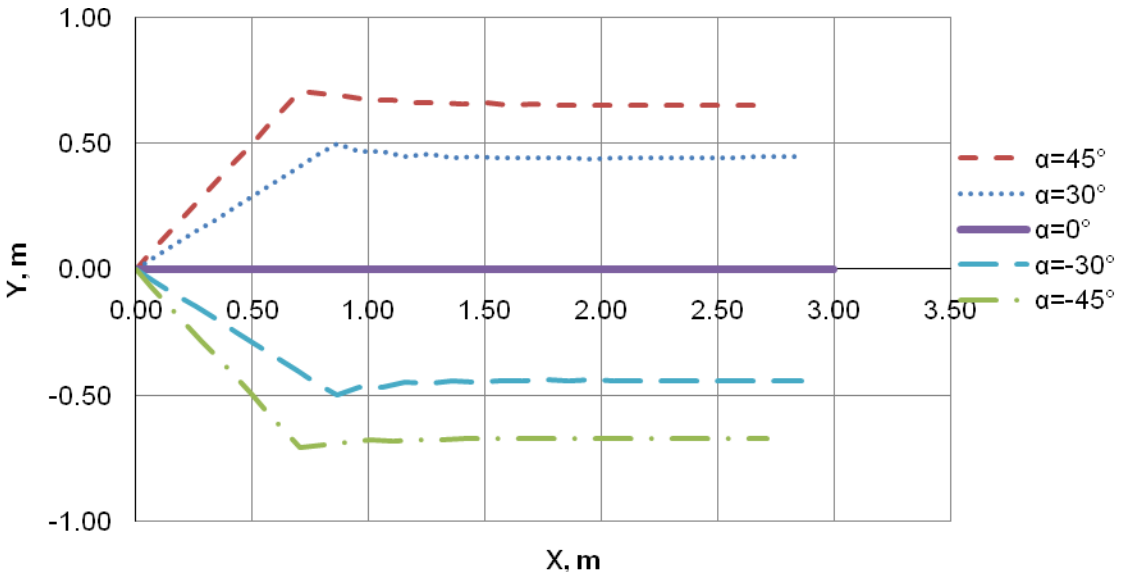

Fig. 5.34 Fracture trajectories for HF propagating under biaxial stresses at different slant angles (α) using Newtonian fluid flow model.

The trajectories for HF propagating under biaxial stresses at different slant angles using a Newtonian fluid flow model are plotted in **Fig. 5.34**. As compared with **Fig. 5.26**, the fractures follow similar trajectories as results simulated by using constant pressure model. Hence the model outputs for fracture footprints by using Newtonian fluid model are stable and reliable. It predicts that HF will propagate along the direction of maximum horizontal stress, S_H.

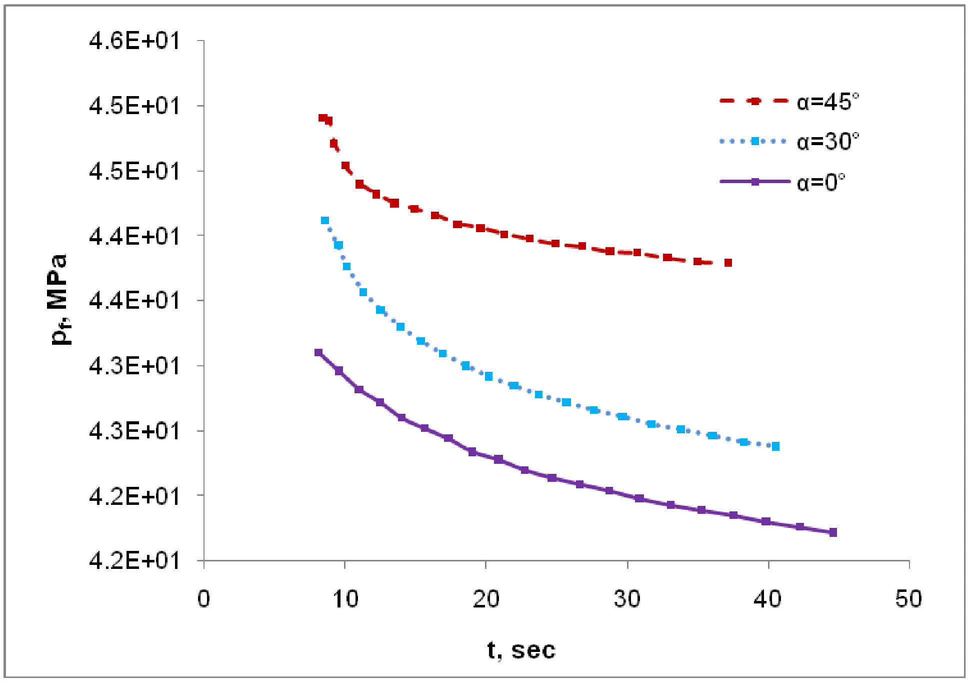

Fig. 5.35 Fluid pressure at the wellbore (*x*=0) with time by using Newtonian fluid model for HF at different slant angles (*α*).

The variation of fluid pressure at the wellbore with time for HF at different slant angles α is plotted in **Fig. 5.35**. Under the boundary condition of constant injection rate at the wellbore, the pressure at the wellbore required for the fracture to propagate decreases with time. As the fracture grows and the fracture aperture increases, less energy is required to propagate the HF and the pressure is decreasing. This agrees with the results calculated by a classical KGD model (Geertsma and de Klerk 1969).

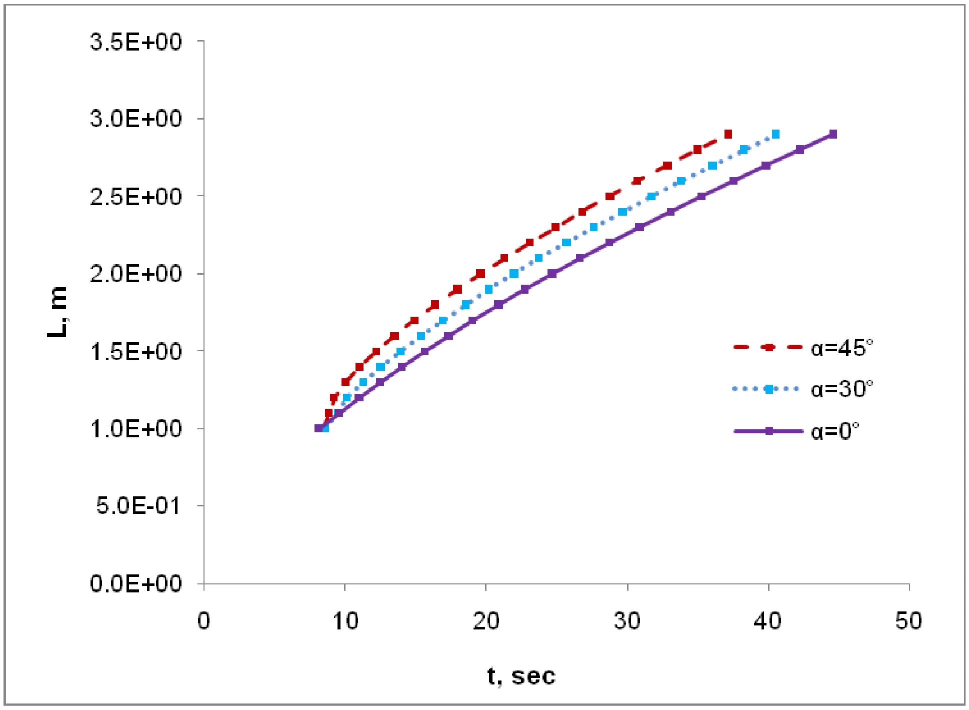

Fig. 5.36 Fracture length with time by using Newtonian fluid model for HF at different slant angles (α).

It can also be observed that for a HF with a bigger slant angle, the pressure at the wellbore is higher than those with a smaller slant angle. Similarly, we can see from **Fig. 5.36** that the higher the slant angle, the more slowly the fracture length increases with time. We may conclude that more energy is required for a HF with bigger slant angle to grow within the rock.

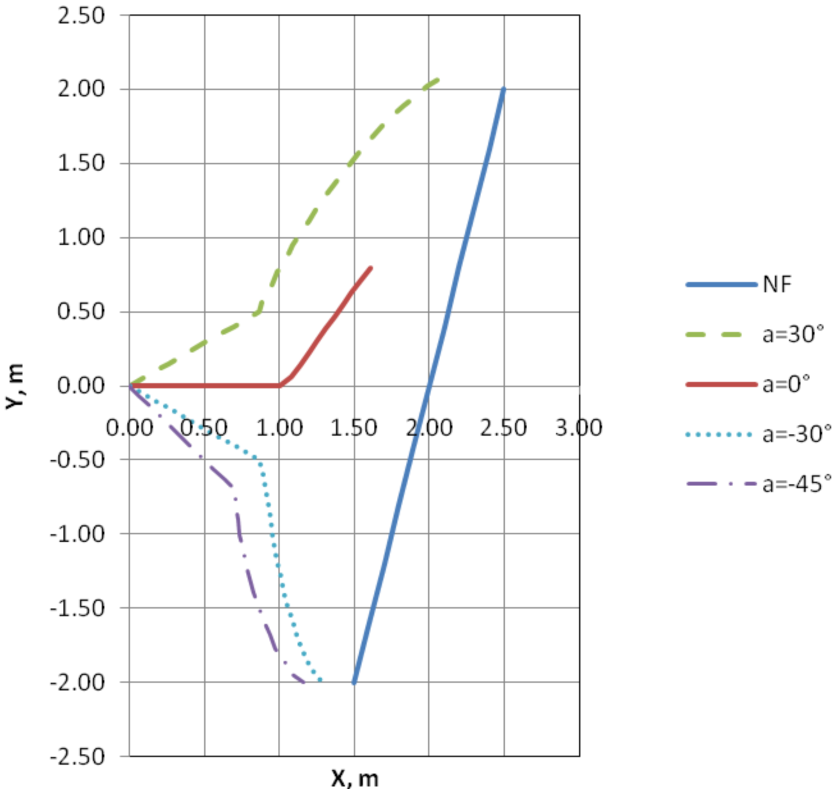

Fig. 5.37 Deflection of HFs at different orientation angles (α) when propagating towards a NF simulated by using a joint model that includes initial deformation and a Newtonian fluid model.

HF trajectories near a NF by using a Newtonian fluid model and joint models that include and exclude initial joint deformations are simulated and plotted in **Fig. 5.37** and **Fig. 5.38**, respectively. The input parameters are similar as listed in **Table 5.6** except that the fluid is modeled to have a viscosity μ=1.0cp and the injection rate at the wellbore q=1.0 bbl/min. As can be seen, fracture trajectories are identical as those plotted in **Fig. 5.25** and **Fig. 5.30**. The model outputs for fracture footprints by using Newtonian fluid model near NF are stable and reliable.

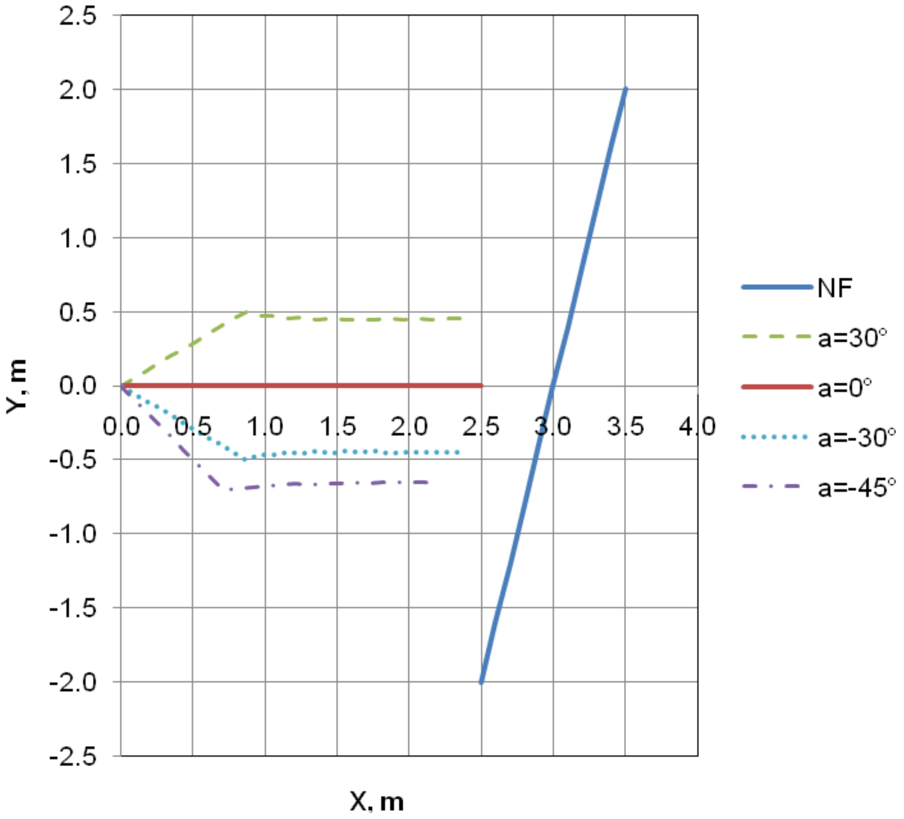

Fig. 5.38 Deflection of HFs at different orientation angles (α) when propagating towards a NF simulated by using a joint model that excludes initial deformation and a Newtonian fluid model.

Fracture trajectories under different fluid injection rates at the wellbore by using a Newtonian fluid model and joint models that include and exclude the initial joint deformation are simulated and plotted in **Fig. 5.39** and **Fig. 5.40**, respectively. It can be observed from **Fig. 5.39** that fracture trajectories are identical under three different injection rates and that they are not sensitive to the fluid injection rates when using a joint model that include initial deformation. In this type of joint model, we can see that the NF is a predominant factor in controlling the HF trajectory. The initial deformation along the NF (when included) is much more influential to the stress field around the HF than the fluid flow within the HF.

In contrast, HF shows three different routes under different injection rates when a joint model that excludes the initial joint deformation is used, as plotted in **Fig. 5.40**. We can observe that fracture under higher injection rate deviates more from the direction of maximum horizontal stress (S_H). Simulation results from this type of joint model exhibits that the NF has a much smaller influence on the stress field around the HF and that the influence of fluid flow within the HF overweighs and can thereby affect the fracture trajectory.

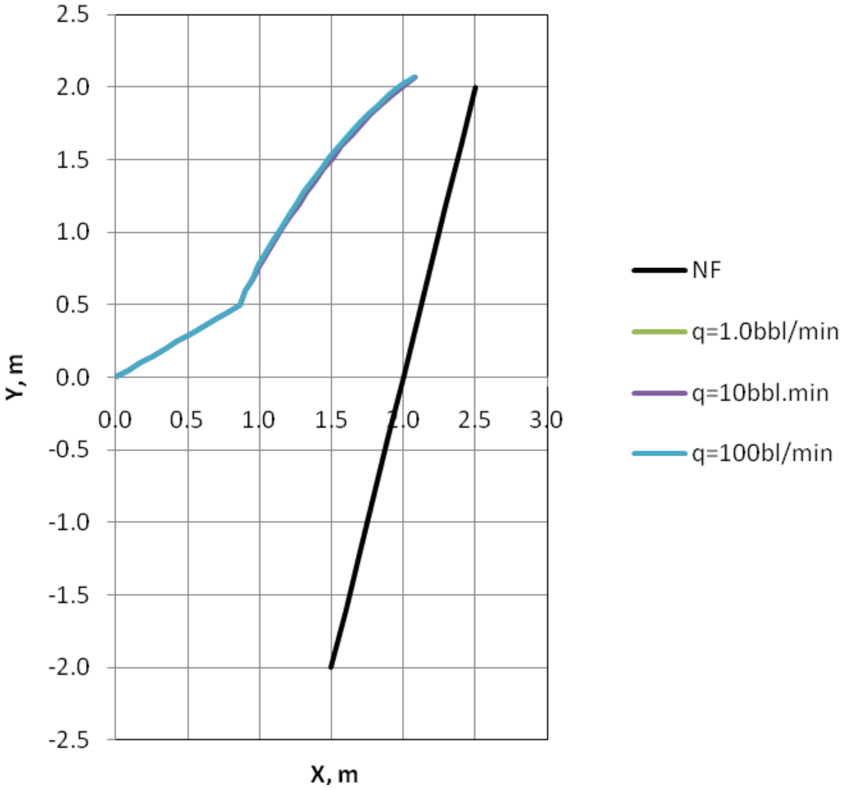

Fig. 5.39 Deflection of HF (α=30°) under different injection rates at the wellbore (q) when propagating towards a NF simulated by using a joint model that includes initial deformation and a Newtonian fluid model.

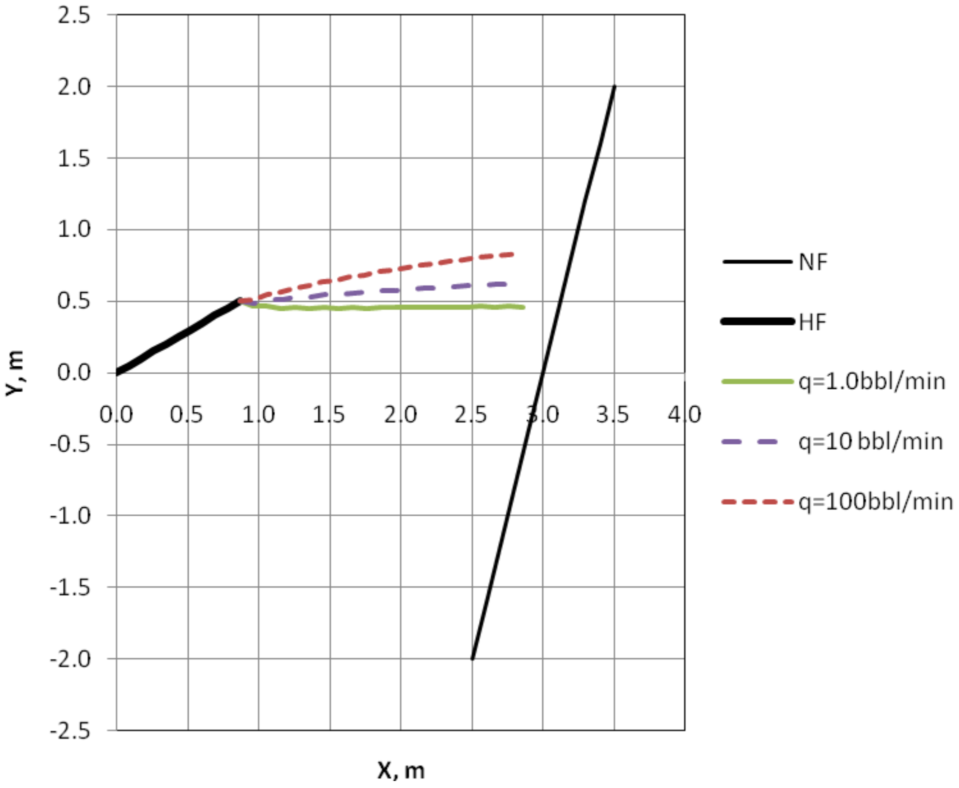

Fig. 5.40 Deflection of HF (α=30˚) under different injection rates at the wellbore (*q*) when propagating towards a NF simulated by using a joint model that excludes initial deformation and a Newtonian fluid model.

6 SUMMARY AND CONCLUSIONS

6.1 Summary

In this thesis, the interaction between a HF and a NF are investigated numerically by considering the mechanical deformation of the rock in response to the fluid pressure acting on the fracture surface, the fluid flow within the fracture, and the fracture propagation in the formation. Rock deformation is considered to be elastic while the poroelastic effect associated with pore pressure diffusion is included. Fluid pressure is first considered to be uniformly distributed in the HF, and then the pressure distribution is found using flow of a Newtonian fluid in the crack. Fracture propagation is modeled using the stress structural criterion. A special type of DD element (joint element) is used to describe different joint contact modes (stick, open and yield) for numerical analysis of HF interaction with NF.

The mechanical response of the NF to a static HF is studied to predict the probable location for the onset of new tensile crack before HF coalesces with the NF. The stage when the fluid invades the NF is also considered by simulating a sequence of static states of fluid with uniform pressure distribution along the HF and NF.

Hydraulic fracture trajectories near a NF before HF coalesces with the NF under different joint, rock and fluid properties were modeled using two different joint models (which exclude or included initial joint deformation) and two different fluid flow models (prescribed uniform pressure model or Newtonian fluid flow model).

Future research on the interaction between a HF and a NF can be done by modeling a complete set of stages of HF and NF interaction: HF approaching NF, coalescence, subsequent fluid infiltration, and fracture re-initiation from the NF.

6.2 Conclusions

1. During the stage that a HF approaches a NF before coalescence, the possibility of fracture re-initiation across the NF is enhanced when the NF has weak interfaces; a stronger NF tends to inhibit fracture re-initiation. In terms of re-initiation location, a step-over (offset) is more likely to occur for HF interacting with a weaker joint, as the stress localization tends to be mitigated by sliding of the NF; a strong joint whose surface is fully bonded promotes direct crossing.
2. During the stage of fluid infiltration along the NF, a maximum tensile stress peak is generated at the end of the opening zone along the NF ahead of the fluid front. The location and value of the tension peak is a function of fluid pressure and fluid infiltrated length.
3. Poroelastic effect arising from fluid diffusion into the rock deformation reduces HF aperture and thus reduces tensile stress near the center of the NF ahead of the HF tip before HF reaches NF. While fluid flows along the NF, poroelastic effects can reduce the value of tension peak, decreasing the possibility of fracture re-initiation with time. However, rapid fluid diffusion into a NF can cause it to slip prior to HF arrival, promoting offset situations.

4. Hydraulic fractures subjected to higher injection rates or fracturing fluids of higher viscosity propagate longer distance before turning to the direction of maximum horizontal stress.
5. Fracture trajectories near a NF tend to bend and deviate from the direction of maximum horizontal stress when using a joint model that includes the initial joint deformation.
6. Fracture trajectories are less dependent on the injection rate or fluid viscosity when NF slips under initial stresses and the influence of NF is more predominant; whereas, fracture trajectories are more dominated by the HF variables such as injection rate and fluid viscosity when the influence of NF is smaller, e.g., when a joint is in equilibrium with the in-situ stresses.

NOMENCLATURE

A_{ns}^{ij} = boundary influence coefficients (gives the normal stress at the midpoint of the i^{th} element due to a constant shear DD over the j^{th} element)

B = Skempton's pore pressure coefficient

c = cohesion, MPa

C_f = Fluid diffusivity, m²/s

d = characteristic length of fracture process zone, m

D_x = displacement discontinuity with respect to *x*-axis, m

D_y = displacement discontinuity with respect to *y*-axis, m

D_s^j = total shear components of discontinuity with respect to the local co-ordinates *s* and *n* at the j^{th} element, m

D_n^j = total normal components of discontinuity with respect to the local co-ordinates *s* and *n* at the j^{th} element, m

$(D_s^i)_0$ = shear component of initial total joint deformation, m

$(D_n^i)_0$ = normal component of initial total joint deformation, m

$D_s^{i'}$ = shear component of the induced deformation, m

$D_n^{i'}$ = normal component of the induced deformation, m

E = Young's modulus, MPa

f_I = tensile driving force, MPa

f_{II} = shear driving force, MPa

F_I = normalized tensile driving force

F_{II} = normalized shear driving force

G = shear modulus of rock formation, MPa

k = dynamic permeability, md

K_u = undrained bulk modulus, MPa

K = rock's bulk modulus, MPa

K_I = Mode I stress intensity factor, $\mathrm{MPa \cdot m^{1/2}}$

K_{II} = Mode II stress intensity factor, $\mathrm{MPa \cdot m^{1/2}}$

K_{IC} = Mode I critical stress intensity factor, $\mathrm{MPa \cdot m^{1/2}}$

l = initial crack half length, m

L_1 = fracture length, m

L_2 = joint length, m

p = pressure, MPa

p_f = fluid pressure, MPa

$p(0,t)$ = pressure at the wellbore at time t, MPa

$p(x,t)$ = pressure at coordinate x at time t, MPa

Δp = pressure drop, MPa

q = fracturing fluid flow rate, bbl/min

$q(0,t)$ = injection rate at the wellbore (x=0) at time t, bbl/min

S_H = maximum horizontal stress, MPa

S_h = minimum horizontal stress, MPa

t = time point during a fracture treatment, s

T_0 = tensile strength, MPa

u_x = displacement with respect to x-axis, m

u_y = displacement with respect to y-axis, m

u_s^i = shear displacement at the midpoint of the i^{th} element, m

u_n^i = normal displacement at the midpoint of the i^{th} element, m

w = fracture width, m

w_j = level weighting factor

x = coordinate along direction of fracture propagation, m

y = coordinate along direction of fracture propagation, m

α = Biot's effective stress coefficient

μ = fluid viscosity, cp

ν = Poisson's ratio

ρ = density of the fracturing fluid, kg/m^3

ϕ = angle of friction, °

σ_n = in-situ normal rock stress perpendicular to fracture face, MPa

$\sigma_{\theta\theta}$ = tangential stress in radial coordinate, MPa

$\sigma_{r\theta}$ = shear stress in radial coordinate, MPa

σ_{rr} = radial stress in radial coordinate, MPa

σ_s^i = shear stress at the midpoint of the i^{th} element, MPa

σ_n^i = normal stress at the midpoint of the i^{th} element, MPa

REFERENCES

Batchelor, G.K. 1967. *An Introduction to Fluid Dynamics*. Cambridge, UK.: Cambridge University Press. Original edition. ISBN 0521 66396 2.

Berchenko, I. and Detournay, E. 1997. Deviation of Hydraulic Fractures through Poroelastic Stress Changes Induced by Fluid Injection and Pumping. *International Journal of Rock Mechanics and Mining Sciences* **34** (6): 1009-1019.

Biot, M.A. 1941. General Theory of Three-Dimensional Consolidation. *J. Appl. Phys.* **26**: 182-185.

Blanton, T.L. 1982. An Experimental Study of Interaction between Hydraulically Induced and Pre-Existing Fractures. Paper SPE 10847-MS presented at the SPE Unconventional Gas Recovery Symposium, Pittsburgh, Pennsylvania. DOI: 10.2118/10847-MS.

Bobet, A. 2001. Numerical Simulation of Initiation of Tensile and Shear Cracks. Paper presented at the 38th U.S. Symposium on Rock Mechanics (USRMS), Washington D.C., Swets & Zeitlinger Lisse.

Bobet, A. and Einstein, H.H. 1998. Fracture Coalescence in Rock-Type Materials under Uniaxial and Biaxial Compression. *Int. J. Rock Mech. Min. Sci.* **35**: 863-888.

Boone, T.J., Ingraffea, A.R., and Roegiers, J.C. 1991. Simulation of Hydraulic Fracture Propagation in Poroelastic Rock with Application to Stress Measurement

Techniques. *International Journal of Rock Mechanics and Mining Sciences & Geomechanics Abstracts* **28** (1): 1-14.

Chuprakov, D.A., Akulich, A., Siebrits, E. and Thiercelin, M. 2010. Hydraulic Fracture Propagation in a Naturally Fractured Reservoir. Paper SPE 128715-MS presented at the SPE Oil and Gas India Conference and Exhibition, Mumbai, India. DOI: 10.2118/128715-MS.

Cooke, M.L. and Underwood, C.A. 2001. Fracture Termination and Step-over at Bedding Interfaces Due to Frictional Slip and Interface Opening. *Journal of Structural Geology* **23** (2-3): 223-238.

Crouch, S.L. 1976. *Analysis of Stresses and Displacements around Underground Excavations: An Application of the Displacement Discontinuity Method*. Minneapolis: Dept. of Civil and Mineral Engineering, University of Minnesota.

Crouch, S.L. and Starfield, A.M. 1983. *Boundary Element Methods in Solid Mechanics*. London: George Allen & Unwin. Original edition. ISBN 004620010X.

Detournay, E. and Cheng, A.H.D. 1991. Plane Strain Analysis of a Stationary Hydraulic Fracture in a Poroelastic Medium. *International Journal of Solids and Structures* **27** (13): 1645-1662.

Dobroskok, A., Ghassemi, A., and Linkov, A. 2005. Extended Structural Criterion for Numerical Simulation of Crack Propagation and Coalescence under Compressive Loads. *International Journal of Fracture* **133**: 223-246.

Dong, C.Y. and de Pater, C.J. 2001. Numerical Implementation of Displacement Discontinuity Method and Its Application in Hydraulic Fracturing. *Computer Methods in Applied Mechanics and Engineering* **191** (8-10): 745-760.

Fisher, M.K., Wright, C.A., Davidson, B.M. et al. 2002. Integrating Fracture Mapping Technologies to Optimize Stimulations in the Barnett Shale. Paper presented at the SPE Annual Technical Conference and Exhibition, San Antonio, Texas. Copyright 2002, Society of Petroleum Engineers Inc. 77441.

Gdoutos, E.E. 2005. *Fracture Mechanics: An Introduction.* Dordrecht, The Netherlands: Springer. Original edition. ISBN 1-4020-3153-X.

Geertsma, J. and de Klerk, F. 1969. A Rapid Method of Predicting Width and Extent of Hydraulically Induced Fractures. *SPE Journal of Petroleum Technology* **21** (12): 1571-1581.

Ghassemi, A. and Zhang, Q. 2006. Porothermoelastic Analysis of the Response of a Stationary Crack Using the Displacement Discontinuity Method. *Journal of Engineering Mechanics* **132**: 26-33.

Griffith, A.A. 1924. The Theory of Rupture. *Proceedings 1st International Congress Applied Mechanics*: 55-63, Delft, Holland.

Huang, N.C. and Russell, S.G. 1985. Hydraulic Fracturing of a Saturated Porous Medium-II: Special Cases. *Theoretical and Applied Fracture Mechanics* **4** (3): 215-222.

Jaeger, J.C., Cook, N.G.W., and Zimmerman, R.W. 2007. *Fundamentals of Rock Mechanics*. Malden, MA: Blackwell Publishing. Original edition. ISBN 978-0-632-05759-7.

Khristianovic, S.A. and Zheltov, Y.P. 1955. Formation of Vertical Fractures by Means of Highly Viscous Liquid. Paper presented at the 4th World Petroleum Congress, Rome, Italy. 579-586. World Petroleum Congress.

Koshelev, V. and Ghassemi, A. 2003. Hydraulic Fracture Propagation near a Natural Discontinuity. In *Twenty-Eight Workshop on Geothermal Reservoir Engineering*. Stanford University, Stanford, California.

Matt Blauch and Grieser, B. Special Techniques Tap Shale Gas. http://www.epmag.com/archives/features/307.htm. Accessed May 10, 2010.

McTigue, D.F. 1986. Thermoelastic Response of Fluid-Saturated Porous Rock. *J. Geophys. Res.* **91** (B9): 9,533-539,542.

Nordgren, R.P. 1972. Propagation of a Vertical Hydraulic Fracture. *SPE Journal* **12** (4): 306-314.

Palmer, I.D., Moschovidis, Z.A., and Cameron, J.R. 2007. Modeling Shear Failure and Stimulation of the Barnett Shale after Hydraulic Fracturing. Paper SPE 106113 presented at the SPE Hydraulic Fracturing Technology Conference, College Station, Texas, U.S.A.

Perkins, T.K. and Kern, L.R. 1961. Widths of Hydraulic Fractures. *SPE Journal of Petroleum Technology* **13** (9): 937-949.

Potluri, N.K., Zhu, D., and Hill, A.D. 2005. The Effect of Natural Fractures on Hydraulic Fracture Propagation. Paper SPE 94568-MS presented at the SPE European Formation Damage Conference, Scheveningen, The Netherlands.

Rao, Q., Sun, Z., Stephansson, O. et al. 2003. Shear Fracture (Mode II) of Brittle Rock. *Rock Mech. Mining Sci.* **40**: 355-375.

Renshaw, C.E. and Pollard, D.D. 1995. An Experimentally Verified Criterion for Propagation across Unbounded Frictional Interfaces in Brittle, Linear Elastic Materials. *International Journal of Rock Mechanics and Mining Science & Geomechanics Abstracts* **32** (3): 237-249.

Rice, J.R. 1968. Mathematical Analysis in the Mechanics of Fracture. In *Fracture, An Advanced Treatise.* New York: Academic Press. Vol II: Mathematical Fundamentals. H. Liebowitz. ed.

Ruina, A.L. 1978. Influence of Coupled Deformation-Diffusion Effects on the Retardation of Hydraulic Fracture. In *19th US Rock Mechanics Symposium (USRMS)*:274-282. Reno, Nevada: University of Nevada Press, ARMA.

Sneddon, I.N. 1946. The Distribution of Stress in the Neighborhood of a Crack in an Elastic Solid. In *Proc. R. Soc. London, Ser. A*, 187:229-260.

Tang, C.A., Lin, P., Wong, R.H.C. et al. 2001. Analysis of Crack Coalescence in Rock-Like Materials Containing Three Flaws - Part II: Numerical Approach. *Int. J. Rock Mech. Min. Sci.* **38**: 925-939.

Thiercelin, M.J. and Makkhyu, E. 2007. Stress Field in the Vicinity of a Natural Fault Activated by the Propagation of an Induced Hydraulic Fracture. In *Rock*

Mechanics: Meeting Society's Challenges and Demands. London: Taylor & Francis Group.

Vandamme, L., Detournay, E., and Cheng, A.H.-D. 1989. A Two-Dimensional Poroelastic Displacement Discontinuity Method for Hydraulic Fracture Simulation. *International Journal for Numerical and Analytical Methods in Geomechanics* **13** (2): 215-224.

Warpinski, N.R. and Teufel, L.W. 1987. Influence of Geologic Discontinuities on Hydraulic Fracture Propagation (Includes Associated Papers 17011 and 17074). *SPE Journal of Petroleum Technology* **39** (2): 209-220. DOI: 10.2118/13224-pa

Warpinski, N.R., Wolhart, S.L., and Wright, C.A. 2004. Analysis and Prediction of Microseismicity Induced by Hydraulic Fracturin. *SPE Journal* **9** (1): 24-33. DOI: 10.2118/87673-pa

Woo, C.W. and Ling, L.H. 1984. On Angled Crack Initiation under Biaxial Loading. *The Journal of Strain Analysis for Engineering Design* **19** (1): 51-59. DOI: 10.1243/03093247V191051

Wu, H., Chudnovsky, A., Dudley, J.W. et al. 2004. A Map of Fracture Behavior in the Vicinity of an Interface. Paper presented at the Gulf Rocks 2004, the 6th North America Rock Mechanics Symposium (NARMS), Houston, Texas. ARMA 04-620.

Yan, X. 2004. A Special Crack Tip Displacement Discontinuity Element. *Mechanics Research Communications* **31** (6): 651-659.

Zhang, X. and Jeffrey, R.G. 2006. The Role of Friction and Secondary Flaws on Deflection and Re-Initiation of Hydraulic Fractures at Orthogonal Pre-Existing Fractures. *Geophysical Journal International* **166**: 1454-1465.

Zhang, Z.X. 2002. An Empirical Relation between Mode I Fracture Toughness and the Tensile Strength of Rock. *International Journal of Rock Mechanics and Mining Sciences* **39** (3): 401-406.

APPENDIX A

EQUATIONS OF POROELASTICITY

In the poroelasticity theory (Biot 1941), using a tension positive sign convention, the governing equations describing different variables are:

Constitutive equations:

$$\Delta\varepsilon_{ij} = \frac{\Delta\sigma_{ij}}{2G}, i \neq j \text{ [dimensionless]} \quad \text{A.1}$$

$$\Delta\varepsilon_{kk} = \frac{\Delta\sigma_{kk}}{3K} + \frac{\alpha\Delta p}{K} \text{ [dimensionless]} \quad \text{A.2}$$

$$\Delta\sigma_{ij} = 2G\Delta\varepsilon_{ij} + \frac{2Gv}{1-2v}\Delta\varepsilon_{kk}\delta_{ij} - \alpha\Delta p\delta_{ij} \text{ (Pa)} \quad \text{A.3}$$

$$\Delta\zeta = \frac{\alpha\Delta\sigma_{kk}}{3K} + \frac{\alpha\Delta p}{BK} \text{ [dimensionless]} \quad \text{A.4}$$

$$p = M(\zeta - \alpha\varepsilon) \text{ (Pa)} \quad \text{A.5}$$

Eq. A.2 and **A.4** describe the volumetric response of the solid and fluid, respectively. σ_{ij} denotes the components of the total stress tensor; ε_{ij} denotes the components of the strain tensor related to the solid displacements, *u*, by $\varepsilon_{ij} = \frac{1}{2}(u_{i,j} + u_{j,i})$; *G*=shear modulus; *α*=Biot's effective stress coefficient; *p*=pore pressure; *K*=rock's bulk modulus; δ_{ij} =Kronecker delta (it equals unity for *i=j* and zero for *i≠j*); *B*=Skempton's pore pressure coefficient; *ζ*= variation of the fluid content per unit reference volume of the porous material; *M*=Biot's modulus.

Equilibrium equations:

$$\sigma_{ij,j} = -F_i \text{ (Pa/m)} \quad \text{......} \quad \text{A.6}$$

where F_i=solid body force (force per unit volume)

Darcy's law:

$$v_i = -\kappa(p_{,i} - f_i) \text{ (m/s)} \quad \text{......} \quad \text{A.7}$$

where v_i= fluid velocity, $\kappa=k/\mu$ (k: dynamic permeability; μ: fluid viscosity) and f_i=fluid body force (force per unit volume)

Continuity equation:

$$\frac{\partial \zeta}{\partial t} + v_{i,i} = \gamma \text{ (s}^{-1}\text{)} \quad \text{......} \quad \text{A.8}$$

$$Q = \int_0^t \gamma dt \quad \text{......} \quad \text{A.9}$$

where γ represents fluid source intensity and its integration over time yields the source strengths give by Q.

Field equations of Poroelasticity:

Navier equation for solid displacement:

$$G\nabla^2 u_i + \frac{1}{3}(G + 3K)\varepsilon_{,i} - \alpha p_{,i} = 0 \quad \text{......} \quad \text{A.10}$$

Diffusion equation for pore pressure p:

$$\kappa\nabla^2 p = \frac{1}{M}\frac{\partial p}{\partial t} + \alpha\frac{\partial \varepsilon}{\partial t} - M(\gamma - \kappa f_{i,i}) \quad \text{......} \quad \text{A.11}$$

APPENDIX B

NUMERICAL FORMULATIONS FOR TIP ELEMENTS

First consider arbitrary DD distributions along element length *2a*, as shown in **Fig. B.1:**

$$D_i = D_i\left(\xi\right), i = 1, 2 \qquad \text{B.1}$$

or

$$\begin{aligned} D_x &= D_x\left(\xi\right) \\ D_y &= D_y\left(\xi\right) \end{aligned} \qquad \text{B.2}$$

From a differential point of view, the differential displacements and stresses at field point (*x,y*) due to a differential element (with length *2dξ*) can be written as (Crouch and Starfield 1983, Yan 2004):

$$\begin{aligned} du_x &= D_x(\xi)\left[2(1-\nu)T_3 - yT_5\right] + D_y(\xi)\left[-(1-2\nu)T_2 - yT_4\right] \\ du_y &= D_x(\xi)\left[(1-2\nu)T_2 - yT_4\right] + D_y(\xi)\left[2(1-\nu)T_3 - yT_5\right] \end{aligned} \qquad \text{B.3}$$

$$\begin{aligned} d\sigma_{xx} &= 2GD_x(\xi)\left[2T_4 + yT_6\right] + 2GD_y(\xi)\left[-T_5 + yT_7\right] \\ d\sigma_{yy} &= 2GD_x(\xi)\left[-yT_6\right] + 2GD_y(\xi)\left[-T_5 - yT_7\right] \\ d\sigma_{xy} &= 2GD_x(\xi)\left[-T_5 + yT_7\right] + 2GD_y(\xi)\left[-yT_6\right] \end{aligned} \qquad \text{B.4}$$

where functions T_2, T_3, T_4, T_5, T_6, T_7 are given by

$$
\begin{aligned}
T_2(x,y,\xi,d\xi)/d\xi &= V_2(x,y,\xi) = -\frac{1}{4\pi(1-\nu)}\frac{x-\xi}{(x-\xi)^2+y^2}\\
T_3(x,y,\xi,d\xi)/d\xi &= V_3(x,y,\xi) = -\frac{1}{4\pi(1-\nu)}\frac{y}{(x-\xi)^2+y^2}\\
T_4(x,y,\xi,d\xi)/d\xi &= V_4(x,y,\xi) = \frac{2y}{4\pi(1-\nu)}\frac{x-\xi}{\{(x-\xi)^2+y^2\}^2}\\
T_5(x,y,\xi,d\xi)/d\xi &= V_5(x,y,\xi) = \frac{1}{4\pi(1-\nu)}\frac{(x-\xi)^2-y^2}{\{(x-\xi)^2+y^2\}^2}\\
T_6(x,y,\xi,d\xi)/d\xi &= V_6(x,y,\xi) = \frac{2}{4\pi(1-\nu)}\left\{\frac{(x-\xi)^3}{\{(x-\xi)^2+y^2\}^3}-\frac{3(x-\xi)y^2}{\{(x-\xi)^2+y^2\}^3}\right\}\\
T_7(x,y,\xi,d\xi)/d\xi &= V_7(x,y,\xi) = \frac{2y}{4\pi(1-\nu)}\left\{\frac{3(x-\xi)^2}{\{(x-\xi)^2+y^2\}^3}-\frac{y^2}{\{(x-\xi)^2+y^2\}^3}\right\}
\end{aligned}
\qquad .\mathrm{B.5}
$$

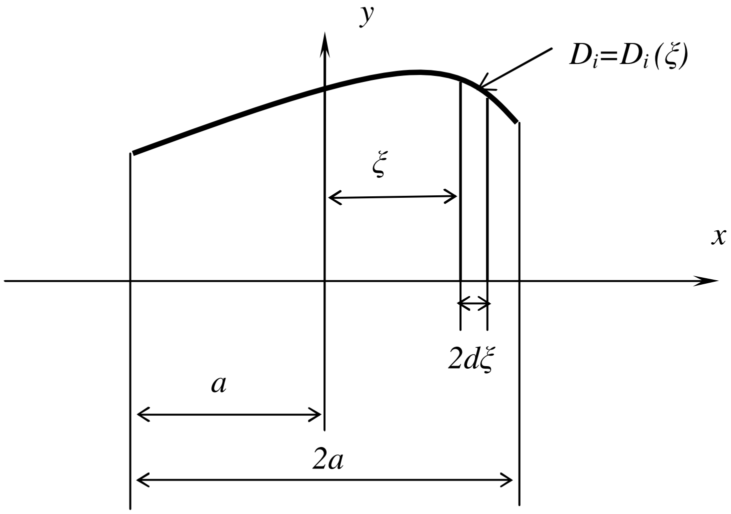

Fig. B.1 An arbitrary DD function and its differential element

If the following integrals are obtained

$U_{ij}(x,y)=\int_{-a}^{a} D_j(\xi)V_i(x,y,\xi)d\xi$ (*i*=2, 3... 7; *j*=1, 2) B.6

, then the displacements and stresses at point *P* (*x,y*) due to the whole element DD can be written as

$$\begin{aligned} u_x &= \left[2(1-\nu)U_{3x}(x,y) - yU_{5x}(x,y)\right] + \left[-(1-2\nu)U_{2y}(x,y) - yU_{4y}(x,y)\right] \\ u_y &= \left[(1-2\nu)U_{2x}(x,y) - yU_{4x}(x,y)\right] + \left[2(1-\nu)U_{3y}(x,y) - yU_{5y}(x,y)\right] \end{aligned} \qquad \text{............ B.7}$$

$$\begin{aligned} \sigma_{xx} &= 2G\left[2U_{4x}(x,y) + yU_{6x}(x,y)\right] + 2G\left[-U_{5y}(x,y) + yU_{7y}(x,y)\right] \\ \sigma_{yy} &= 2G\left[-yU_{6x}(x,y)\right] + 2G\left[-U_{5y}(x,y) - yU_{7y}(x,y)\right] \\ \sigma_{xy} &= 2G\left[-U_{5x}(x,y) + yU_{7x}(x,y)\right] + 2G\left[-yU_{6y}(x,y)\right] \end{aligned} \qquad \text{.................. B.8}$$

The displacement discontinuity function at a left crack tip can be expressed as (Crouch and Starfield 1983, Yan 2004):

$$\begin{aligned} D_x &= H_s\left(\frac{a+\xi}{a}\right)^{0.5} \\ D_y &= H_n\left(\frac{a+\xi}{a}\right)^{0.5} \end{aligned} \qquad \text{.. B.9}$$

where H_s and H_n are the tangential and normal DD at the center of the crack element, respectively.

Substitute **Eq. B.9** into **B.6**, we can get

$$U_{ij}(x,y) = H_j\int_{-a}^{a}\sqrt{\frac{a+\xi}{a}}V_i(x,y,\xi)d\xi = H_jB_i(x,y) \quad (i\text{=2, 3... 7; }j\text{=1, 2}) \qquad \text{............... B.10}$$

where

$$B_i(x,y) = \int_{-a}^{a}\sqrt{\frac{a+\xi}{a}}V_i(x,y,\xi)d\xi \quad (i\text{=2, 3... 7}) \qquad \text{.. B.11}$$

Then substitute **Eq. B.10** into **Eq.B.7** and **B.8**, we can get

$$\begin{aligned} u_x &= H_s\left[2(1-\nu)B_3(x,y) - yB_5(x,y)\right] + H_n\left[-(1-2\nu)B_2(x,y) - yB_4(x,y)\right] \\ u_y &= H_s\left[(1-2\nu)B_2(x,y) - yB_4(x,y)\right] + H_n\left[2(1-\nu)B_3(x,y) - yB_5(x,y)\right] \end{aligned} \quad \text{..........B.12}$$

$$\begin{aligned} \sigma_{xx} &= 2GH_s\left[2B_4(x,y) + yB_6(x,y)\right] + 2GH_n\left[-B_5(x,y) + yB_7(x,y)\right] \\ \sigma_{yy} &= 2GH_s\left[-yB_6(x,y)\right] + 2GH_n\left[-B_5(x,y) - yB_7(x,y)\right] \\ \sigma_{xy} &= 2GH_s\left[-B_5(x,y) + yB_7(x,y)\right] + 2GH_n\left[-yB_6(x,y)\right] \end{aligned} \quad \text{................B.13}$$

B_i (*i*=2, 3... 7) in **Eq. B.11** can be computed as following (Yan 2004):

1) An arbitrary point *P*(*x,y*) (*y≠0*)

Gauss numerical integration can be used to calculate B_i. Let

$$\xi = at \quad \text{..B.14}$$

Then **Eq. B.11** can be written as:

$$B_i(x,y) = a\int_{-1}^{1} V_i(x,y,at)\sqrt{1+t}\,dt \quad (i=2, 3... 7) \quad \text{........................B.15}$$

$$B_i(x,y) = a\sum_j V_i(x,y,a\zeta_j)\sqrt{1+\zeta_j}\,w_j \quad (i=2, 3... 7) \quad \text{........................B.16}$$

where ζ_j and w_j are the Gauss point coordinates and corresponding weighted factors, respectively.

2) An arbitrary point *P*(*x,y*) (*y=0*)

For $x > -a$,

$$B_2(x,0) = \frac{-1}{4\pi(1-v)}\left\{-2\sqrt{2} + \sqrt{\frac{x+a}{a}}\, ln\left|\frac{\sqrt{x+a}+\sqrt{2a}}{\sqrt{x+a}-\sqrt{2a}}\right|\right\}$$

$$B_4(x,0) = 0$$

$$B_5(x,0) = \frac{1}{4\pi(1-v)}\left\{\frac{\sqrt{2}}{x-a} - \frac{1}{2\sqrt{a(x+a)}}\, ln\left|\frac{\sqrt{x+a}+\sqrt{2a}}{\sqrt{x+a}-\sqrt{2a}}\right|\right\} \qquad \text{....... B.17}$$

$$B_6(x,0) =$$

$$\frac{1}{4\pi(1-v)}\left\{\frac{\sqrt{2}}{(x-a)^2} - \frac{\sqrt{2}}{2(x^2-a^2)} - \frac{1}{4\sqrt{a}\,(x+a)^{3/2}}\, ln\left|\frac{\sqrt{x+a}+\sqrt{2a}}{\sqrt{x+a}-\sqrt{2a}}\right|\right\}$$

$$B_7(x,0) = 0$$

For $x < -a$, let $r = |x| - a$,

Then

$$B_2(x,0) = \frac{-1}{4\pi(1-v)}\left\{-2\sqrt{2} + 2\sqrt{\frac{r}{a}}\arctan\sqrt{\frac{2a}{r}}\right\}$$

$$B_4(x,0) = 0$$

$$B_5(x,0) = \frac{1}{4\pi(1-v)}\left\{-\frac{\sqrt{2}}{r+2a} + \frac{1}{\sqrt{ar}}\arctan\sqrt{\frac{2a}{r}}\right\} \qquad \text{........ B.18}$$

$$B_6(x,0) = \frac{1}{4\pi(1-v)}\left\{\frac{\sqrt{2}}{(r+2a)^2} - \frac{\sqrt{2}}{2r(r+2a)} - \frac{1}{2\sqrt{a}r^{3/2}}\arctan\sqrt{\frac{2a}{r}}\right\}$$

$$B_7(x,0) = 0$$

3) An arbitrary point $P(x,y)$ ($y=0$)

$$B_3(x,0) = 0, |x| > a$$

$$B_3(x,0) = \frac{1}{4(1-v)}, y = 0_+, |x| < a \qquad \text{... B.19}$$

$$B_3(x,0) = -\frac{1}{4(1-v)}, y = 0_-, |x| < a$$

4) For point $P(0,0)$

$$B_2(0,0) = \frac{-1}{4\pi(1-v)}\left\{-2\sqrt{2} + ln\left|\frac{1+\sqrt{2}}{1-\sqrt{2}}\right|\right\}$$

$$B_3(x,0) = \frac{1}{4(1-v)}, y = 0_+$$

$$B_3(x,0) = -\frac{1}{4(1-v)}, y = 0_-$$

$$B_4(0,0) = 0 \qquad \text{.......................................} \text{B.20}$$

$$B_5(0,0) = \frac{1}{4\pi(1-v)}\left\{-\sqrt{2} - \frac{1}{2}ln\left|\frac{1+\sqrt{2}}{1-\sqrt{2}}\right|\right\}/a$$

$$B_6(0,0) = \frac{1}{4\pi(1-v)}\left\{\frac{-3\sqrt{2}}{2} - \frac{1}{4}ln\left|\frac{1+\sqrt{2}}{1-\sqrt{2}}\right|\right\}/a^2$$

$$B_7(0,0) = 0$$

As the two tips are symmetric, knowing the calculation of influence coefficients from a left tip element to an arbitrary domain point *P*(x,y) (x, y are coordinates of the arbitrary point in the local coordinate system of the influencing tip element), the influence coefficients from a right crack tip element to an arbitrary point *P* can be calculated using the same functions of B_i (from **Eq. B.17** to **B.20**) but the negative value of coordinates of the arbitrary point P in the local coordinate system of the influencing right tip element *P'(-x, -y)*.

APPENDIX C

PROGRAM FLOWCHART

Main program

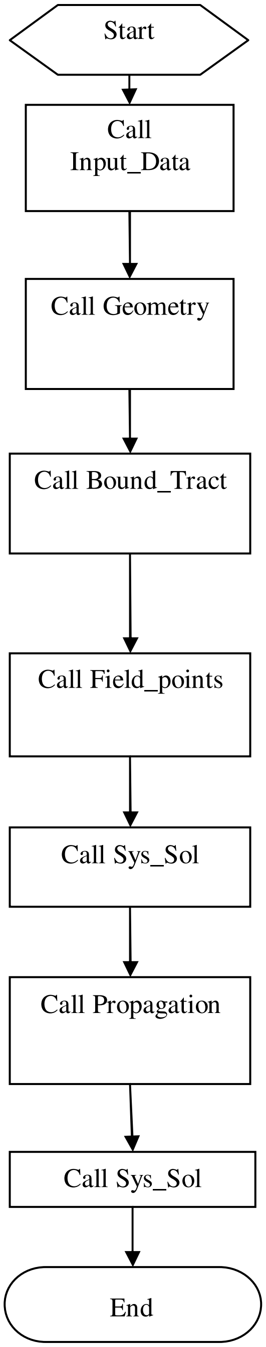

Calculate geometric parameters

for the elements

Calculate boundary concentration at each element

- *far_field stress:PFM , PFN, PFNM, PFP*
- *Induced stress: PM, PN, PNM (or induced displacement)*
- *Induced pore pressure TEMP*

Calculate field point coordinates

Core part (see next page)

Determine fracture propagation direction and mode (details can be found in Dob's paper)

To have a correct value of temperature and displacements on the next time step, changes in geometry are accounted for by calling sys_sol again.

Sys_sol routine

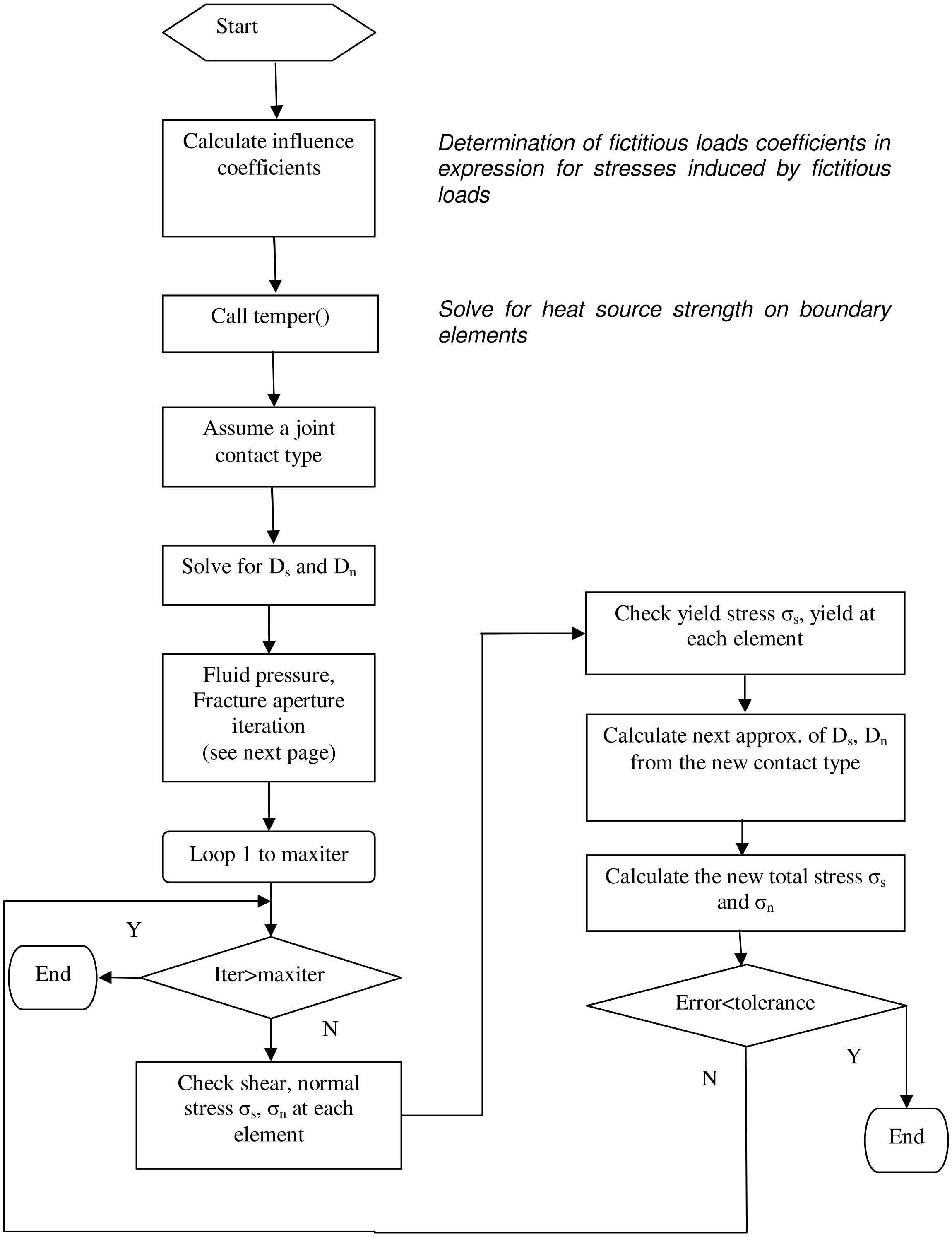

Determination of fictitious loads coefficients in expression for stresses induced by fictitious loads

Solve for heat source strength on boundary elements

Fracture Pressure/width iteration

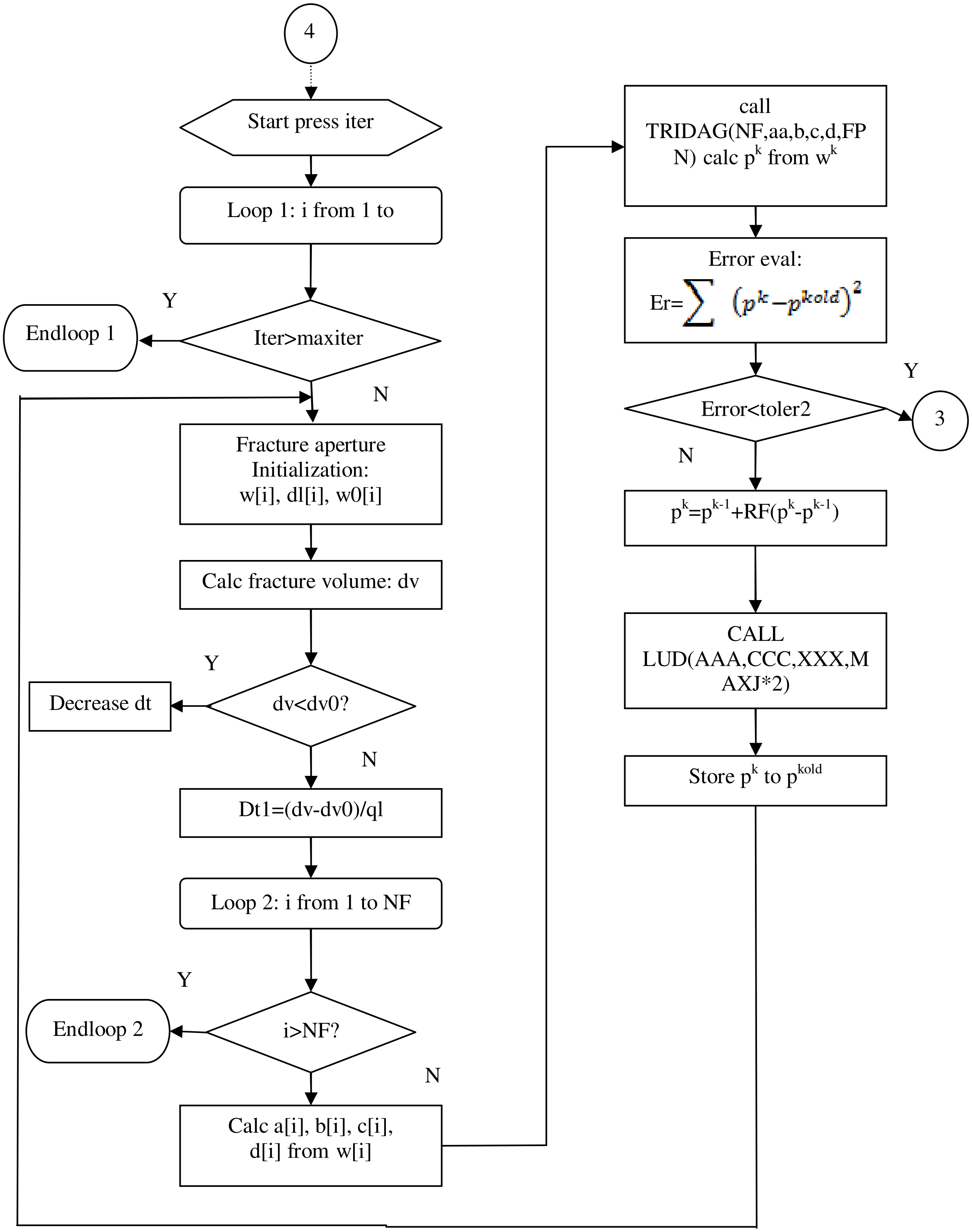

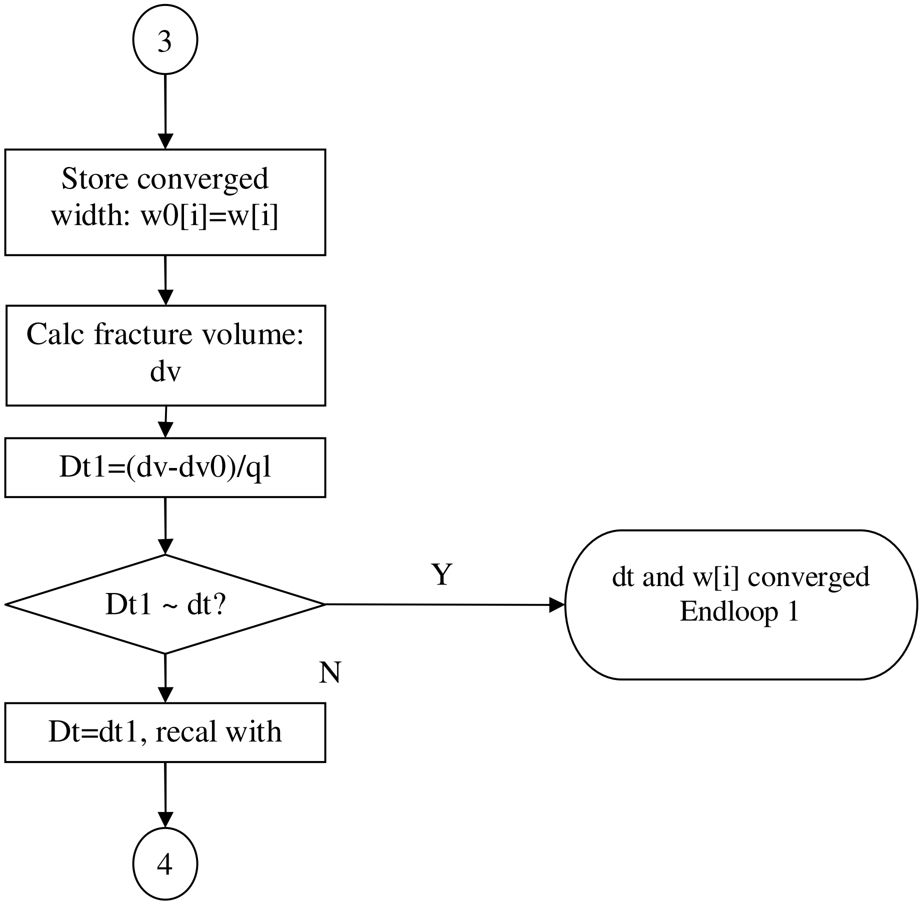
3
Store converged width: w0[i]=w[i]
Calc fracture volume: dv
Dt1=(dv-dv0)/ql
Dt1 ~ dt?
Y
dt and w[i] converged Endloop 1
N
Dt=dt1, recal with
4

VITA

Name: Wenxu Xue

Permanent Address: Harold Vance Department of
Petroleum Engineering,
3116 TAMU,
College Station, TX 77843-3116

Email Address: xuewenxu@gmail.com

Education: Tsinghua University,
Beijing, China
B.S., Thermal Energy and Power Engineering,
July 2004

Texas A&M University,
College Station, Texas, USA
M.S., Petroleum Engineering,
December 2010

Affiliation: Society of Petroleum Engineers
American Rock Mechanics Association
Honor Society of Phi Kappa Phi